INVERSE SOLUTIONS IN ELECTROMAGNETISM WITH APPLICATIONS IN BIOMEDICAL IMAGING AND NON-DESTRUCTIVE TESTING

By

REZA K. AMINEH, M.Sc., B.Sc.

A Thesis
Submitted to the School of Graduate Studies
in Partial Fulfillment of the Requirements
for the Degree
Doctor of Philosophy

McMaster University

DOCTOR OF PHILOSOPHY (2010)   McMaster University
(Electrical and Computer Engineering)   Hamilton, Ontario

TITLE: Inverse Solutions in Electromagnetism with Applications in Biomedical Imaging and Non-Destructive Testing

AUTHOR: Reza K. Amineh, M.Sc. (Amirkabir University), B.Sc. (Sharif University)

SUPERVISOR: Professor Natalia K. Nikolova

CO-SUPERVISOR: Professor James P. Reilly

NUMBER OF PAGES: xxv, 184

ABSTRACT

This thesis presents solutions to several inverse problems in electromagnetism and microwave engineering. In general, these inverse problems belong to two applications: breast cancer diagnosis using microwave imaging and defect characterization in metallic structures using magnetic flux leakage (MFL).

Our contribution in microwave imaging for breast tumor detection can be divided into three parts. First, we propose a novel ultra-wide band (UWB) antenna that can operate in direct contact with the breast without the need for coupling liquids. This antenna is designed such that more than 90% of the radiated power is directed toward the tissue from its front aperture over the UWB. The performance of the antenna is investigated via simulation and measurement of the following parameters: return loss, near-field directivity, efficiency, fidelity, and group velocity. Overall, the results show that the antenna is a good candidate for frequency and time-domain imaging techniques.

Second, we have proposed an aperture raster scanning setup that benefits from the features of our novel antenna. In this scanning setup, the breast tissue is compressed between two rectangular plates (apertures) while two antennas perform two-dimensional (2-D) scan by moving together on both sides of the

compressed tissue. For each scanning step, the transmission S-parameter between the two antennas is recorded at several frequencies within UWB. Then, the modulus of the calibrated transmission S-parameter is plotted at each frequency to provide a 2-D image of the interior of the breast. The images are enhanced using a de-blurring technique based on blind de-convolution. This setup provides real time images of strong scatterers inside the normal tissue.

Third, we propose 2-D and three-dimensional (3-D) holography algorithms to further improve the quality of the images obtained from the proposed planar scanning setup. These techniques are based on the Fourier transforms of the collected data to provide an image of a 2-D target (when collecting data at a single frequency) or a 3-D target (when collecting wide-band data). These techniques are fast and very robust to noise. The capability of the 2-D and 3-D holographic imaging techniques is examined via simulation results.

For defect characterization in metallic structures using MFL technique, we propose fast and reliable methodologies to invert the measured MFL response to the defect's shape parameters. First, we present a procedure to estimate the shape parameters of rectangular cracks which are the most common type of defects in the metallic structures. The procedure consists of estimating orientation, length, and depth of the cracks, consecutively. We validate this procedure via estimating the shape parameters of pre-known cracks from the simulated and measured MFL responses. Then, we present a methodology based on space mapping (SM)

optimization for defect characterization. We examine the efficiency of this methodology for two types of defects: rectangular cracks and cylindrical pits.

ACKNOWLEDGEMENTS

It is a pleasure to thank many people who made this thesis possible. First and foremost I offer my sincerest gratitude to my PhD supervisor, Dr. Natalia K. Nikolova, who has supported me throughout my thesis with her patience and knowledge whilst allowing me the room to work in my own way. With her enthusiasm, inspiration, and her great efforts to explain things clearly and simply, she helped me to understand and proceed through this long way. Throughout my PhD program, she provided encouragement, sound advice, good teaching, good company, and lots of novel ideas. One simply could not wish for a better supervisor.

I would like to thank my co-supervisor, Dr. James P. Reilly, for his help and support. I also thank the members of my supervisory committee meeting, Dr. Mohamed H. Bakr, Dr. Michael D. Noseworthy, and Dr. Aleksander Jeremic for their precious time and valuable suggestions for the work done in this thesis. I gratefully acknowledge Dr. John W. Bandler and Dr. Slawomir Koziel for providing the opportunity of learning new concepts for me.

Furthermore, I am deeply indebted to my colleagues at the Computational Electromagnetics Laboratory at McMaster University that have provided the environment for sharing their experiences about the problems involved as well as participating in stimulating team exercises. I would specially like to thank my colleague and co-author Aastha Trehan for her valuable efforts and supports. I was very lucky to have my wonderful colleagues and friends since they not only gave me a lot of support but also made my long journey much more cheerful. My thanks go to all the friends including Kaveh Moussakhani, Li Liu, Mohamed Swillam, Yunpeng Song, Xiaying Zhu, Mohammad S. Dadash, Ali Khalatpour, Arshad Hasib, Osman Ahmed, Mohamed Negm, Yifan Zhang, and Qingsha Chen.

Words fail me to express my appreciation to my beloved wife Maryam whose dedication, love and persistent confidence in me, has taken the load off my shoulder. I owe her for letting her intelligence, passions, and ambitions collide with mine, unselfishly. Therefore, I would also thank Ravan's family for letting me take her hand in marriage and walk away to explore new opportunities together.

My deep love and appreciation goes to my family in Iran with whom I shared my childhood and whose love and support still sustain me today. My sister and brothers: Bita, Amin, and Mohammad who are all so much part of me and my memories of childhood. To my parents who gave me a curiosity about life which has resulted in this thesis.

INVERSE SOLUTIONS IN ELECTROMAGNETISM WITH APPLICATIONS IN BIOMEDICAL IMAGING AND NON-DESTRUCTIVE TESTING

Contents

Chapter 3 Aperture Raster Scanning Setup for Near-Field Microwave Imaging 35

List of Figures

List of Tables

List of Acronyms

2-D	Two Dimensional
3-D	Three Dimensional
CPU	Central Processing Unit
DAS	Delay-and-Sum
EMI	Electromagnetic Interference
FCC	Federal Communication Commission
FEM	Finite Element Method
FT	Fourier Transform
MFL	Magnetic Flux Leakage
MIST	Microwave Imaging via Space-Timing
MRI	Magnetic Resonance Imaging
NDT	Non-Destructive Testing
NFD	Near-Field Directivity
PSF	Point-Spread Function
RAM	Random-Access Memory
SM	Space Mapping
SNR	Signal to Noise Ratio
TEM	Transverse Electromagnetic
UWB	Ultra-Wide Band
VNA	Vector Network Analyzer

CHAPTER 1

INTRODUCTION

Problems in engineering and science may be formulated in two opposing ways [1]: find the effect of a given cause or, conversely, find the cause which produces a prescribed or measured effect. The former are called forward problems while the latter are inverse problems. Inverse problems in which data come from measurements are known as identification or parameter-estimation problems. Another type of inverse problem is the synthesis problem, in which data are assumed based on certain requirement and a solution may not exist. The optimal design problems belong to this group. They are very popular in engineering, where the purpose is to design a device which can provide a specified behavior and/or optimal performance. In this thesis, we consider various types of inverse problems in the electromagnetic and microwave areas.

1.1 MOTIVATION

The inverse problems considered in this thesis are related to two major applications: microwave imaging for breast cancer diagnosis and non-destructive testing of metallic structures. We categorize the motivation for this thesis into two parts as described below.

1.1.1 Microwave Imaging for Breast Cancer Diagnosis

Breast cancer is the second common cancer after lung cancer and is the most common cancer among women [2]. It is usually detected using X-ray mammography [3][4]. Despite the wide usage of mammography, there are a few problems associated with this method. The most important is that 5%–15% of the tumors can not be seen mammographically [4][5]. In addition, the health hazard arising from the ionization of tissues caused by X-rays prevents regular examination of women. Therefore, alternative or complementing imaging methods are needed. Microwave imaging is an emerging modality for this purpose.

Microwave imaging is not limited to breast cancer imaging. The technique can be used in many different fields and applications. Some examples are subsurface sensing such as landmine detection (e.g., [6]), nondestructive testing of materials (e.g., [7]), concealed weapon detection (e.g., [8]), and other types of biomedical imaging (e.g., [9]).

The microwave applications for imaging of biological tissues had a breakthrough in 1979 when Jacobi *et al.* [10] developed a water-immersed antenna system that was able to successfully image canine kidney [11]. Later, research activities included experimental microwave imaging based mainly on linear reconstruction algorithms utilizing the Born and the Rytov approximations (e.g., see [12][13]). It was shown that the best performance of the linear reconstruction algorithms was limited to small low contrast objects [14]–[16]. Thus, the following developments have mainly been focused on iterative nonlinear reconstruction algorithms which are more computationally intensive, but lead to better image quality [17]–[28]. The problem to be solved is inherently ill-posed and nonlinear. Therefore, an iterative optimization algorithm has to be used, which involves a cost function that is either maximized or minimized. However, the nonlinearity of the problem often causes the algorithm to get trapped in a local minimum leading to an incorrect reconstruction [29]. To alleviate this problem, frequency-hopping technique has been proposed where the low-frequency content of the electromagnetic pulse is used to reduce the nonlinearities. This is then followed by using successively higher frequency content to improve the resolution [30]. In [31], a 3D microwave imaging setup has been proposed in which the diagonal tensor approximation acts as a preconditioner for the stabilized biconjugate-gradient FFT method. Another possibility to reduce illposedness is to use *a priori* information about the object being imaged [22]. Contributions such as [32]–[34] describe how this can be done. The problem of local minima can often be resolved with a good initial guess or by starting the reconstruction from some ideal model of the expected targets. This is, for example, viable in biomedical imaging where the organs and tissues can be assumed known [32], or when testing an object for a defect when the unperturbed object is known [33]. A method for introducing a finite number of different dielectric materials based on Markov modeling and the Bayesian framework has been suggested in [34]. Yet another technique that can be understood as a shape recognition method, the level set method, was suggested in [35]. Later references on the same method include [36]–[39]. To overcome the ill-posedness, it is furthermore necessary to apply a regularization procedure that is introducing constraints on the reconstructed image. An effective regularization should make use of constraints corresponding to known physical properties of the object being imaged. The Tikhonov method is an example of a method that is often used to impose a smoothness condition on the reconstruction [40]. A review and classification of some regularization techniques have been presented in [41]. Also in a recent work, a sparsity regularization approach has been presented [42] for solving inverse scattering problems using the distorted Born iterative method. Although in the optimization-based microwave imaging described so far the data is collected in the frequency domain, in a recent work [43], time-domain data has been acquired which allows very few transmitters and receivers to be employed._In general, the non-linear optimization-based image reconstruction is very expensive in terms of memory and time and may not lead to reliable results.

Another group of techniques proposed for microwave imaging is the radar-based imaging. In radar-based imaging, the goal is to create a map of the scattering arising from the contrast in the dielectric properties within the breast. The radar approach originates from military and ground-penetrating applications and was proposed for breast-cancer detection in the late nineties independently by Benjamin in 1996 [44], [45] and Hagness in 1998 [46]. In contrast to most optimization-based techniques, the proposed radar systems operate at higher frequencies (up to 10 GHz) and use a large bandwidth (as much as 8 GHz). Most of these radars are therefore ultrawide band (UWB). The scattering information is obtained from transmission and reception of short UWB electromagnetic pulses. The simplest algorithm proposed for radar-based imaging was a standard delay-and-sum (DAS) focusing [47]. More elaborate techniques such as microwave imaging via space-time (MIST) address some drawbacks of DAS. The MIST algorithm [48][49] outperforms mono-static DAS, although multi-static DAS still outperforms mono-static MIST [50]. More recently, Xie *et al.* [50][51] proposed a new data-adaptive algorithm for breast-cancer detection based on robust Capon beamforming. Using full-wave FDTD simulations with idealized antennas (point sources), the authors showed that their new algorithm provides better performance than multi-static DAS and MIST. Compared to the mono-static approaches, a multi-static approach with a fully-populated antenna array enables the acquisition of far more data. In [52], a planar antenna array was used, with all antennas printed on the same substrate. Encouraging experimental phantom results showed the strength of the multi-static radar approach. However, the performance of the flat array is limited by the finite beamwidth of the antennas and, additionally, a planar arrangement does not conform well to the breast. Recently, the same research group presented the prototype of a multi-static radar based on a hemispherical antenna array [53]. A big advantage of radar-based imaging over the optimization-based imaging is its relatively simple and robust signal processing. To date there have been only a few experimental breast-imaging radar systems reported in the open literature [48][53]-[55]. Although radar-based techniques have their advantages (e.g., simplicity), they provide limited performance in terms of image resolution and clutter rejection.

In addition to the drawbacks mentioned above for optimization-based and radar-based techniques, the proposed imaging setups so far require immersing the antennas and the breast tissue in a coupling liquid. This not only complicates the maintenance and sanitation of the setup but also causes additional loss in microwave measurements. All of the above drawbacks have hindered the progress toward successful clinical trials.

In this thesis, we first propose novel antennas/sensors for near-field microwave imaging of the breast. The antenna is designed to operate in the UWB. The antenna characterization includes return loss, total efficiency, near-field directivity, fidelity, and group velocity. Then, for the first time we consider the direct raster scanning technique when measuring the transmission *S*-parameters in the UWB. We also study its feasibility in breast-cancer detection. The properties of our novel sensors enable this methodology with the following advantages. (1) The need for coupling liquids is eliminated due to the low-loss dielectric material incorporated into the antenna structure. This significantly simplifies the maintenance and sanitation of the envisioned clinical setup. Also, this eliminates the additional power loss due to the coupling liquids. (2) The small sensor aperture leads to enhanced spatial resolution in the images. (3) The UWB properties of the antenna allow for aperture raster scanning in the UWB frequency range. (4) Simple and fast post-processing algorithms facilitate real time, reliable, and robust imaging of the breast. This is achieved by an efficient blind de-convolution algorithm for image de-blurring. In addition, we proposed fast and reliable signal processing techniques using the principle of microwave holography to further improve the images obtained from the rectangular aperture scanning.

1.1.2 Magnetic Flux Leakage Technique for Non-Destructive Testing

The magnetic flux leakage (MFL) technique plays an important role in the nondestructive testing (NDT) of buried oil and gas pipelines in order to find metal-loss regions usually caused by corrosion, fatigue, etc. The size and shape of the defects can be obtained by studying the distribution of the MFL output signal. After the leakage field is measured, an inverse problem must be solved so that the shape characteristics of the flaw, such as width, length and depth can be estimated. The correct assessment of this information is vital in order to determine critical regions in the pipelines.

The MFL inversion techniques often use an iterative approach where a forward model calculates the leakage field for a given set of defect parameters. Three major groups of forward models are commonly used. The first group involves numerical simulations typically based on the finite element method (FEM) [56]-[58]. These models provide accurate results but the drawback is that they are computationally very demanding. The second group consists of closed-form analytical formulas for defects of certain canonical shapes [59]-[62]. These models typically utilize magnetic poles or dipoles on the defect walls. They are very fast but less accurate and versatile due to the assumptions made in deriving the analytical formulas [60][62]. The third group of forward MFL models is based on artificial neural networks for two-dimensional (2-D) and three-dimensional (3-D) flaws [63]-[67]. These models are fast but are limited to the region in parameter space for which the neural network is trained.

In this thesis, we first propose a direct methodology to invert MFL signals to the shape parameters of surface-breaking cracks. Simple techniques are utilized to provide fast and reliable means for characterization of rectangular cracks. The estimated shape parameters include: orientation, length, and depth. Then, space mapping (SM) optimization [68]-[71] methodology is proposed for the first time for defect characterization using MFL responses. In space mapping optimization, the burden of the optimization is placed on a fast but less accurate coarse model while the more accurate but expensive (in terms of memory and time) fine model is evaluated only a few times during the optimization process. The proposed methodology is examined for two types of defects: rectangular cracks and cylindrical pits.

1.2 CONTRIBUTIONS

The author has contributed substantially to a number of original developments presented in this thesis. These are briefly described next.

(1) Design, fabrication, and measurement of a TEM horn antenna/sensor for microwave imaging of the breast.

(2) Proposing a raster aperture scanning setup for microwave imaging of the breast.

(3) Developing two-dimensional (2-D) and three-dimensional (3-D) holography techniques for near-field microwave imaging.

(4) Proposing direct inversion technique for characterization of surface-breaking cracks using MFL data.

(5) Proposing space mapping optimization methodology for fast and reliable parameter estimation of surface defects using MFL data.

The work presented in this thesis has been published or submitted for publication in eight journals and sixteen conference proceedings. These are cited throughout the thesis.

1.3 OUTLINE OF THE THESIS

In Chapter 2, a novel transverse electromagnetic (TEM) horn antenna placed in a solid dielectric medium is proposed for microwave imaging of the breast. The major design requirement is that the antenna couples the microwave energy into the tissue without being immersed itself in a coupling medium. The antenna achieves this requirement by: 1) directing all radiated power through its front aperture, and 2) blocking external electromagnetic interference by a carefully designed enclosure consisting of copper sheets and absorbing sheets. The major investigated antenna parameters in the UWB include: return loss, near-field directivity (NFD), efficiency, group velocity, and fidelity.

In chapter 3, the proposed antenna is employed in a raster scanning imaging setup. The setup consists of two antennas aligned along each other's boresight and moving together to scan two parallel apertures. The imaged object lies between the two apertures. With a blind de-convolution algorithm, the images are de-blurred.

In chapter 4, new 2-D and 3-D holographic microwave imaging techniques are proposed to reconstruct an image of the targets. These techniques are based on the Fourier analysis of the data recorded by two antennas scanning together two separate rectangular parallel apertures on both sides of a target. No assumptions are made about the incident field, which can be derived by either simulation or measurement. Both the back-scattered and forward-scattered signals can be used to reconstruct the image of the target. This makes the proposed technique applicable with near-field measurements. Associated resolution limits, sampling constraints, and the impact of noise are also discussed.

The work in chapter 5 is two-fold. In the first part, a direct procedure is proposed for full characterization of rectangular surface-breaking cracks based on the MFL measurements of only one tangential component of the magnetic field. The parameters of interest include the orientation, length and depth of the cracks. In the second part, a space mapping methodology is proposed to expedite the optimization process in defect characterization using the MFL data. The proposed methodology is examined for two types of defects: rectangular cracks and cylindrical pits.

REFERENCES

[1] P. Neittaanmaki, M. Rudnicki, and A. Savini, *Inverse Problems and Optimal Design in Electricity and Magnetism*. Clarendon Press, Oxford, 1996.

[2] D. M. Parkin, F. Bray, J. F. And, and P. Pisani, "Global cancer statistics, 2002," *CA: A Cancer J. Clinicians*, vol. 55, pp. 74–108, Mar. 2005.

[3] C. H. Jones, "Methods of breast imaging," *Phys. Med. Biol.*, vol. 27, pp. 463–499, Apr. 1982.

[4] M. Säbel and H. Aichinger, "Recent developments in breast imaging," *Phys. Med. Biol.*, vol. 41, pp. 315–368, Mar. 1996.

[5] P. T. Huynh, A. M. Jarolimek, and S. Daye, "The false-negative mammogram," *Radiographics*, vol. 18, pp. 1137–1154, 1998.

[6] T. P. Montoya and G. S. Smith, "Land mine detection using a ground-penetrating radar based on resistively loaded Vee dipoles," *IEEE Trans. Antennas and propag.*, vol. 47, no. 12, pp. 1795–1806, 1999.

[7] J. C. Bolomey, "New concept for microwave sensing," *Adv. Microwave Millim. Wave Detectors*, vol. 2275, 1994.

[8] D. M. Sheen, D. L. McMakin, and T. E. Hall, "Three-dimensional millimeter-wave imaging for concealed weapon detection," *IEEE Trans. Microwave Theory and Tech.*, vol. 49, no. 9, pp. 1581–1592, 2001.

[9] D. Colton and P. Monk, "The detection and monitoring of leukemia using electromagnetic waves: mathematical theory," *Inv. Problems*, vol. 10, pp. 1235–1251, 1994.

[10] J. H. Jacobi, L. E. Larsen, and C. T. Hast, "Water-immersed microwave antennas and their application to microwave interrogation of biological targets," *IEEE Trans. Microwave Theory Tech.*, vol. MTT-27, no. 1, pp. 70–78, Jan. 1979.

[11] L. E. Larsen and J. H. Jacobi, "Microwave scattering parameter imagery of an isolated canine kidney," *Med. Phys.*, vol. 6, pp. 394–403, 1979.

[12] A. J. Devaney, "Reconstructive tomography with diffracting wave-fields," *Inv. Problems*, vol. 2, no. 2, pp. 161–183, May 1986.

[13] R. Aitmehdi, A. P. Anderson, S. Sali, and M. Ferrando, "The determination of dielectric loss tangent by microwave phase tomography," *Inv. Problems*, vol. 4, no. 2, pp. 333–345, May 1988.

[14] M. Slaney, A. C. Kak, and L. E. Larsen, "Limitations of imaging with first order diffraction tomography," *IEEE Trans. Microwave Theory Tech.*, vol. 32, no. 8, pp. 860–873, Aug. 1984.

[15] J. C. Bolomey, C. Pichot, and G. Gaboriaud, "Planar microwave camera for biomedical applications: Critical and prospective analysis of reconstruction algorithms," *Radio Sci.*, vol. 26, no. 2, pp. 541–549, Mar.–Apr. 1991.

[16] A. Fhager and M. Persson, "Comparison of two image reconstruction algorithms for microwave tomography," *Radio Sci.*, vol. 40, no. 3, Jun. 2005, Article RS3017.

[17] A. Abubakar, P. M. van den Berg, and J. J. Mallorqui, "Imaging of biomedical data using a multiplicative regularized contrast source inversion method," *IEEE Trans. Microwave Theory Tech.*, vol. 59, no. 7, pp. 1761–1771, Jul. 2002.

[18] R. E. Kleinman and P. M. van den Berg, "A modified gradient method for two-dimensional problems in tomography," *J. Comput. Appl. Math.*, vol. 42, no. 1, pp. 17–35, Sep. 1992.

[19] W. C. Chew and Y. M.Wang, "Reconstruction of two-dimensional permittivity distribution using the distorted born iterative method," *IEEE Trans. Med. Imag.*, vol. 9, no. 2, pp. 218–225, Jun. 1990.

[20] Q. H. Liu, Z. Q. Zhang, T. T. Wang, J. A. Bryan, G. A. Yabbara, L. W. Nolte, and W. T. Jones, "Active microwave imaging I—2-D forward and inverse scattering methods," *IEEE Trans. Microwave Theory Tech.*, vol. 50, no. 1, pp. 123–133, Jan. 2002.

[21] S. Caorsi, G. L. Gragnani, and M. Pastorino, "Reconstruction of dielectric permittivity distributions in arbitrary 2-D inhomogeneous biological bodies by a multiview microwave numerical method," *IEEE Trans. Med. Imag.*, vol. 12, no. 6, pp. 232–239, Jun. 1993.

[22] N. Joachimowicz, C. Pichot, and J. P. Hugonin, "Inverse scattering: an iterative numerical method for electromagnetic imaging," *IEEE Trans. Antennas Propag.*, vol. 39, no. 12, pp. 1742–1753, Dec. 1991.

[23] P. Meaney, K. D. Paulsen, A. Hartov, and R. K. Crane, "An active microwave imaging system for reconstruction of 2-D electrical property distributions," *IEEE Trans. Biomed. Eng.*, vol. 42, no. 10, pp. 1017–1026, Oct. 1995.

[24] A. E. Bulyshev, A. E. Souvorov, S. Y. Semenov, V. G. Posukh, and Y. E. Sizov, "Three-dimensional vector microwave tomography: Theory and computational experiments," *Inv. Problems*, vol. 20, no. 4, pp. 1239–1259, Aug. 2004.

[25] A. Abubakar and P. M. van den Berg, "Iterative forward and inverse algorithms based on domain integral equations for three-dimensional electric and magnetic objects," *J. Comput. Phys.*, vol. 195, no. 1, pp. 236–262, Mar. 2004.

[26] Z. Q. Zhang and Q. H. Liu, "Three-dimensional nonlinear image reconstruction for microwave biomedical imaging," *IEEE Trans. Biomed. Eng.*, vol. 51, no. 3, pp. 544–548, Mar. 2004.

[27] Q. Fang, P. M. Meaney, S. D. Geimer, A. V. Streltsov, and K. D. Paulsen, "Microwave image reconstruction from 3-D fields coupled to 2-D parameter estimation," *IEEE Trans. Med. Imag.*, vol. 23, no. 4, pp. 475–484, Apr. 2004.

[28] S. Y. Semenov, A. E. Bulyshev, A. Abubakar, V. G. Posukh, Y. E. Sizov, A. E. Souvorov, P. M. van den Berg, and T. C. Williams, "Microwave-tomographic imaging of high dielectric-contrast objects using different image-reconstruction approaches," *IEEE Trans. Microwave Theory Tech.*, vol. 53, no. 7, pp. 2284–2295, Jul. 2005.

[29] T. Isernia, V. Pascazio, and R. Pierri, "On the local minima in a tomographic imaging technique," *IEEE Trans. Geosci. Remote Sens.*, vol. 39, no. 7, pp. 1596–1607, Jul. 2001.

[30] W. C. Chew and J. H. Lin, "A frequency-hopping approach for microwave imaging of large inhomogeneous bodies," *IEEE Microwave Guided Wave Lett.*, vol. 5, no. 12, pp. 439–441, Dec. 1995.

[31] C. Yu, M. Yuan, J. Stang, E. Bresslour, R. T. George, G. A. Ybarra, W. T. Joines, and Q. H. Liu, "Active microwave imaging II: 3-D system prototype and imaging reconstruction from experimental data," IEEE *Trans. Microwave Theory Tech.*, vol. 56, no. 4, pp. 991–1000, Apr. 2008.

[32] S. Caorsi, G. L. Gragnani, M. Pastorino, and M. Sartore, "Electromagnetic imaging of infinite dielectric cylinders using a modified born approximation and including *a priori* information on the unknown cross sections," *Proc. Inst. Elect. Eng.—Microw. Antennas Propag.*, vol. 141, no. 6, pp. 445–450, Dec. 1994.

[33] M. Benedetti, M. Donelli, G. Franceschini, M. Pastorino, and A. Massa, "Effective exploitation of the *a priori* information through a microwave imaging procedure based on the SMW for NDE/NDT applications," *IEEE Trans. Geosc. Remote Sens.*, vol. 43, no. 11, pp. 2584–2592, Nov. 2005.

[34] O. Féron, B. Duchêne, and A. Mohammad-Djafari, "Microwave imaging of inhomogeneous objects made of a finite number of dielectric and conductive materials from experimental data," *Inv. Problems*, vol. 21, no. 6, pp. S95–S115, Dec. 2005.

[35] F. Santosa, "A level-set approach for inverse problems involving obstacles," *ESIAM: Control, Optim., Calculus of Variations*, vol. 1, pp. 17–33, 1996.

[36] O. Dorn, E. L. Miller, and C. M. Rappaport, "A shape reconstruction method for electromagnetic tomography using adjoint fields and level sets," *Inv. Problems*, vol. 16, no. 5, pp. 1119–1156, Oct. 2000.

[37] R. Ferrayé, J.-Y. Dauvignac, and C. Pichot, "An inverse scattering method based on contour deformations by means of a level set method using

frequency hopping technique," *IEEE Trans. Antennas Propag.*, vol. 51, no. 5, pp. 1100–1113, May 2003.

[38] A. Litman, "Reconstruction by level sets of n-ary scattering obstacles," *Inv. Problems*, vol. 21, no. 6, pp. S131–S152, Dec. 2005.

[39] D. A. Woten, M. R. Hajihashemi, A. M. Hassan, and M. El-Shenawee, "Experimental Microwave Validation of Level Set Reconstruction Algorithm," IEEE Trans. Antennas Propag., vol. 58, no. 1, pp. 230-233, Jan. 2010.

[40] A. N. Tikonov and V. Arsenine, *Solutions of Ill-Posed Problems*. New York: Winston, 1977.

[41] P. Mojabi and J. Lo Vetri, "Overview and classification of some regularization techniques for the Gauss-Newton inversion method applied to inverse scattering problems," *IEEE Trans. Antennas Propag.*, vol. 57, no. 9, pp. 2658–2665, Sept. 2009.

[42] D. W. Winters, B. D. Van Veen, and S. C. Hagness, "A sparcity regularization approach to the electromagnetic inverse scattering problem," *IEEE Trans. Antennas Propag.*, vol. 58, no. 1, Jan. 2010.

[43] M. A. Ali and M. moghaddam, "3D nonlinear super-resolution microwave inversion technique using time domain data," *IEEE Trans. Antennas Propag.*, vol. 58, no. 7, pp. 2372–2336 Jul. 2010.

[44] R. Benjamin, "Synthetic, post-reception focusing in near-field radar," *Proc. EUREL Int. Conf. on the Detection of Abandoned Land Mines: A Humanitarian Imperative Seeking a Tech. Solution*, Oct. 7–9, 1996, pp. 133–137.

[45] R. Benjamin, "Detecting reflective object in reflective medium," U.K. GB 2313969, Dec. 10, 1997.

[46] S. C. Hagness, A. Taflove, and J. E. Bridges, "Two-dimensional FDTD analysis of a pulsed microwave confocal system for breast cancer detection: Fixed-focus and antenna-array sensors," *IEEE Trans. Biomed. Eng.*, vol. 45, pp. 1470–1479, Dec. 1998.

[47] E. C. Fear and M. A. Stuchly, "Microwave system for breast tumor detection," *IEEE Microwave Wireless Compon. Lett.*, vol. 9, pp. 470–472, Nov. 1999.

[48] L. Xu, S. K. Davis, S. C. Hagness, D. W. van der Weide, and B. D. Van Veen, "Microwave imaging via space-time beamforming: Experimental investigation of tumor detection in multilayer breast phantoms," *IEEE Trans. Microwave Theory Tech.*, vol. 52, pt. Part 2, pp. 1856–1865, Aug. 2004.

[49] E. J. Bond, L. Xu, S. C. Hagness, and B. D. Van Veen, "Microwave imaging via space-time beamforming for early detection of breast cancer," in *Proc. IEEE Int. Conf. on Acoust., Speech, and Signal Process. (ICASSP '02)*, May 13–17, 2002, vol. 3, pp. III-2909–III-2912.

[50] Y. Xie, B. Guo, L. Xu, J. Li, and P. Stoica, "Multi-static adaptive microwave imaging for early breast cancer detection," in *Proc. 39th Asilomar Conf. on Signals, Syst. and Comput.*, Nov. 1, 2005, pp. 285–289.

[51] Y. Xie, B. Guo, L. Xu, J. Li, and P. Stoica, "Multistatic adaptive microwave imaging for early breast cancer detection," *IEEE Trans. Biomed. Eng.*, vol. 53, pp. 1647–1657, Aug. 2006.

[52] R. Nilavalan, J. Leendertz, I. J. Craddock, R. Benjamin, and A. Preece, "Breast tumor detection using a flat 16 element array," in *Proc. 16th Int. Symp. on Electromagn. Compat. Topical Meeting on Biomed. EMC*, Zurich, Switzerland, Feb. 2005, pp. 81–84.

[53] M. Klemm, I. J. Craddock, J. A. Leendertz, A. Preece, and R. Benjamin "Radar-based breast cancer detection using a hemispherical antenna array-experimental results" *IEEE Trans. Antennas and Propag.*, vol. 57, no. 6, pp. 1692–1704, Jun. 2009.

[54] E. C. Fear, J. Sill, and M. A. Stuchly, "Experimental feasibility study of confocal microwave imaging for breast tumor detection," *IEEE Trans. Microw. Theory Tech.*, vol. 51, pp. 887–892, Mar. 2003.

[55] J. M. Sill and E. C. Fear, "Tissue sensing adaptive radar for breast cancer detection—experimental investigation of simple tumor models," *IEEE Trans. Microwave Theory Tech.*, vol. 53, pp. 3312–3319, Nov. 2005.

[56] R. Schifini and A. C. Bruno, "Experimental verification of a finite element model used in a magnetic flux leakage inverse problem," *J. Phys.D: Appl. Phys.*, vol. 38, no. 12, pp. 1875–1880, June 2005.

[57] Z. Chen, G. Preda, O. Mihalache, and K. Miya, "Reconstruction of crack shapes from the MFLT signals by using a rapid forward solver and an optimization approach," *IEEE Trans. Magn.*, vol. 38, no. 2, pp. 1025–1028, Mar. 2002.

[58] M. Yan, S. Udpa, S. Mandayam, Y. Sun, P. Sacks, and W. Lord, "Solution of inverse problems in electromagnetic NDE using finite element methods," *IEEE Trans. Magn.*, vol. 34, no. 5,pp. 2924–2927, Sept. 1998.

[59] C. Edwards and S. B. Palmer, "The magnetic leakage field of surface-breaking cracks," *J. Phys. D: Appl. Phys.*, vol. 19, no. 4, pp 657–673, Apr. 1986.

[60] C. Mandache and L. Clapham, "A model for magnetic flux leakage signal Predictions," *J. Phys. D: Appl. Phys.*, vol. 36, no. 20, pp. 2427–2431, Oct. 2003.

[61] D. Minkov, J. Lee, and T. Shoji, "Study of crack inversions utilizing dipole model of a crack and Hall element measurements," *J. Magn. Magn. Mater.*, vol. 217, no. 1, pp. 207–215, Jul. 2000.

[62] D. Minkov, Y. Takeda, T. Shoji, and J. Lee, "Estimating the sizes of surface cracks based on Hall element measurements of the leakage magnetic field and a dipole model of a crack," *J. Appl. Phys. A*, vol. 74, no. 2, pp. 169–176, Feb. 2002.

[63] P. Ramuhalli, L. Udpa, and S. S. Udpa, "Electromagnetic NDE signal inversion by function-approximation neural networks," *IEEE Trans. Magn.*, vol. 38, no. 6, pp. 3633–3642, Nov. 2002.

[64] W. Han and P. Que, "2-D defect reconstruction from MFL signals by a genetic optimization algorithm," *Russian J. of NDT,* vol. 41, no. 12, pp. 809–814, Dec. 2005.

[65] W. Han and P. Que, "Defect reconstruction of submarine oil pipeline from MFL signals using genetic simulated annealing algorithm," *J. Japan Petr. Inst.*, vol. 49, no. 3, pp. 145–150, 2006.

[66] P. Ramuhalli, L. Udpa, and S. S. Udpa, "Neural network-based inversion algorithms in magnetic flux leakage nondestructive evaluation," *J. Appl. Phys.*, vol. 93, no. 10, pp. 8274–8276, May 2003.

[67] A. Joshi, L. Udpa, S. S. Udpa, and A. Tamburrino, "Adaptive wavelets for characterizing magnetic flux leakage signals from pipeline inspection," *IEEE Trans. Magn.*, vol. 42, no. 10, pp. 3168–3170, Oct. 2006.

[68] J. W. Bandler, R. M. Biernacki, S. H. Chen, P. A. Grobelny, and R. H. Hemmers, "Space mapping technique for electromagnetic optimization," *IEEE Trans. Microwave Theory Tech.*, vol. 2, no. 12, pp. 2536–2544, Dec. 1994.

[69] J. W. Bandler, Q. S. Cheng, D. H. Gebre-Mariam, K. Madsen, F. Pedersen, and J. Søndergaard, "EM-based surrogate modeling and design exploiting implicit, frequency and output space mappings," in *IEEE MTT-S Int. Microw. Symp. Dig.*, Philadelphia, PA, June 2003, pp. 1003–1006.

[70] J. W. Bandler, Q. S. Cheng, S. A. Dakroury, A. S. Mohamed, M. H. Bakr, K.Madsen, and J. Søndergaard, "Space mapping: The state of the art," *IEEE Trans. Microwave Theory Tech.*, vol. 52, no. 1, pp. 337–361, Jan. 2004.

[71] D. Echeverria and P.W. Hemker, "Space mapping and defect correction," *CMAM The Int. Mathematical J. Computational Methods in Applied Mathematics,* vol. 5, no. 2, pp. 107–136, 2005.

CHAPTER 2

DESIGN, FABRICATION, AND MEASUREMENT OF A TEM HORN ANTENNA FOR ULTRA-WIDE BAND MICROWAVE BREAST IMAGING

2.1 INTRODUCTION

The design and fabrication of high-performance antennas present significant challenges in the implementation of microwave imaging. An important antenna design requirement is a wide impedance bandwidth. In radar-based techniques, the wide bandwidth is a prerequisite to achieving high fidelity of the radiated pulse. In optimization-based techniques, the frequency-hopping approach is used which employs multi-frequency microwave measurements. It allows for the reconstruction of the permittivity distribution with higher fidelity compared to a single-frequency or narrow-band reconstruction [1]. Other typical design requirements that have been considered in the literature are high directivity as well as small size so that a number of antennas could be positioned around the breast. Various types of antennas have been proposed for tissue-sensing applications. Typical examples include planar monopole [2], slot antenna [3], Fourtear antenna

[4], microstrip patch antenna [5], planar "dark-eyes" [6], and ridged pyramidal horn [7].

For microwave scanning of the breast, the antennas and the tissue are typically immersed in a coupling liquid with dielectric properties as close as possible to the average properties of the breast tissue in the operating frequency band (e.g. see [8]). This medium minimizes the reflections occurring at the skin interface and increases the penetration into the tissue. Optimizing the coupling liquid based on *in vivo* measurement data has been addressed in [8] where the coupling liquid is a mixture of glycerin and water. Also, several liquids have been compared in [9] and the benefits of selecting an oil-based immersion liquid have been discussed. However, the selection of a convenient and practical coupling medium for realistic clinical experiments is still an issue of debate. The coupling medium complicates maintenance and requires replacement to avoid contamination.

In our initial investigations we studied two types of coupling liquids: alcohol [10] and oil-based liquids [11]. Alcohol is convenient for clinical use but it shows high loss which is not suitable for microwave measurements. On the other hand, oil-based liquids have lower loss but they are not convenient for clinical use.

Considering the limitations of using coupling liquids, an ultra-wide band (UWB) TEM horn antenna placed in a partially shielded dielectric medium was proposed. The major design considerations, which distinguishes this antenna from the previously proposed antennas for this application are: (1) elimination of the coupling liquid, (2) directing all radiated power toward the tissue via the front aperture of the antenna, and (3) blocking the electromagnetic interference from the surrounding medium by a carefully designed enclosure consisting of copper sheets and power absorbing sheets. The first requirement ensures that the imaging system is convenient to be used in a clinical environment, i.e., that it is easy to maintain and sanitize after a patient is examined. The second and third requirements are crucial in the detection and characterization of tumors. The antenna also features ultra-wide impedance bandwidth. It is designed to operate in the UWB range allowed by the Federal Communication Commission (FCC) for indoor applications, i.e., 3.1 GHz to 10.6 GHz. The amount of power coupled to the tissue through the front aperture is quantified by a new parameter called near-field directivity (NFD). To compute NFD, instead of computing near-field directivity for each point as proposed in [12], the integration of the real part of the Poynting vector is computed over a surface overlapping the antenna aperture and the result is divided by the total radiated power.

In addition, we investigate the following parameters of the antenna in the UWB range through simulation and measurement: group velocity, fidelity, and efficiency. Novel techniques are presented for estimating the efficiency and the group velocity from measurements suitable for the characterization of antennas operating in direct contact with tissue. The design and characterization of the antenna have been presented in [13]-[20].

2.2 ANTENNA DESIGN AND FABRICATION

The proposed antenna is a TEM horn which is placed in a partially shielded dielectric medium. Since the focus here is on near-field imaging for breast cancer diagnostics, we design the antenna to operate best when attached to a skin layer backed by a tissue layer. This influences the selection of the permittivity of the dielectric material used in the antenna structure and ultimately the antenna dimensions.

Fig. 2.1(a) shows the two plates of the TEM horn which is fed by a coaxial cable via a balun ensuring matched transition to the parallel plates of the horn [21]. Figs. 2.1(b) and 2.1(c) show the top and bottom views of the TEM horn and the balun. The TEM horn is embedded in a solid dielectric medium with permittivity of 10 so that it matches closely the weighted average permittivity of the breast tissue of a radiologically dense breast [22] in the UWB frequency range. This ensures maximum coupling of the microwave power into the imaged body. Also, using such dielectric material eliminates the need for coupling liquids. The material of the dielectric medium is ECCOSTOCK® HiK from Emerson & Cuming Microwave Products [23] with $\varepsilon_r = 10$ and $\tan\delta$ < 0.002 in the frequency range from 1 GHz to 10 GHz. This solid material simplifies the fabrication process significantly. It can be readily machined to make three dielectric pieces (cross-sectional view shown in Fig. 2.1(d)) using carbide tools or by grinding. After placing the copper sheets of the TEM horn (Figs. 2.1(a), 2.1(b), and 2.1(c)) on the middle piece, all three pieces are attached together to form the final shape in Fig. 2.1(e).

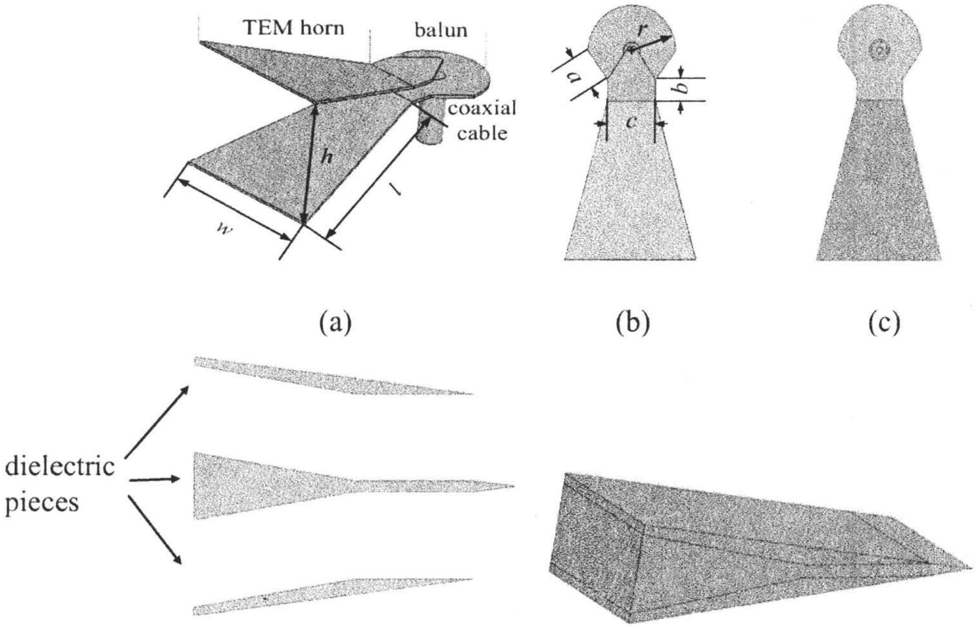

(a) (b) (c)

(d) (e)

Fig. 2.1. (a) The TEM horn with the coaxial feed and the balun. (b) Top view of the TEM horn. (c) Bottom view of the TEM horn. (d) Cross-sectional view of the three antenna pieces machined out of ECCOSTOCK® HiK. (e) After mounting the copper plates of the TEM horn on the middle dielectric piece, all three dielectric parts are glued together.

In order to de-couple the antenna from the outside environment (except the front side), the antenna is shielded with patterned copper sheets as shown in Fig. 2.2. The shapes of the apertures on the top copper sheet have a crucial role in matching the impedance of the antenna to that of the coaxial cable. The top plate of the TEM horn is connected to the top copper sheet with a thin wire to suppress propagating modes between these two plates. The thin wire is along the same axis as the inner wire of the coaxial feed; see Fig. 2.3. Then, a microwave absorbing sheet with $\varepsilon' \approx 30$, $\varepsilon'' \approx 2$, $\mu' \approx 1.7$, and $\mu'' \approx 2.7$ (ECCOSORB FGM-40, Emerson & Cuming Microwave Products [23]) is glued on the top surface of the antenna (on top of the copper sheet) to prevent the coupling of the antenna to the outside environment.

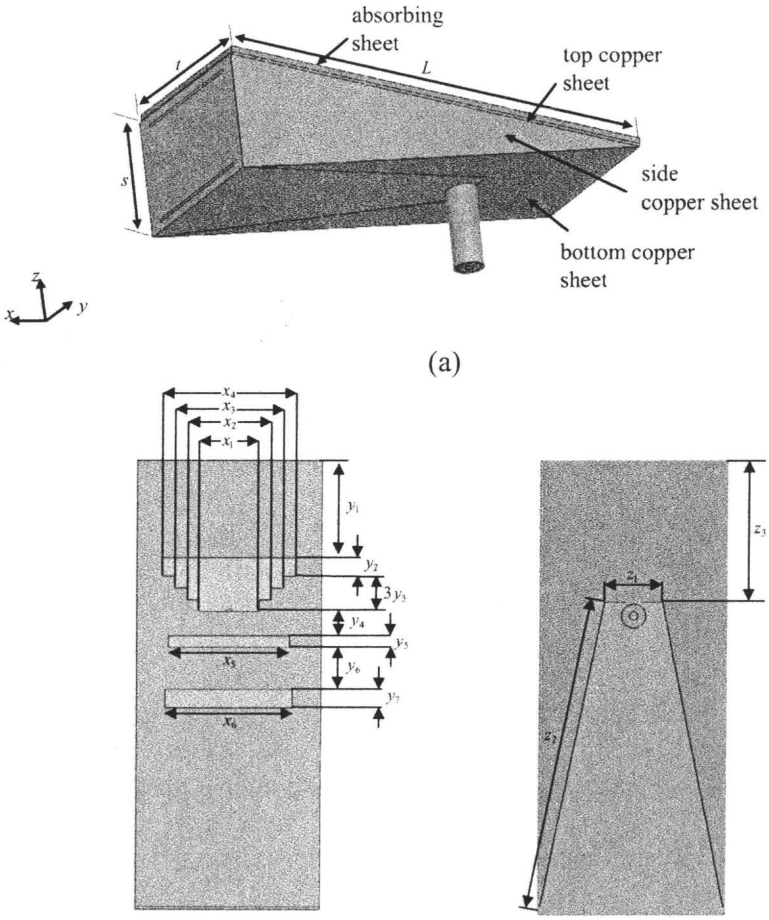

(a)

(b) (c)

Fig. 2.2 (a) The TEM horn placed in a dielectric medium with relative permittivity of 10 with copper sheets on all outer surfaces except the front aperture and a microwave absorbing sheet on the top surface. (b) The copper sheet pattern on the top surface. (c) The copper sheet pattern on the bottom surface.

2.3 ANTENNA PERFORMANCE

Fig. 2.3 shows the simulation set-up where the antenna is assumed to operate in air while its front aperture is attached to a two-layer medium with a skin layer and a tissue layer with the properties shown in Fig. 2.4. The design parameters have been optimized so that the antenna is matched to the 50-Ω coaxial cable in the whole UWB frequency range. We show the performance of the antenna in the frequency domain as well as the time domain.

The frequency-domain simulations are performed with HFSS ver. 11 [24] and the time-domain simulations are performed with CST Microwave Studio [25]. The measurements have been performed on the artificial phantom emulating the human breast. Table 2.1 shows the values for the design parameters of Figs. 2.1 and 2.2. The parameters *L*, *s*, and *t*, which show the overall size of the antenna, are 74 mm, 19 mm, and 30 mm, respectively.

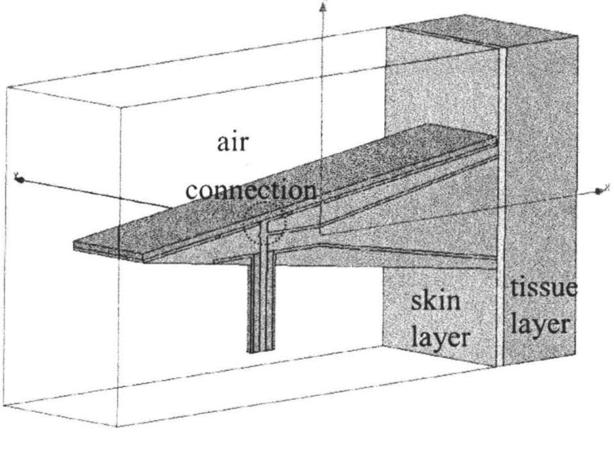

Fig. 2.3. Sliced view of one-half of the simulation set-up.

TABLE 2.1
DESIGN PARAMETERS OF THE ANTENNA

Parameter	Value (mm)	Parameter	Value (mm)
l	38	x_4	10
w	24	x_5	20
h	16	x_6	21
a	8	y_1	16
b	5	y_2	3
c	11	y_3	2
r	11	y_4	4
L	74	y_5	2
s	19	y_6	7
t	30	y_7	3
x_1	22	z_1	9
x_2	18	z_2	52
x_3	14	z_3	23

2.3.1 Return Loss

The antenna geometry is optimized first in HFSS to obtain a return loss below -10 dB in the whole UWB. Then, the final design is also simulated in CST Microwave Studio for validation as well as in order to compute the time-domain performance parameters. The return loss of the antenna is measured when the antenna is attached to a phantom consisting of two layers: a 2 mm thin skin layer and a 5 cm thick tissue layer. These layers are made of glycerin solutions with the properties shown in Fig. 2.4 to emulate the breast tissue. Fig. 2.5 shows the comparison between the simulated and measured results for the return loss of the antenna. The impedance match is good in the UWB frequency range (below -10 dB).

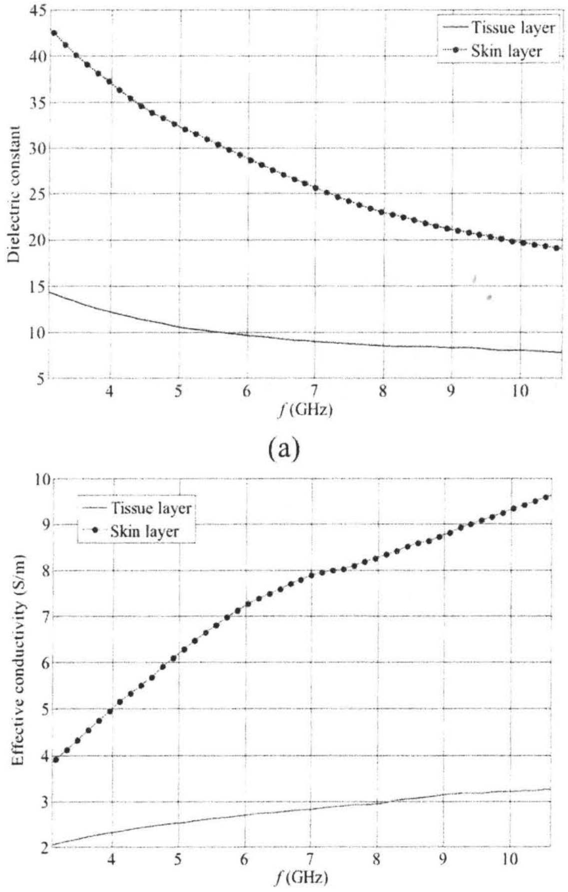

(a)

(b)

Fig. 2.4. Measured constitutive parameters of the tissue and skin layers made of glycerin phantoms: (a) dielectric constant and (b) effective conductivity.

2.3.2 Near-Field Directivity (NFD)

Fig. 2.6 shows the computed NFD factor for the antenna. This factor shows the proportion of the power that is radiated via the front aperture of the antenna. To compute this factor, the normal component of the real part of the Poynting vector is integrated on the surfaces of a cuboid enclosing the antenna with its front surface overlapping the front aperture of the antenna as shown in Fig. 2.3. The total radiated power is obtained from the sum of all these integrations. Then, the power integral over the front surface is divided by the total radiated power to give the NFD factor. Fig. 2.6 shows the computed NFD factor versus frequency. The average NFD factor over the whole band is 93%. It shows that the antenna is decoupled electromagnetically from the outside environment very well while coupling most of the radiated power into the imaged tissue.

2.3.3 Efficiency

We investigate the efficiency of the antenna via simulation and measurement. In order to compute the efficiency via simulation, we divide the total radiated power (computed as described in the previous section over the cuboid surface shown in Fig. 2.3) by the power fed to the antenna. The power fed to the antenna is computed as the power incident on the coaxial port minus the reflected power at that port.

In order to have an experimental estimation of the antenna efficiency, two identical antennas are attached together front-to-front as shown in Fig. 2.7. The received-to-transmitted power ratio P_r/P_t is

$$\frac{P_r}{P_t} = (1-|\Gamma_r|^2)\cdot(1-|\Gamma_t|^2)\cdot e_r \cdot e_t \cdot D_r \cdot D_t \qquad (2.1)$$

where Γ_r and Γ_t are the return losses for the two antennas, e_r and e_t are their efficiencies, and D_r and D_t are their NFD factors. In a measurement with a vector network analyzer (VNA), the two antennas' coaxial feeds represent the two ports where $|S_{21}|^2 = P_r / P_t$, $|S_{11}| = \Gamma_t$, and $|S_{22}| = \Gamma_r$. The efficiency of one antenna is obtained as

$$e_A = \frac{|S_{21}|}{\sqrt{(1-|S_{22}|^2)(1-|S_{11}|^2)\cdot \mathrm{NFD}}}. \tag{2.2}$$

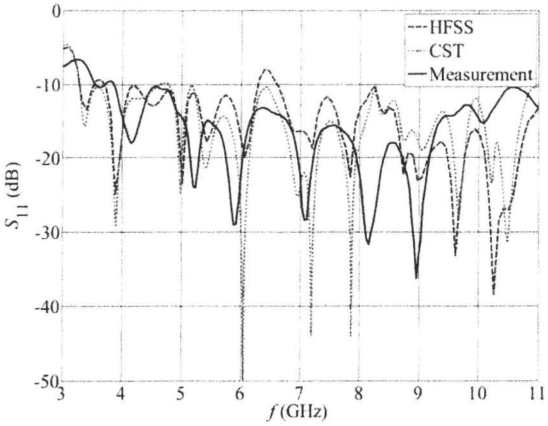

Fig. 2.5. Return loss of the antenna obtained from HFSS and CST simulations and measurement.

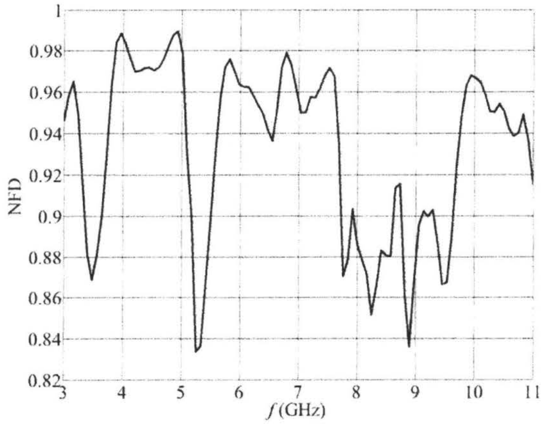

Fig. 2.6. Simulated NFD factor of the antenna.

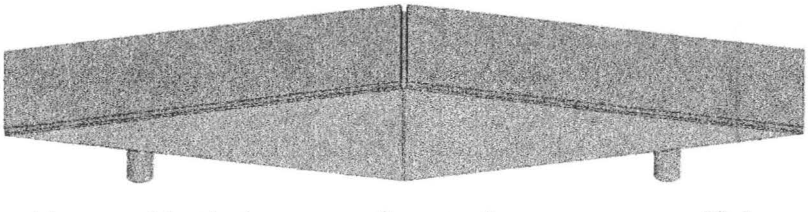

Fig. 2.7. Attaching two identical antennas front-to-front to measure efficiency and group velocity.

In the above formula, while the *S*-parameters are measured, the NFD factor is simulated (see Fig. 2.6).

Fig. 2.8 compares the antenna efficiency obtained from simulation and measurement over the UWB frequency range. The average of the efficiency over the whole band in the case of the simulation and the measurement is 40% and 32%, respectively. Considering the efficiency together with the NFD factor, this indicates that the overall coupling efficiency of the proposed antenna to the imaged medium via the front aperture is much better than that of existing low-directivity UWB antennas whose average radiation efficiencies are of comparable values; for example, see [6]. We emphasize that such low-directivity UWB antennas direct only a fraction of the radiated power toward the imaged region.

2.3.4 Group Velocity

We estimate the group velocity of the antenna via measurements. The variation of the group velocity with frequency is a measure of the distortion of the transmitted pulse due to the antenna. We use S_{21} in the same measurement set-up as shown in Fig. 2.7. We express S_{21} as

$$S_{21} = \frac{V_2}{V_1} = e^{-(\alpha_1 + j\beta_1)L_1} e^{-(\alpha_2 + j\beta_2)L_2} \tag{2.3}$$

where V_2 and V_1 are the assumed voltages at the two-antenna terminals, β_2 and β_1 are the phase constants associated with the signal delay in each antenna, α_1 and α_2 are the respective attenuation constants, and L_2 and L_1 are the lengths of the antennas from the coaxial feed point to the center of the aperture. Since the two antennas are assumed identical, we define α_A, β_A, and L_A as $\alpha_2 = \alpha_1 = \alpha_A$, $\beta_2 = \beta_1 = \beta_A$, and $L_1 = L_2 = L_A$. Thus, (2.3) becomes $S_{21} = e^{-2\alpha_A L_A} \cdot e^{-j2\beta_A L_A}$. We introduce θ_{21} as the angle of S_{21}, $\theta_{21} = 2\beta_A L_A$. Then the group velocity v_g is obtained as

$$v_g = \left(\frac{\partial \beta_A}{\partial \omega}\right)^{-1} = \frac{1}{2L_A}\left(\frac{\partial \theta_{21}}{\partial \omega}\right)^{-1}. \tag{2.4}$$

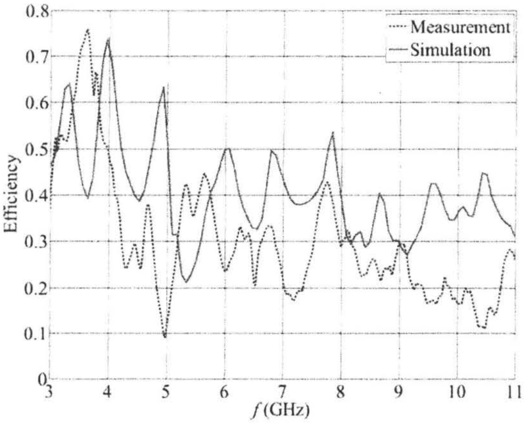

Fig. 2.8. Simulated and measured efficiencies of the antenna.

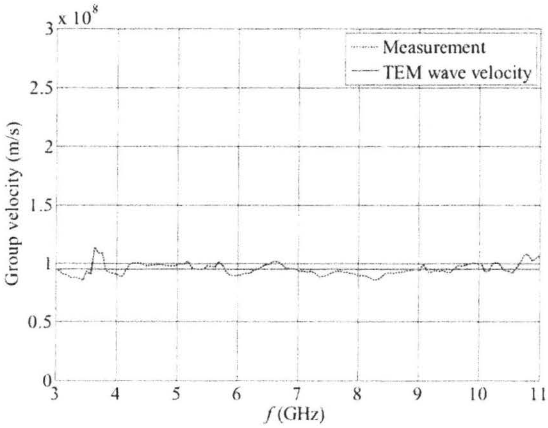

Fig. 2.9. Group velocity obtained from measurement compared to the wave velocity in a medium with permittivity of 10, $v_{\text{TEM}} \approx 0.9 \times 10^8$ m/s.

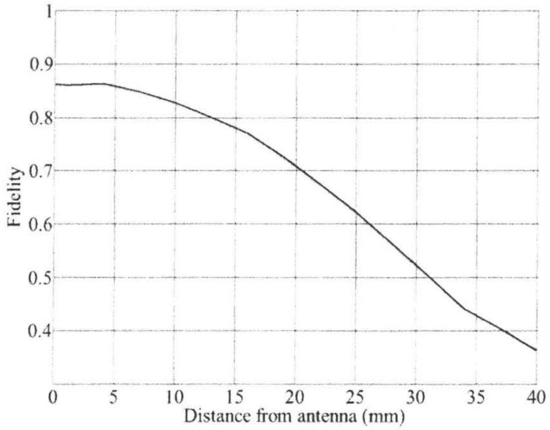

Fig. 2.10. Simulated fidelity versus the distance from the center of the antenna aperture and along the aperture normal.

Fig. 2.9 shows the group velocity computed from measured results. It is compared with the velocity of the wave in the antenna dielectric medium with permittivity of 10.

2.3.5 Fidelity

In order to investigate the distortion of the pulses by the proposed antenna into homogenized breast tissue, the antenna fidelity is computed. The fidelity is the maximum magnitude of the cross-correlation between the normalized observed response and an ideal response derived from the excitation waveform at the antenna terminals [26],

$$F = \max_{\tau} \int_{-\infty}^{\infty} \hat{f}(t)\hat{r}(t+\tau)dt \tag{2.5}$$

where $\hat{r}(t)$ is the observed E-field normalized to unit energy, and $\hat{f}(t)$ is the input signal at the antenna terminals also normalized to unit energy. Fig. 2.10 shows the computed fidelity of the antenna. It is seen that the fidelity of the signal is maximum close to the antenna and decreases with distance. The reason for the drop in the fidelity with distance is the tissue dispersion and dissipation.

2.4 SUMMARY

In this chapter, a novel UWB TEM horn antenna placed in a dielectric medium has been proposed for microwave imaging in breast cancer detection. The outer surface of the antenna is covered by copper sheets and a microwave absorbing sheet. The design is accomplished through full-wave simulation and then experimentally tuned for best impedance match. Simulated and experimental results confirm that the following design requirements are met: (1) The antenna does not need to be immersed in a coupling liquid. (2) The near-field power is directed entirely toward the tissue through the front aperture of the antenna. (3) Excellent isolation from external electromagnetic interference (EMI) is achieved. (4) Good impedance match in the UWB frequency range is achieved.

This antenna enables the development of practical imaging systems which will be easy to maintain in a clinical environment. Such systems will allow for convenient and fast sanitation of the equipment after a patient is examined. Furthermore, the specifications stated in (2) and (3) are crucial for the sensitivity and the EMI immunity of the microwave breast imaging system that have not been properly addressed in previously reported works. This antenna is intended to be used in a microwave breast tomography system although it may be also a good candidate for radar-based imaging.

REFERENCES

[1] W. C. Chew and J. H. Lin, "A frequency-hopping approach for microwave imaging of large inhomogeneous bodies," *IEEE Microwave Guided Wave Lett.*, vol. 5, no. 12, pp. 439–441, Dec. 1995.

[2] H. M. Jafari, M. J. Deen, S. Hranilovic, and N. K. Nikolova, "A study of ultrawideband antennas for near-field imaging," *IEEE Trans. Antennas and Propag.*, vol. 55, no. 4, pp. 1184–1188, Apr. 2007.

[3] H. M. Jafari, J. M. Deen, S. Hranilovic, and N. K. Nikolova, "Co-polarised and cross-polarised antenna arrays for breast, cancer detection," *IET Microwave Antennas Propag.*, vol. 1, no. 5, pp. 1055–1058, Oct. 2007.

[4] D. A. Woten and M. El-Shenawee, "Broadband dual linear polarized antenna for statistical detection of breast cancer," *IEEE Trans. Antennas and Propag.*, vol. 56, no. 11, pp. 3576-3580, Nov. 2008.

[5] R. Nilavalan, I. J. Craddock, A. Preece, J. Leendertz, and R. Benjamin, "Wideband microstrip patch antenna design for breast cancer tumour detection," *IET Microwave Antennas Propag.*, vol. 1, no. 2, pp. 277–281, Apr. 2007.

[6] H. Kanj and M. Popovic, "A novel ultra-compact broadband antenna for microwave breast tumor detection," *Progress In Electromagnetics Research*, PIER 86, pp. 169–198, 2008.

[7] X. Li, S. C. Hagness, M. K. Choi, and D. Van Der Weide, "Numerical and experimental investigation of an ultra-wideband ridged pyramidal-horn antenna with curved launching plane for pulse radiation," *IEEE Antennas Wirel. Propag. Lett.*, vol. 2, pp. 259–262, 2003.

[8] P. M. Meaney, M. W. Fanning, T. Raynolds, C. J. Fox, Q. Fang, C. A. Kogel, S. P. Poplack, and K. D. Paulsen, "Initial clinical experience with microwave breast imaging in women with normal mammography," *Acad Radiol.*, vol. 14, no. 2, pp. 207–218, Feb. 2007.

[9] J. M. Sill and E. C. Fear, "Tissue sensing adaptive radar for breast cancer detection: study of immersion liquids," *Electron. Lett.*, vol. 41, no. 3, pp. 113–115, 2005.

[10] A. Trehan, R. K. Amineh, M. S. Georgiev, and N. K. Nikolova, "Photogrammetry-based surface reconstruction for improving microwave breast tumor detection," *24th Int. Review of Progress in Applied Computational Electromagnetics (ACES)*, Canada, 2008.

[11] A. Trehan, R. K. Amineh, M. S. Georgiev, and N. K. Nikolova, "Accuracy assessment of photogrammetry surface reconstruction for improving microwave imaging," *IEEE Int. Symp. on Antennas and Propag. and USNC/URSI National Radio Science Meeting (AP-S/URSI)*, USA, 2008.

[12] J. Odendaal, J. Joubert, and M. J. Prinsloo, "Extended edge wave diffraction model for near-filed directivity calculations of horn antennas," *IEEE Trans. Instrument. and Measur.*, vol. 54, no. 6, pp. 2469–2473, Dec. 2005.

[13] R. K. Amineh, A. Trehan, and N. K. Nikolova, "TEM horn antenna for ultra-wide band microwave breast imaging," *Progress In Electromagnetics Research B (PIER B)*, vol. 13, pp. 59–74, 2009.

[14] R. K. Amineh, M. Ravan, A. Trehan, and N. K. Nikolova, "Near-field microwave imaging based on aperture raster scanning with TEM horn antennas," submitted to *IEEE Trans. Antennas and Propag.*

[15] R. K. Amineh, M. Ravan, A. Trehan, and N. K. Nikolova, "Microwave imaging for breast cancer diagnosis based on planar aperture scanning," *IEEE Int. Symp. on Antennas and Propag. and USNC/URSI National Radio Science Meeting (AP-S/URSI)*, Canada, 2010.

[16] R. K. Amineh, M. Ravan, A. Trehan, and N. K. Nikolova, "Microwave imaging for breast cancer diagnosis based on planar aperture scanning," *IEEE Int. Symp. on Antennas and Propag. and USNC/URSI National Radio Science Meeting (AP-S/URSI)*, Canada, 2010.

[17] R. K. Amineh and N. K. Nikolova, "Design, fabrication, and characterization of ultra-wide band TEM horn for microwave imaging," *14th Int. Symp. on Antenna Tech. and Applied Electromagnetics and the Canadian Radio Sciences Meeting (ANTEM/AMEREM)*, Canada, 2010.

[18] R. K. Amineh, M. Ravan, A. Trehan, and N. K. Nikolova, "Near-field microwave imaging based on planar aperture scanning," *IEEE MTT Int. Microwave Symp. (IMS)*, USA, 2010.

[19] R. K. Amineh, A. Trehan, and N. K. Nikolova, "Ultra-wide band TEM horn antenna for microwave imaging of the breast," *IEEE Int. Symp. on Antennas and Propag. and USNC/URSI National Radio Science Meeting (AP-S/URSI)*, USA, 2009.

[20] R. K. Amineh, A. Trehan, and N. K. Nikolova, "Ultra-wide band TEM horn antenna designed for microwave imaging of the breast," 13th *Int. Symp. on Antenna Tech. and Applied Electromagnetics and the Canadian Radio Sciences Meeting (ANTEM/URSI)*, Canada, 2009.

[21] K. Chung, S. Pyun, and J. Choi, "Design of an ultrawide-band TEM horn antenna with a microstrip-type balun," *IEEE Trans. Antennas and Propag.*, vol. 53, no. 10, pp. 3410–3413, Oct. 2005.

[22] M. Lazebnik, L. McCartney, D. Popovic, C. B. Watkins, M. J. Lindstrom, J. Harter, S. Sewall, A. Magliocco, J. H. Booske, M. Okoniewski, and S. C. Hagness, "A large-scale study of the ultrawide band microwave dielectric properties of normal breast tissue obtained from reduction surgeries," *Phys. Med. Biol.* , vol. 52, pp. 2637–2656, May 2007.

[23] Emerson & Cuming Microwave Products, http://www.eccosorb.com.

[24] Ansoft Corporation, USA, http://www.ansoft.com.

[25] CST Computer Simulation Technology AG., http://www.cst.com.

[26] D. Lamensdorf and L. Susman, "Baseband-pulse-antenna techniques," *IEEE Antennas Propag. Mag.*, vol. 36, no. 1, pp. 20–30, Feb. 1994.

CHAPTER 3

APERTURE RASTER SCANNING SETUP FOR NEAR-FIELD MICROWAVE IMAGING

3.1 INTRODUCTION

We test the antenna performance as a microwave sensor in an aperture scanning setup to detect embedded targets inside a lossy dielectric body. We examine various scenarios from high-contrast targets in homogeneous phantoms to low-contrast tumors in a heterogeneous breast model. The former case is investigated as a general imaging scenario for hidden targets in dielectric bodies although there are many examples in the literature for breast imaging where normal tissue is assumed to be homogeneous and the tumors have large contrasts (e.g., see [1]-[8]). The latter case gives a realistic insight into the efficiency of the scanning technique as it considers both large and small contrasts. The work in this chapter has been presented in [9]-[12].

3.2 IMAGING SETUP

As shown in Fig. 3.1, a simulant of the breast tissue layer with the properties shown in Fig. 2.4 is compressed between two very thin parallel plates.

A slight compression of the breast between two rigid parallel plates would prevent undesired movement during the microwave measurements. Then, two antennas, one transmitting and the other receiving, perform a two-dimensional (2-D) scan by moving together along the opposite sides of the compressed breast. We note that tissue compression is applied in X-ray mammography (severe compression) and MRI (slight compression). Compression is employed in X-ray mammography mostly to increase sensitivity while in MRI it is used to immobilize the tissue during data acquisition. Movement may cause blurring and measurement errors.

The imaging setup has the following advantages for breast imaging. (1) The imaging setup does not require coupling liquid. Thus, the imaging system would be convenient for clinical use, i.e., it would be easy to sanitize after a patient is examined. (2) The transmitter (or receiver) antenna couples (or measures) practically all microwave power directly in (or from) the tissue through its front aperture due to an excellent NFD. This eliminates interference from the outside environement. (3) The image generation is simple. The transmission *S*-parameter $S_{21}^{\text{back}}(y,z)$ between the two antennas when no scatterer is present (background medium only) at the position (*y*,*z*) is acquired. To obtain the calibrated transmission *S*-parameter $S_{21}^{\text{cal}}(y,z)$, $S_{21}^{\text{back}}(y,z)$ is subtracted from measured transmission *S*-parameter $S_{21}^{\text{meas}}(y,z)$

$$S_{21}^{\text{cal}}(y,z) = S_{21}^{\text{meas}}(y,z) - S_{21}^{\text{back}}(y,z). \qquad (3.1)$$

The images are plots of $|S_{21}^{\text{cal}}(y,z)|$. (4) The coupling between the antennas is optimal in such scanning setup.

In this example, $S_{21}^{\text{back}}(y,z)$ is the same for all (y,z) positions, because the background medium is homogeneous. However, the same calibration can be applied with heterogeneous background where S_{21}^{back} would depend on the position. Also, here the separation distance between the two antennas is set at 3 cm. At such distance, the coupling between the two antennas is sufficiently strong to obtain reasonable signal-to-noise ratio (SNR) with conventional test instruments, e.g., vector network analyzer. In a practical breast-scanning scenario, separation distances anywhere between 8 and 12 cm are necessary in order to avoid patient discomfort. Such a system would require low-noise amplifiers and controlled environment in order to achieve good dynamic range especially at the high-frequency end.

We investigate the capability of this setup to produce images through aperture scanning with the proposed antennas. This is first done through HFSS simulations. A flat tissue layer with the properties shown in Fig. 2.4 and dimensions of $140 \text{ mm} \times 140 \text{ mm} \times 30 \text{ mm}$ is covered by two layers of skin on the top and the bottom sides and is scanned by two antennas. The thin support plates that are supposed to compress slightly the breast are ignored here since their effect will be eliminated through the calibration process. We embed 5 tumor simulants in the breast tissue layer with various shapes as shown in Fig. 3.1. Table 3.1 shows their position and dielectric properties. The latter are assumed frequency-independent in this example. This allows us to monitor the tumor responses with different contrasts in electrical properties with respect to the background. The S_{21} parameter is acquired on an area of $100\text{ mm}\times 100\text{ mm}$ where the sampling rate is 5 mm. Figs. 3.2(a), (b), and (c) show the images obtained from $|S_{21}^{\text{cal}}(y,z)|$ at 5 GHz, 7 GHz, and 9 GHz. These images show that the tumor simulants can be easily detected especially at 5 and 7 GHz. It is observed that while the tumors have been detected, their shape can not be determined. This is expected because the tumor simulants are electrically too small. However, larger tumors appear as larger bright spots in the images even if their permittivity contrast with respect to the background is lower (compare tumors 4 and 5 with tumor 1). Another interesting observation is that at 7 GHz the image of tumor 4, which has only permittivity contrast but no conductivity contrast with the background, appears larger than the image of tumor 2, which has the same size and shape but has contrast in both permittivity and conductivity.

Here, it is worth noting that images can be generated using only magnitude information according to

$$|S_{21}^{\text{cal}}(y,z)|=|S_{21}^{\text{meas}}(y,z)|-|S_{21}^{\text{back}}|. \tag{3.2}$$

However, instead of sharp spots, the tumor simulants appear as doughut shapes. Ignoring the phase information has a negative effect on the image quality. In the next section, we improve the quality of the images using a blind de-convolution technique.

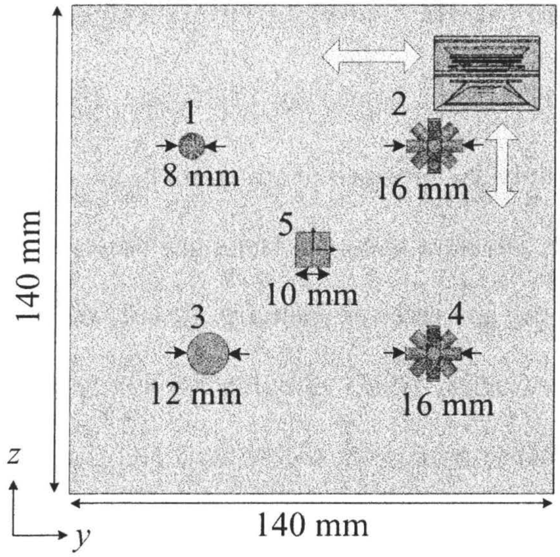

(a)

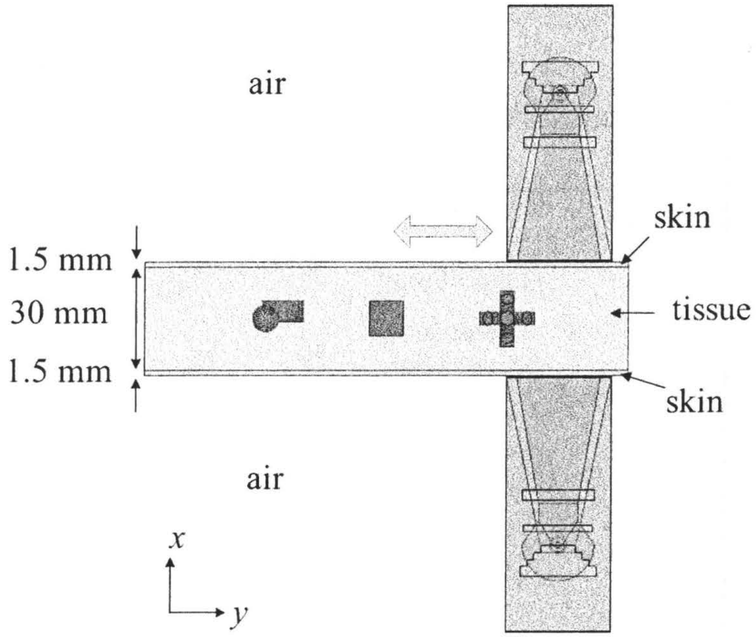

(b)

Fig. 3.1. The proposed planar microwave imaging setup to detect tumors inside a breast phantom including the compressed phantom and two UWB antennas: (a) top view, (b) side view. Large arrows show the scanning axes.

3.3 APPLYING BLIND DE-CONVOLUTION TO DE-BLUR THE IMAGES

Although the images formed by $|S_{21}^{\text{cal}}(y,z)|$ discussed in the previous section clearly identify the presence of scatterers in the tissue, they suffer from significant blurring. The most important factor that causes the blurring is the non-point-wise transmitter and receiver apertures. In fact, the antenna aperture acts like an averaging window, which gives approximately the integration of the power over the antenna aperture in each central (y,z) position. This integration effect is actually a convolution (filtering) in the spatial domain. This effect can be reduced with blind de-convolution.

TABLE 3.1
SHAPE, SIZE, ELECTRICAL PROPERTIES AND POSITION OF THE TUMOR SIMULANTS IN FIG. 3.1

Tumor No.	Shape & Size	ε_r	σ (S/m)	Position (mm)
1	sphere radius=4 mm	50	5	(0,-35,30)
2	irregular radius=8 mm	50	5	(0,35,30)
3	cylinder radius=6 mm height=6 mm	50	5	(0,-35,-30)
4	irregular radius=8 mm	50	3	(0,35,-30)
5	cuboid side=10 mm	30	5	(0,0,0)

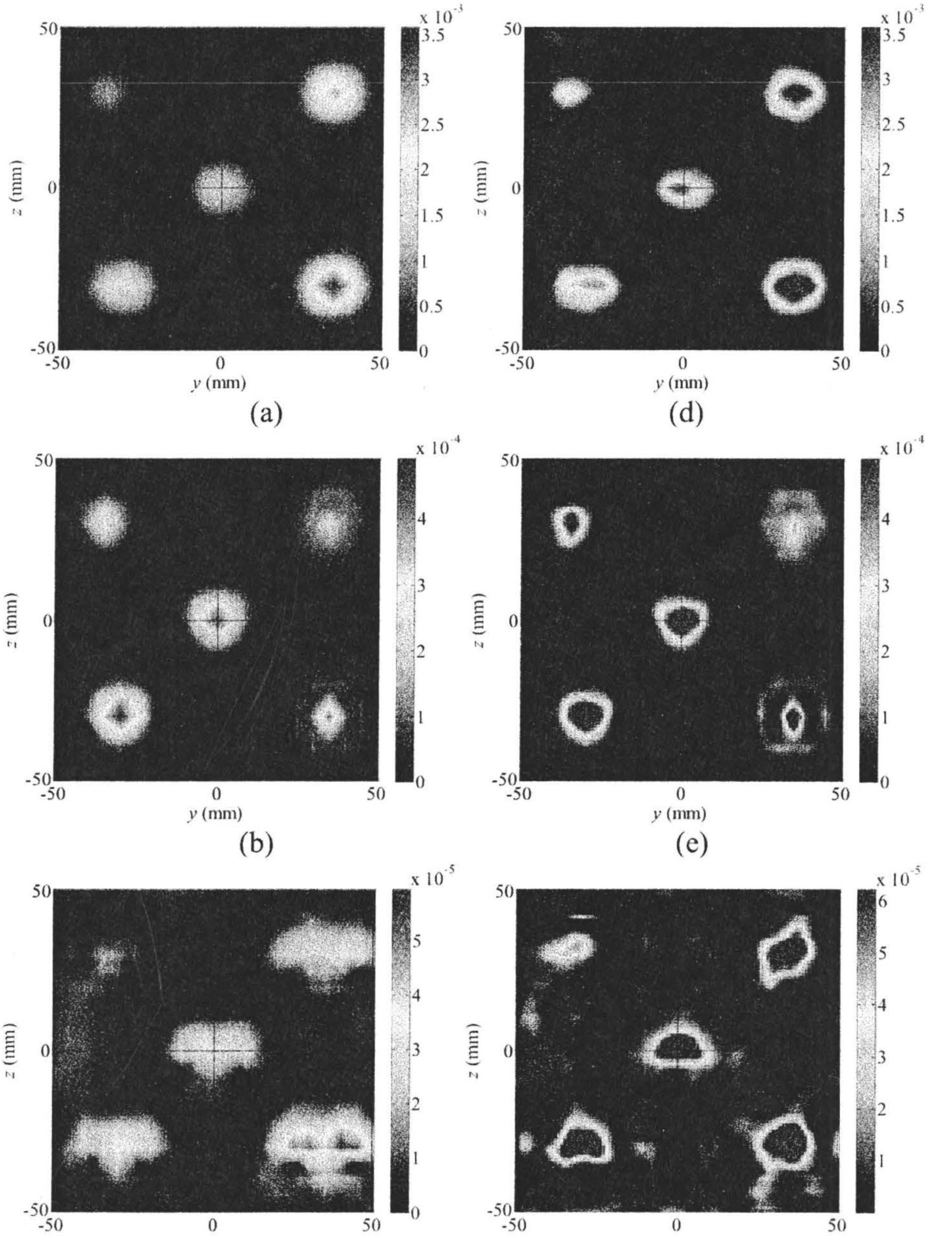

Fig. 3.2. The simulated $|S_{21}^{\text{cal}}|$ images from 2-D scanning at: (a) 5 GHz, (b) 7 GHz, and (c) 9 GHz. The de-blurred images after applying blind de-convolution at: (d) 5 GHz, (e) 7 GHz, and (f) 9 GHz.

In blind de-convolution, it is assumed that the original unknown image $f(y,z)$ has been convolved with a point spread function (PSF), $u(y,z)$, to create a blurred image $g(y,z)$,

$$g(y,z) = f(y,z) * u(y,z) \tag{3.3}$$

where $*$ denotes two-dimensional convolution. The aim in blind image de-convolution is to estimate the original image $f(y,z)$ when the blurred image $g(y,z)$ is known and the PSF is unknown or partially known [13].

Here, we have the blurred image $g(y,z)=|S_{21}^{\text{cal}}(y,z)|$ from the measurement. We assume that the integrating effect occurs non-evenly over the antenna aperture. Thus, we use the simulated distribution of the normal component (x-component) of the Poynting vector at the antenna aperture as the weighting coefficients for the integration effect at each frequency. This becomes the initial guess for the PSF. It needs to be further corrected since: 1) the distribution of the x-component of the Poynting vector over the antenna aperture depends on the tissue properties in front of the antenna, 2) the integration of the power entering the antenna via the front aperture will not be exactly equal to the power that reaches the antenna port, and 3) in practice, the distribution of $u(y,z)$ would be slightly different from the one obtained via simulation due to inevitable differences between the simulated antenna model and the fabricated antenna. Here, we use accelerated damped Lucy Richardson algorithm [14] in the MATLAB image processing toolbox [15]. The algorithm restores the original image $f(y,z)$ and the point-spread function (PSF) simultaneously in each iteration in order to maximize the likelihood between the resulting original image, when convolved with the resulting PSF and the blurred image. Figs. 3.2(d)-(f) show the de-blurred images after applying blind de-convolution. It is clear that in these images tumors appear with much better contrast compared to the raw images of Figs. 3.2(a)-(c). Also, the spatial spans of the tumors have been restored in the de-blurred images especially at 9 GHz.

3.4 MEASUREMENTS OF A HOMOGENEOUS PHANTOM

A homogeneous flat phantom is prepared out of glycerin with a thickness of 3 cm and two scaterrers are placed inside. Fig. 3.3 shows the constitutive parameters of the two embedded scatterers, denoted as Sc1 and Sc2, as well as those of the homogeneous background phantom. Sc1 is made of alginate powder while Sc2 is made of glycerin. The background medium is also glycerin-based but the recipe is different from that for Sc2. Table 3.2 shows the positions, sizes, and the type of materials for Sc1 and Sc2. Two identical antennas with the parameters shown in the previous sections are used to perform a 2-D scan of the compressed phantom between two thin glass sheets. With spatial sampling rates of 5 mm in both y and z directions, the S-parameters at the two antenna terminals are measured utilizing an Advantest R3770 VNA. Figs. 3.4(a)-(c) show the images obtained after calibration (as described by (3.1)) at 5 GHz, 7 GHz, and 9 GHz. Sc1, which has larger contrast in the dielectric properties than Sc2, produces a brighter larger spot in the images. We also note that diffusion of the alginate powder into the homogeneous phantom makes the effective size of Sc1 larger. After insertion into the background medium, the constitutive parameters of the center of Sc1 are those reported in Fig. 3.3; however, they gradually transition into the properties of the background medium away from the center.

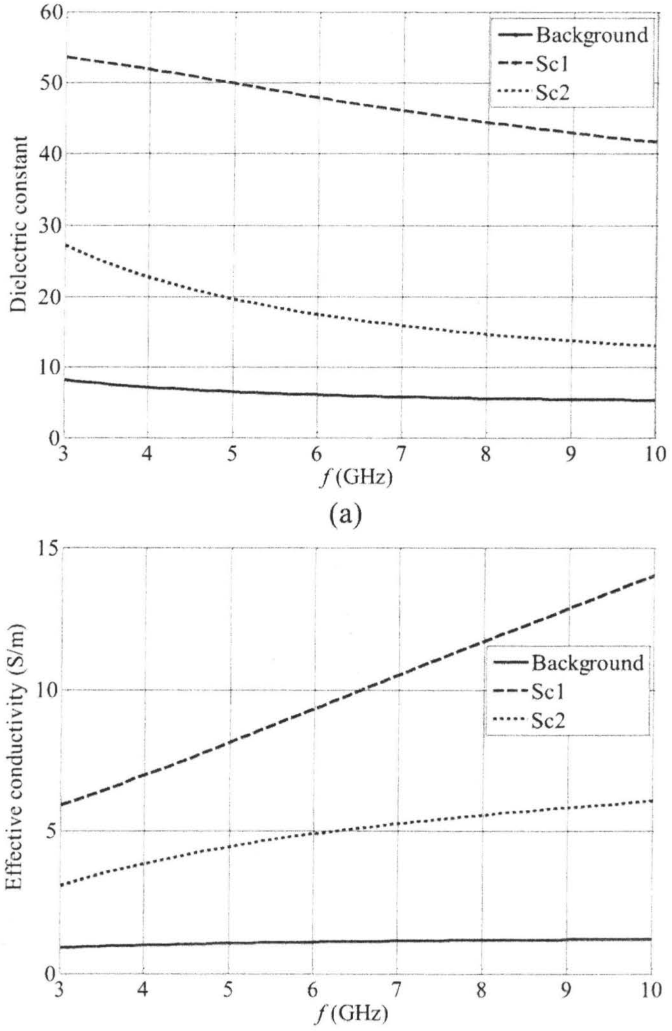

(a)

(b)

Fig. 3.3. Measured constitutive parameters for the background medium and the two scatterers: (a) dielectric constant, (b) effective conductivity.

TABLE 3.2
POSITION (IN THE Y-Z PLANE), SIZE, AND MATERIAL TYPE FOR THE TWO SCATTERERS EMBEDDED IN THE EXPERIMENTAL HOMOGENEOUS PHANTOM

Scatterer	Position (mm)	Size (mm)	Material
Sc1	(-4,25)	$10\times10\times10$ [before diffusion]	alginate powder
Sc2	(9,-25)	$15\times15\times15$	glycerin

In order to perform blind de-convolution on the raw images, we first simulate one antenna with the thin glass sheet and the homogeneous phantom to get the initial guess for the PSF at each frequency as described in section 3.3. Then, we apply the blind de-convolution algorithm to improve the image quality as shown in Figs. 3.4(d)-(f).

3.5 SIMULATION RESULTS FOR HETEROGENEOUS BREAST MODEL

So far we have investigated the capability of the proposed scanning setup in detecting targets embedded in homogeneous background media. However, in applications such as breast tumor detection, the host medium is not homogeneous. Here, we examine the raster scanning with the proposed antenna for a heterogeneous breast model. This model is obtained by converting MRI intensity images into several tissues including: fat, trans-fat, fibro-glandular, and muscle. The skin layer is then created artificially in the simulation model to envelop tightly the MRI-based model. Fig. 3.5(a) shows the simulation setup containing two identical antennas and the heterogeneous flattened breast model with a thickness of 3 cm. We then insert three tumor simulants with the shapes shown in

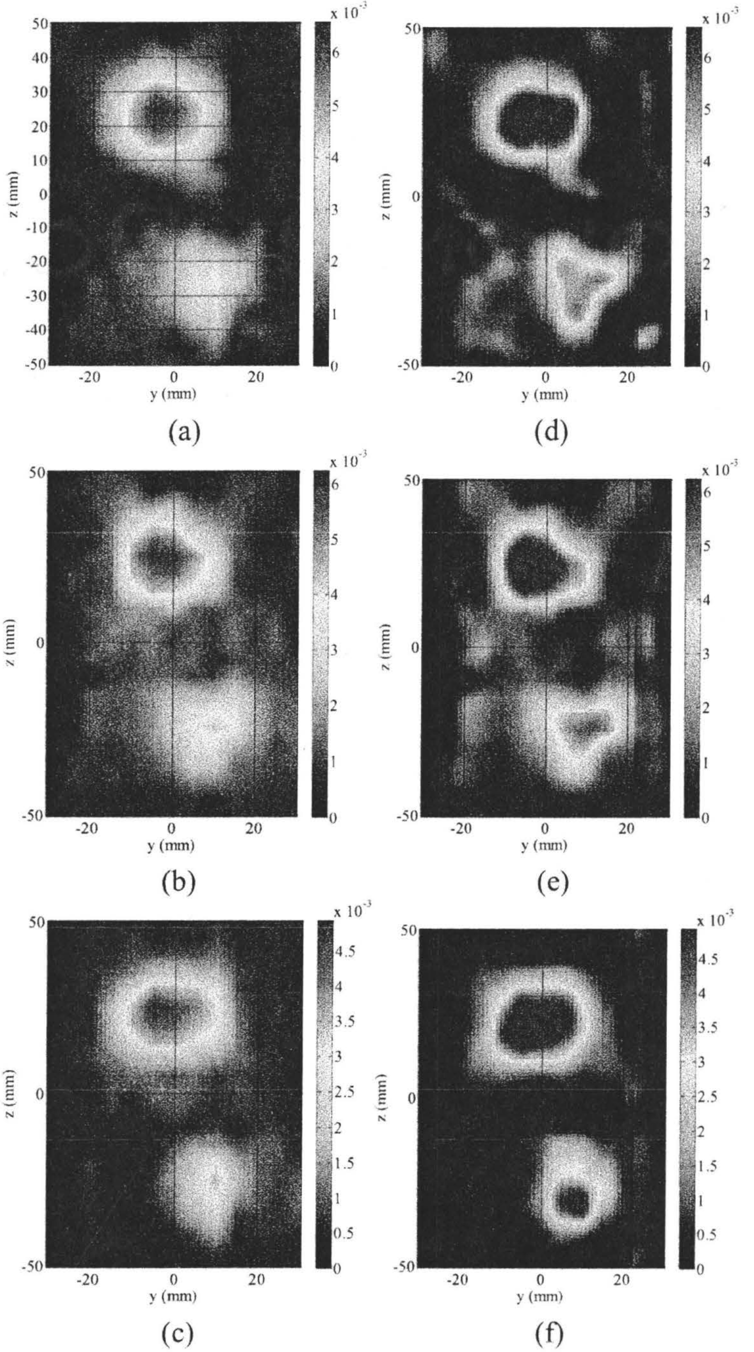

Fig. 3.4. The measured $|S_{21}^{\text{cal}}|$ images from 2-D scanning at: (a) 5 GHz, (b) 7 GHz, and (c) 9 GHz. The de-blurred images after applying blind de-convolution to the images at: (d) 5 GHz, (e) 7 GHz, and (f) 9 GHz.

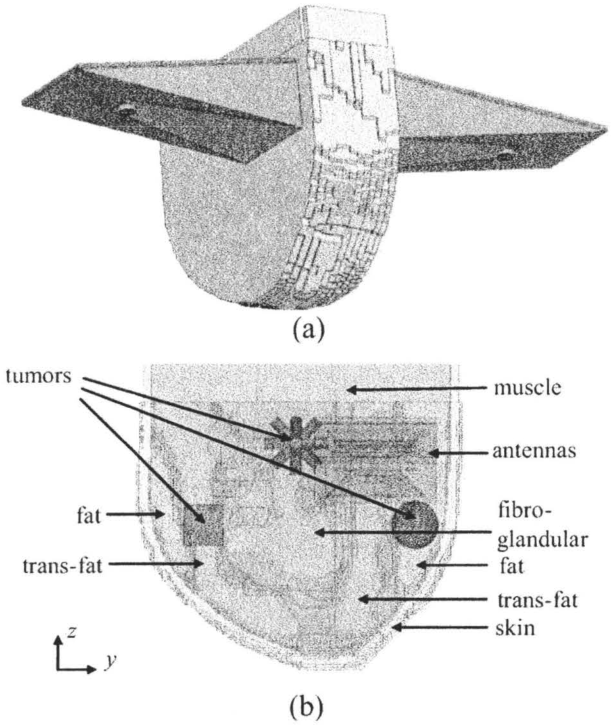
(a)

(b)

Fig. 3.5. (a) Scanning compressed heterogeneous breast model by two antennas (b) Three tumor simulants embedded at the positions (-23,-40) mm, (30,-40) mm, and (0,-20) mm in the trans-fat, fibro-glandular, and fat tissues, respectively.

the cross-sectional view of Fig. 3.5(b) in various tissues. The tumor in fat is at the position (30,-40) mm in the *y*-*z* plane. The tumor in trans-fat is at the position (-23,40) mm in the *y*-*z* plane. The tumor in fibro-glandular tissue is at the position (0,-20) mm in the *y*-*z* plane. Fig. 3.6 shows the electrical properties assigned to the tissues which are extracted from [16] and [17]. Also, the properties shown in Fig. 2.4 are assigned to the skin layer. The tumor in the fibro-glandular tissue has the lowest contrast (about 50:43 in permittivity and 4.7:4 in conductivity at 5 GHz and similar contrasts at other frequencies) while the tumor in the fat has the largest contrast (about 50:5 in permittivity and 4.7:0.45 in conductivity at 5 GHz and similar contrasts at other frequencies).

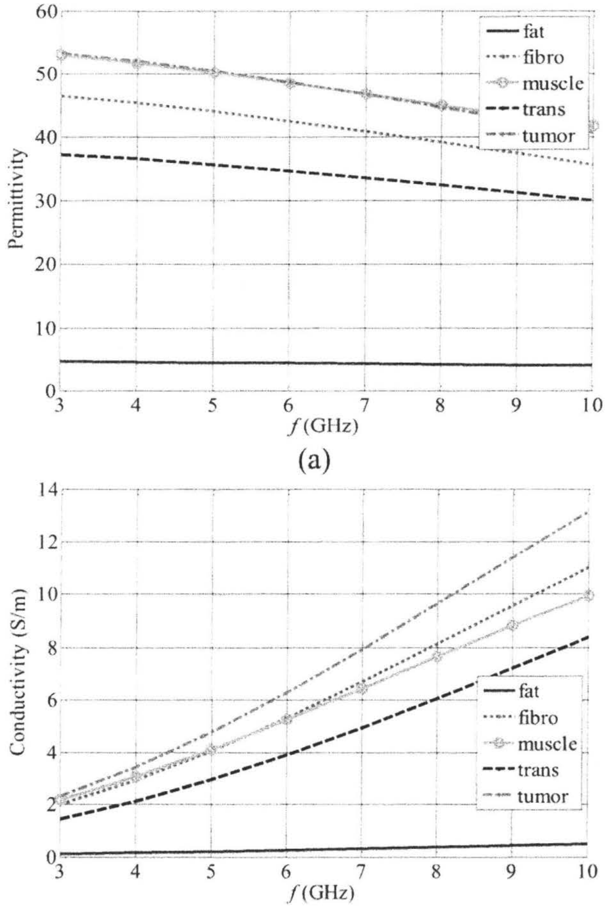

(a)

(b)

Fig. 3.6. Permittivity and conductivity of the heterogeneous breast model.

Using the calibrated data (as described in (3.1)), the raw images shown in Figs. 3.7(a)-(c) are obtained. The images show that all three tumors can be detected at 5 GHz. At 7 GHz two of the tumors are clearly visible (that in the fat and the one in the trans-fat). However, at 9 GHz only the tumor embedded in the fat tissue can be detected. This is the case of the highest contrast. The reduced detection capability at 9 GHz is due to the degradation of the numerical SNR at high frequencies. Here, we define the numerical SNR as the ratio of the signal

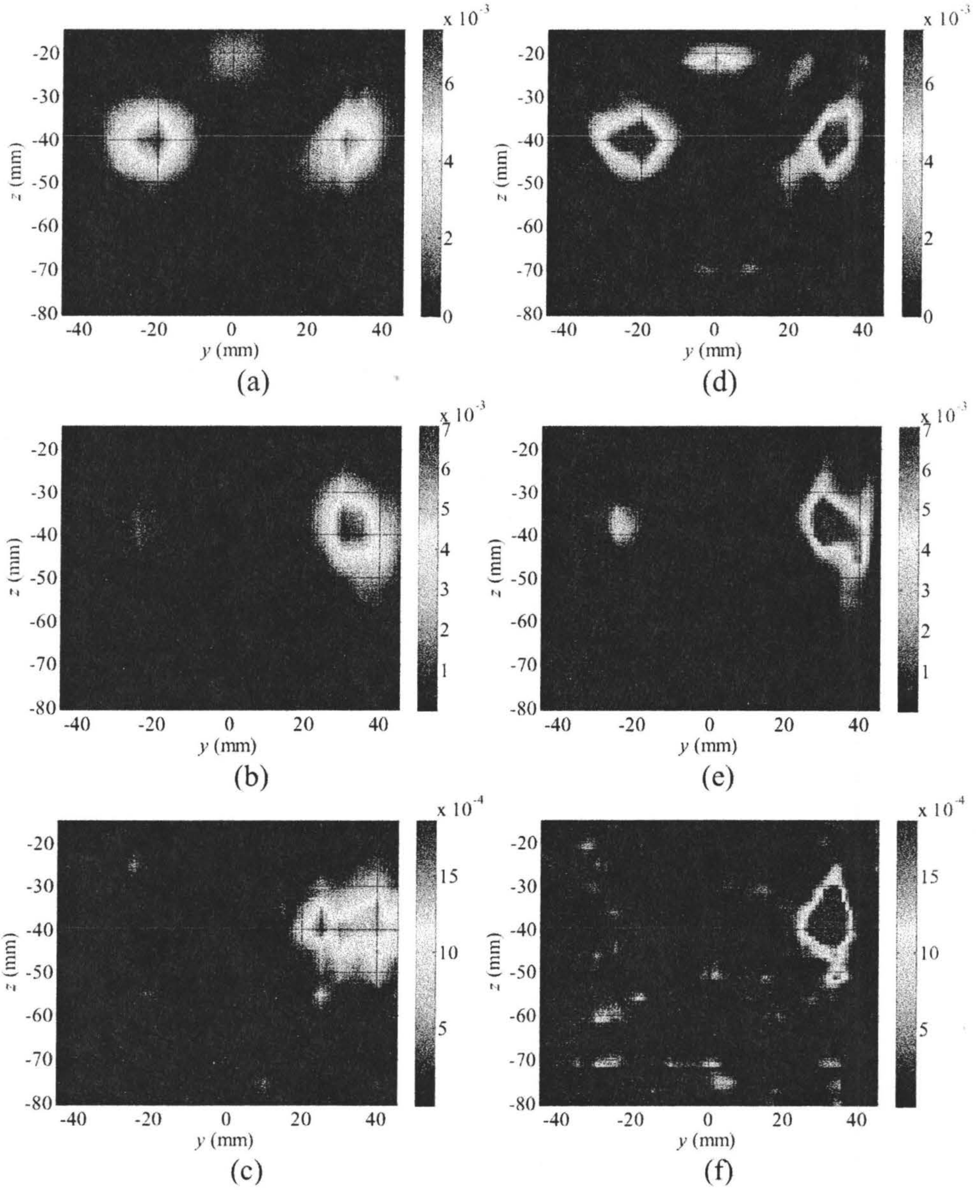

Fig. 3.7. The simulated $|S_{21}^{\text{cal}}|$ images from 2-D scanning of the heterogeneous breast model at: (a) 5 GHz, (b) 7 GHz, and (c) 9 GHz. The de-blurred images after applying blind de-convolution at: (d) 5 GHz, (e) 7 GHz, and (f) 9 GHz.

strength at the position of the tumor and the *S*-parameter mesh convergence error of the simulations. In all simulations, the mesh convergence error is set at 0.001. Table 3.3 shows the computed values for the so defined SNR for all three tumor simulants at 5 GHz, 7 GHz, and 9 GHz. It is observed that the SNR decreases drastically with increasing frequency. In particular, at 9 GHz, the SNR value is larger than 1 only for the tumor embedded in the fat. In measurements, the system SNR can be increased using low-noise amplifiers at the receiver.

The blind de-convolution algorithm is applied to the raw images in this example as well. Figs. 3.7(d)-(f) show the reconstructed images in which the tumors appear with better contrast.

TABLE 3.3
DEGRADATION OF SNR VERSUS FREQUENCY FOR THE THREE EMBEDDED TUMOR SIMULANTS IN FIG. 3.5

Tumor position (mm)	Host tissue	5 GHz	7 GHz	9 GHz
(0,-20)	fibro-glandular	2.2	0.2	0.03
(-23,-40)	trans-fat	6.3	0.9	0.2
(30,-40)	fat	7.4	7.1	1.9

3.6 SUMMARY

In this chapter, an aperture raster scanning setup was used to test the antenna proposed in chapter 2 in both measurements and simulations. The scanning setup clearly benefits from the excellent near-field directivity of the proposed antenna. Strong scatterers inside a homogeneous dielectric body were detected both in simulations and measurements. The detection of weak and strong scatterers in a heterogeneous breast model was also examined and the results are encouraging. A blind de-convolution technique was applied to improve the image quality. Overall, the simulation and experimental results confirm the capability of the planar raster scanning setup with the proposed antennas to provide high-quality images through near-field microwave measurements.

REFERENCES

[1] T. Rubæk, P. M. Meaney, P. Meincke, and K. D. Paulsen, "Nonlinear microwave imaging for breast-cancer screening using Gauss–Newton's method and the CGLS inversion algorithm," *IEEE Trans. Antennas and Propag.*, vol. 55, no. 8, pp. 2320–2331, Aug. 2007.

[2] S. K. Davis, B. D. Van Veen, S. C. Hagness, and F. Kelcz, "Breast tumor characterization based on ultrawide band microwave backscatter," *IEEE Trans. Biomed. Eng.*, vol. 55, no. 1, pp. 237–246, Jan. 2008.

[3] D. J. Kurrant and E. C. Fear, "An improved technique to predict the time-of-arrival of a tumor response in radar-based breast imaging," *IEEE Trans. Biomed. Eng.*, vol. 56, no. 4, pp. 1200–1208, Apr. 2009.

[4] A. Fhager and M. Persson, "Using *a priori* data to improve the reconstruction of small objects in microwave tomography," *IEEE Trans. Microwave Theory Tech.*, vol. 55, no. 11, pp. 2454–2462, Nov. 2007.

[5] C. Yu, M. Yuan, J. Stang, E. Bresslour, R. T. George, G. A. Ybarra, W. T. Joines, and Q. H. Liu, "Active microwave imaging II: 3-D system prototype and image reconstruction from experimental data," *IEEE Trans. Microwave Theory Tech.*, vol. 56, no. 4, pp. 991–1000, Apr. 2008.

[6] M. Klemm, I. J. Craddock, J. A. Leendertz, A. Preece, and R. Benjamin "Radar-based breast cancer detection using a hemispherical antenna array-experimental results" *IEEE Trans. Antennas and Propag.*, vol. 57, no. 6, pp. 1692–1704, Jun. 2009.

[7] D. A. Woten and M. El-Shenawee, "Broadband dual linear polarized antenna for statistical detection of breast cancer," *IEEE Trans. Antennas Propag.*, vol. 56, no. 11, pp. 3576–3580, Nov. 2008.

[8] J. Zhang, E. C. Fear, and R. Johnston, "Cross-Vivaldi antenna for breast tumor detection," *Microwave and Opt. Lett.*, vol. 51, no. 2, pp. 275–280, Feb. 2009.

[9] R. K. Amineh, M. Ravan, A. Trehan, and N. K. Nikolova, "Ultra-wide band TEM horn for microwave imaging based on aperture scanning," submitted to *IEEE Trans. Antennas and Propag.*

[10] R. K. Amineh, M. Ravan, A. Trehan, and N. K. Nikolova, "Microwave imaging for breast cancer diagnosis based on planar aperture scanning," *AP-*

S/URSI 2010, Canada.

[11] R. K. Amineh, A. Trehan, M. Ravan, and N. K. Nikolova, "Planar aperture scanning for microwave imaging of the breast: advances and challenges," *AP-S/URSI 2010*, Canada.

[12] R. K. Amineh, M. Ravan, A. Trehan, and N. K. Nikolova, "Near-field microwave imaging based on planar aperture scanning," *IMS 2010*, USA.

[13] D. Kundur and D. Hatzinakos, "Blind image de-convolution," *IEEE Signal Proc. Mag.*, May 1996.

[14] D. S. C. Biggs and M. Andrews, "Acceleration of iterative image restoration algorithms," *Applied Optics*, vol. 36, no. 8, pp. 1766–1775, Mar. 1997.

[15] Matlab$^{\text{TM}}$, Version 7.1, The MathWorks, Inc., 3 Apple Hill Drive, Natick, MA 01760–2098, 2005.

[16] M. Lazebnik, M. Okoniewski, J. H. Booske, and S. C. Hagness, "Highly accurate Debye models for normal and malignant breast tissue dielectric properties at microwave frequencies," *IEEE Microwave and Wirel. Components Lett.*, vol. 17, no. 12, Dec. 2007.

[17] T. Wuren, T. Takai, M. Fuiji, and I. Sakagami, "Effective 2-Debye-pole FDTD model of electromagnetic interaction between whole human body and UWB radiation," *IEEE Microwave Wirel. Components Lett.,* vol. 17, no. 7, pp. 483–485, Jul. 2007.

CHAPTER 4

MICROWAVE HOLOGRAPHY FOR NEAR-FIELD IMAGING

4.1 INTRODUCTION

Various methods have been proposed for microwave imaging. We described common optimization-based and radar-based techniques proposed so far for breast imaging in chapter 1. We also described the challenges in microwave imaging which have prevented so far the realization of reliable clinical imaging setups.

A microwave holographic imaging technique has been proposed in Pacific Northwest National Laboratory [1] which relies on the measurement of the magnitude and phase of the wave scattered from the imaged target on a rectangular aperture. Knowledge of the magnitude and phase across an aperture allows Fourier-transform (FT) based reconstruction of the target's reflectivity. This technique has been used to form high-resolution two-dimensional (2-D) or three-dimensional (3-D) images. In this method, a transmitter antenna and a receiver antenna move together on one side of the target to scan a rectangular planar aperture. The data collected at a single frequency can be used to reconstruct a 2-D reflectivity image of the target. Using wide-band frequency data allows for

3-D image reconstruction. The algorithm assumes that the wave emanating from the transmitter and the one reflected back from the target point are closely approximated by spherical waves. It then uses a 2-D FT to decompose them into an equivalent superposition of plane waves. Each of the plane wave components can then be phase shifted, or back propagated, to the target position. An inverse FT transforms the data back to the spatial domain. The magnitude of the complex image then yields an image of the target.

We should emphasize that the microwave holographic imaging discussed above has similarities and differences with the conventional microwave holography first presented in [2]. In [1], the scattered field due to the target is measured on an aperture similar to the conventional holography in which the interference pattern of a reference wave with the wave scattered from the target is recorded on a hologram. However, the reconstruction of the target in [1] is implemented based on the processing techniques in contrast to the conventional holography in which the hologram is illuminated with the reference wave to reconstruct a virtual target. Gathering all these applications in one category, so far, microwave holography has been proposed for concealed weapon detection [1][3]-[5], near-field analysis of antennas [6], biomedical imaging [7], and non-destructive testing and evaluation [8].

In this chapter, we extend the holographic image reconstruction developed in [1] to include not only back-scattered but also forward-scattered signals for 2-D and 3-D imaging. Our method does not make any assumptions about the incident field such as those based on plane wave representations. The incident field can be even given in a numerical form as in the case when it is derived through electromagnetic simulation or measurement. This is especially important in near-field imaging where the target is close to the antenna and the spherical assumption for the illuminating wave is not valid. This also makes the proposed techniques applicable to heterogeneous background mediums.

In the proposed techniques, the *S*-parameters at the terminals of the two antennas (one transmitting and one receiving) are measured when the antennas scan together two separate parallel apertures on both sides of a target. In the 2-D technique, the *S*-parameters collected at a single frequency are then processed to first localize the target in the range direction and then reconstruct a 2-D image of the target. In the 3-D technique, the *S*-parameters collected at several frequencies are processed to reconstruct a 3-D target region slice by slice.

The proposed 2-D and 3-D techniques are validated with predetermined targets in simulations. Resolution limits are derived and validated. The effect of noise is also studied. In addition, in the 3-D technique we investigate the effect of number of frequencies and target size and contrast on the reconstructed images. The outcome of this research work has been presented in [9]-[12].

4.2 THEORY OF 2-D MICROWAVE HOLOGRAPHY

The microwave holography set-up in this work consists of two x-polarized antennas and a 2D target in between as shown in Fig. 4.1. The radiation field of the x-polarized antennas can be reasonably approximated by TM$_x$ polarization. Thus, in this work we consider the x-components of the incident and scattered fields only. This leads to a simplified dyadic Green's function in which we only consider the G_x^x element. The transmitting and the receiving antennas perform 2-D scan while moving together on two separate planes (transmitter and receiver planes) positioned at $z = 0$ and $z = D$, respectively. The target is positioned at $z = \bar{z}$ and its thickness along the z-axis is assumed to be negligible. Assume we know the incident field (the field in the same region when the target is not present) at the $z = \bar{z}$ plane as a function of x and y when the transmitting antenna is at $x' = 0$, $y' = 0$ ($z' = 0$ at the transmitting plane):

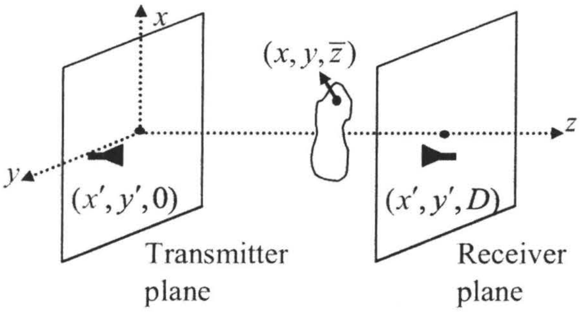

Fig. 4.1. Microwave holography setup.

$$s_0^{\text{inc}}(x, y, \bar{z}) \equiv s^{\text{inc}}(x, y, \bar{z}; 0, 0, 0) . \tag{4.1}$$

Here, the position $(x, y, \bar{z})$ indicates the observation point while $(0, 0, 0)$ indicates the origin of the wave. A method to find the true position of the target $\bar{z}$ is outlined later. Then, following the formulation of scattering problem presented in Appendix A, the scattered wave $s(x', y')$ due to the target when the transmitting and the receiving antennas are at $(x', y', 0)$ and (x', y', D), respectively, can be expressed as

$$\begin{aligned} s(x', y') &= \int_x \int_y f(x, y, \bar{z}) \cdot \frac{s_0^{\mathrm{inc}}(x - x', y - y', \bar{z}) e^{-ikr}}{r} dx dy \\ &= \int_x \int_y f(x, y, \bar{z}) \cdot \frac{s_0(x' - x, y' - y, \bar{z}) e^{-ikr}}{r} dx dy. \end{aligned} \tag{4.2}$$

where $f(x, y, \bar{z}) = (k_s(x, y) - k_0)$ and it is called the reflectivity function of the target, $s_0(x, y, \bar{z}) = s_0^{\mathrm{inc}}(-x, -y, \bar{z})$, G_x^x element has been approximated by e^{-ikr}/r where $r = \sqrt{(x' - x)^2 + (y' - y)^2 + (D - \bar{z})^2}$ and k is the wavenumber in the background medium.

We define the scattering function $g_0(x, y, \bar{z})$ as

$$g_0(x, y, \bar{z}) = \frac{s_0(x, y, \bar{z}) e^{-ikr}}{r}. \tag{4.3}$$

Next, $s(x', y')$ is expressed as a 2-D convolution integral

$$s(x', y') = \int_x \int_y f(x, y, \bar{z}) \cdot g_0(x' - x, y' - y, \bar{z}) dx dy. \tag{4.4}$$

This allows for the expression of the 2-D FT $S(k_x, k_y)$ of $s(x', y')$ as

$$S(k_x, k_y) = F(k_x, k_y, \bar{z}) G_0(k_x, k_y, \bar{z}) \tag{4.5}$$

where $F(k_x, k_y, \bar{z})$ and $G_0(k_x, k_y, \bar{z})$ are the 2-D FT of $f(x, y, \bar{z})$ and $g_0(x, y, \bar{z})$ with k_x and k_y being Fourier variables with respect to x and y, respectively. Finally, the reconstructed reflectivity function of the target is obtained as

$$f(x,y,\bar{z}) = \mathrm{F}_{2\mathrm{D}}^{-1}\left\{\frac{S(k_x,k_y)}{G_0(k_x,k_y,\bar{z})}\right\} \tag{4.6}$$

where $\mathrm{F}_{2\mathrm{D}}^{-1}$ denotes the inverse 2-D FT. The reconstructed image can then be obtained as the magnitude of the reflectivity function $|f(x,y,\bar{z})|$.

Note that (4.6) is a formal reconstruction formula and it can be seen as the "maximum likelihood solution" if the collected data suffer from incompleteness or any particular type of noise. The latter factors are often the cause for ill-posedness. However, as shown later, the technique is very robust to noise for the imaging applications considered here, which is mainly due to sufficient sampling (in the Nyquist sense) in the scanned apertures. Also, because of the finite size of the apertures, not all the wavenumbers (k_x,k_y) can be measured. As discussed later, this imposes lower and upper limits on k_x and k_y, which in turn limits the cross-range resolution of the images.

4.2.1 Image Reconstruction in 2-D Holography

In the imaging setup shown in Fig. 4.1, four *S*-parameters [13] can be measured for the two antennas at each scanning position. The *S*-parameter s_{jk} $(j,k = 1,2)$ is the scattered signal at the terminals of the j^{th} antenna when the k^{th} antenna transmits. The parameters s_{11} and s_{22} are referred to as the reflection *S*-parameters, while s_{21} and s_{12}, are referred to as the transmission *S*-parameters. The 2-D FT of s_{11}, s_{21}, s_{12}, and s_{22} are denoted as S_{11}, S_{21}, S_{12}, and S_{22}, respectively.

The collected data from each *S*-parameter can be processed using (4.6) to create an image of the target. In this case, we obtain four separate images with various resolutions (as discussed later). To reconstruct a single image, the data sets of all *S*-parameters must be used simultaneously. To implement this, we re-write (4.5) for each *S*-parameter at each (k_x,k_y), assuming that $F(k_x,k_y,\bar{z})$ is the same in all cases. This leads to

$$\begin{bmatrix} S_{11}(k_x,k_y) \\ S_{21}(k_x,k_y) \\ S_{12}(k_x,k_y) \\ S_{22}(k_x,k_y) \end{bmatrix} = F(k_x,k_y,\bar{z}) \begin{bmatrix} G_0^{11}(k_x,k_y,\bar{z}) \\ G_0^{21}(k_x,k_y,\bar{z}) \\ G_0^{12}(k_x,k_y,\bar{z}) \\ G_0^{22}(k_x,k_y,\bar{z}) \end{bmatrix}. \tag{4.7}$$

This system of equations is over-determined since at each (k_x,k_y), four equations need to be solved simultaneously to find only one unknown, $F(k_x,k_y,\bar{z})$. Thus, a least-square solution is employed at each spatial frequency pair (k_x,k_y) to find the corresponding value of $F(k_x,k_y,\bar{z})$. After $F(k_x,k_y,\bar{z})$ is obtained for all values of (k_x,k_y), $f(x,y,\bar{z})$ is computed as the inverse 2-D FT of $F(k_x,k_y,\bar{z})$.

4.2.2 Localization of the Target Along the Range in 2-D Holography

As discussed earlier, the true position of the target $\bar{z}$ along the range (the z axis) is a prerequisite for obtaining the scattering function $g_0(x,y,\bar{z})$ and consequently its 2-D FT $G_0(k_x,k_y,\bar{z})$, which is needed in the reconstruction formula (4.6). Therefore, a method is needed to determine $\bar{z}$. The method proposed here is based on the images created from the reflection *S*-parameters of the two antennas.

The 2-D FT of the reflectivity functions at an arbitrary selected position z reconstructed from reflection *S*-parameters using (4.5), $F^1(k_x,k_y,z)$ and $F^2(k_x,k_y,z)$, can be written as:

$$F^1(k_x,k_y,z)=\frac{S_{11}(k_x,k_y,\overline{z})}{G_0^1(k_x,k_y,z)} \tag{4.8}$$

$$F^2(k_x,k_y,z)=\frac{S_{22}(k_x,k_y,\overline{z})}{G_0^2(k_x,k_y,z)} \tag{4.9}$$

where $S_{11}(k_x,k_y,\overline{z})$ and $S_{22}(k_x,k_y,\overline{z})$ are the 2-D FT of reflection *S*-parameters s_{11} and s_{22}, respectively. Here, $z=\overline{z}$ emphasizes that the 2-D FT of measured reflection parameters are associated with the true position of the target $\overline{z}$. $G_0^1(k_x,k_y,z)$ and $G_0^2(k_x,k_y,z)$ are the FTs of the scattering functions for antenna 1 and antenna 2, respectively. They are computed based on the assumed target position z when the antennas are at the origin of their respective aperture planes (as described by (4.3)).

A cost function $J(z)$ is formulated as the 2-norm (Frobenius norm) of the difference between the 2-D FT of the two reconstructed reflectivity functions

$$J(z)=\left\|F^1(k_x,k_y,z)-F^2(k_x,k_y,z)\right\|. \tag{4.10}$$

We expect that the true position of the target would be the value of z for which $J(z)$ is minimized, i.e.,

$$\bar{z} = \arg\min_{z}(J(z)) . \tag{4.11}$$

In other words, the reflectivity functions obtained from the reflection coefficients of the two antennas are anticipated to be the same when the target position is estimated correctly.

To prove this assumption, we re-write $J(z)$ using (4.8) and (4.9)

$$J(z) = \left\| \frac{S_{11}(k_x,k_y,\bar{z})}{G_0^1(k_x,k_y,z)} - \frac{S_{22}(k_x,k_y,\bar{z})}{G_0^2(k_x,k_y,z)} \right\| . \tag{4.12}$$

If we assume that the true (unknown) position of the target is $z = \bar{z}$, $S_{11}(k_x,k_y,\bar{z})$ and $S_{22}(k_x,k_y,\bar{z})$ can be expanded as

$$S_{11}(k_x,k_y,\bar{z}) = F(k_x,k_y,\bar{z})G_0^1(k_x,k_y,\bar{z}) \tag{4.13}$$

$$S_{22}(k_x,k_y,\bar{z}) = F(k_x,k_y,\bar{z})G_0^2(k_x,k_y,\bar{z}) \tag{4.14}$$

where $F(k_x,k_y,\bar{z})$ is the true reflectivity function of the target, which is expected to be the same for both cases. Using (4.12), (4.13) and (4.14), $J(z)$ is written as

$$J(z) = \left\| F(k_x,k_y,\bar{z}) \left[\frac{G_0^1(k_x,k_y,\bar{z})}{G_0^1(k_x,k_y,z)} - \frac{G_0^2(k_x,k_y,\bar{z})}{G_0^2(k_x,k_y,z)} \right] \right\| . \tag{4.15}$$

Assuming spherical propagation for the incident wave ($s_0^{\text{inc}}(x,y,z) = e^{-ikr}$ where r is the distance between the origin of the wave and the observation point), the scattering functions for the two antennas are:

$$g_0^1(x,y,z) = \frac{e^{-i2kr_1}}{r_1} \tag{4.16}$$

$$g_0^2(x,y,z)=\frac{e^{-i2kr_2}}{r_2} \tag{4.17}$$

where $r_1=\sqrt{x^2+y^2+z^2}$ and $r_2=\sqrt{x^2+y^2+(D-z)^2}$. The 2-D FTs of (4.16) and (4.17) are [14]

$$G_0^1(k_x,k_y,z)=\frac{e^{-ik_z z}}{ik_z} \tag{4.18}$$

and

$$G_0^2(k_x,k_y,z)=\frac{e^{-ik_z(D-z)}}{ik_z} \tag{4.19}$$

where $k_z=\sqrt{4k^2-k_x^2-k_y^2}$. Using (4.18) and (4.19), the cost function in (4.15) is written as

$$J(z)=\left\|F(k_x,k_y,\bar{z})\left[e^{-ik_z(\bar{z}-z)}-e^{-ik_z(z-\bar{z})}\right]\right\|=\left\|2iF(k_x,k_y,\bar{z})\sin[k_z(z-\bar{z})]\right\|. \tag{4.20}$$

For the cost function of (4.20) to be minimized, the following must hold: $\sin[k_z(z-\bar{z})]=0$ or $k_z(z-\bar{z})=n\pi$ where $n\in\mathbb{Z}$. Therefore, $(z-\bar{z})=n\lambda_z/2$, where $\lambda_z=2\pi/k_z$ is the wavelength associated with k_z. Since k_z depends on k_x and k_y, λ_z also depends on k_x and k_y. This indicates that for each point (k_x,k_y) in the 2-D spatial-frequency domain, the minimum of the difference between $F^1(k_x,k_y,z)$ and $F^2(k_x,k_y,z)$ repeats every $\lambda_z/2$ when moving away from the true position of the target $\bar{z}$. Since $\lambda_z/2$ is not the same for different (k_x,k_y) points, the minimum of the difference between $F^1(k_x,k_y,z)$ and $F^2(k_x,k_y,z)$

occurs only at $n = 0$ or $z = \bar{z}$, where all (k_x, k_y) points give a common minimum.

The accuracy of the target localization along the range depends on the sampling rate in the range direction. As long as at least one of the sample planes falls inside the target volume, the described technique will identify the target's range location correctly by the minimum of the cost function. Note that in the proposed single-frequency 2-D reconstruction technique, the goal is not to build an image in depth but rather to identify planes, which contain the target. The 2-D reconstruction assumes that the target is thin, i.e. its dimension along the range is much smaller than its dimensions in the cross-range directions. The obvious restriction here is that for proper reconstruction, the target must lie in a plane more or less parallel to the apertures scanned by the antennas.

4.2.3 Cross-Range Resolution of the 2-D Holography

In order to investigate the cross-range resolution of the proposed holography imaging technique, similarly to the resolution estimation in [15], we reconstruct the image of a single point object described by the reflectivity function $f(x, y, \bar{z}) = \delta(x - x_0, y - y_0)$ where δ is the Dirac delta function. The FT of this object is

$$F(k_x, k_y, \bar{z}) = \int_x \int_y \delta(x - x_0, y - y_0) \cdot e^{-ik_x x - ik_y y} dx dy = e^{-ik_x x_0 - ik_y y_0} . \qquad (4.21)$$

According to (4.5), the FT of the signal due to this object is

$$S(k_x, k_y, \bar{z}) = e^{-ik_x x_0 - ik_y y_0} G_0(k_x, k_y, \bar{z}) . \qquad (4.22)$$

Using (4.6) and (4.22), the reconstructed image is obtained as

$$\tilde{f}(x,y,\bar{z}) = \mathrm{F}_{2\mathrm{D}}^{-1}\left\{\frac{e^{ik_x x_0}\, e^{ik_y y_0} G_0(k_x,k_y,\bar{z})}{G_0(k_x,k_y,\bar{z})}\right\} = \mathrm{F}_{2\mathrm{D}}^{-1}\; e^{-ik_x x_0 - ik_y y_0} \quad . \tag{4.23}$$

Assuming that the wavenumbers in the x and y directions are bounded as $k_x \in [-k_x^{\mathrm{m}}, k_x^{\mathrm{m}}]$ and $k_y \in [-k_y^{\mathrm{m}}, k_y^{\mathrm{m}}]$ (for apertures symmetrical with respect to the origin), the reconstructed image is computed as

$$\tilde{f}(x,y,\bar{z}) = \int_{-k_y^{\mathrm{m}}}^{k_y^{\mathrm{m}}} \int_{-k_x^{\mathrm{m}}}^{k_x^{\mathrm{m}}} e^{ik_x(x-x_0)} e^{ik_y(y-y_0)} dk_x dk_y = k_x^{\mathrm{m}} k_y^{\mathrm{m}} \mathrm{sinc}[k_x^{\mathrm{m}}(x-x_0)] \mathrm{sinc}[k_y^{\mathrm{m}}(y-y_0)] \,. \tag{4.24}$$

The first zeros of the *sinc* functions occur at $\delta_x = x - x_0 = \pi / k_x^{\mathrm{m}}$ and $\delta_y = y - y_0 = \pi / k_y^{\mathrm{m}}$. Here, δ_x and δ_y define the cross-range resolution of the technique. Two point reflectors have to be separated by more than δ_x and δ_y in the x and y directions, respectively, so that they can be distinguished.

The limits for the wavenumbers k_x^{m} and k_y^{m} are determined based on both illumination and reflection paths. Consider the bounds for k_x. If the angles subtended by the transmitting and receiving apertures (or the full beamwidths of the antennas, whichever is less) are denoted by θ_t and θ_r, respectively, the maximum phase shift occurs for a wave traveling from the edge of the transmitting aperture to the edge of the receiving aperture as shown in Fig. 4.2. This phase shift equals $k\sin(\theta_t / 2)x + k\sin(\theta_r / 2)x$. Therefore, $k_x^{m} = k\sin(\theta_t / 2)$ $+ k\sin(\theta_r / 2)$ and the cross-range resolution is

$$\delta_x = \frac{\pi}{k_x^{\mathrm{m}}} = \frac{\pi}{k\sin(\theta_t/2) + k\sin(\theta_r/2)} = \frac{\lambda}{2[\sin(\theta_t/2) + \sin(\theta_r/2)]}. \qquad (4.25)$$

Note that in the case of reflection, where the illuminated and reflected waves travel the same path, we have $\theta_t = \theta_r = \theta_b$, and the bound for k_x is $k_x^m = 2k\sin(\theta_b/2)$. This corresponds to resolution of $\delta_x = \lambda[4\sin(\theta_b/2)]^{-1}$, which is the same as the resolution estimated in [1]. Another interesting observation is that the resolution would be the same when using either of the transmission coefficients (s_{12} or s_{21} parameters) to reconstruct the image. The discussion for the resolution in the y direction is similar.

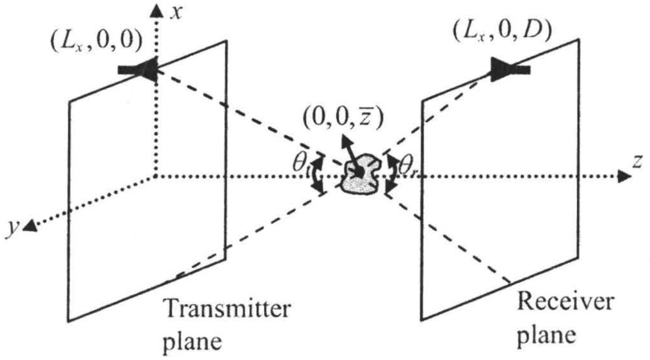

Fig. 4.2. Illustration of angles subtended by the aperture to be used in the resolution estimation in the x direction.

4.2.4 Spatial and Frequency Sampling in 2-D Holography

In order to make use of all frequency components of the measured signals, the sampling rate of the scan has to satisfy the Nyquist criterion, i.e., the phase shift from one sample point to the next must be less than π. For a spatial sampling interval of Δx, the worst case is a phase shift of no more than $2k\Delta x$. Therefore, the sampling criterion can be expressed as [1]

$$\Delta x < \lambda / 4 . \tag{4.26}$$

4.2.5 Reconstruction Results for 2-D Holography

To evaluate the proposed microwave holography technique, two $\lambda/2$ horizontally-polarized dipole antennas with a target in between are simulated in FEKO Suite 5.4 [15] (e.g., see Fig. 4.3). The antennas perform a 2-D scan by moving together on aperture planes. The aperture planes are located at $z = 50$ mm and $z = 0$. We refer to them as aperture 1 and aperture 2 corresponding to antenna 1 and antenna 2, respectively. The apertures have a size of 60 mm$\times$60 mm with their centers being on the z axis.

The S-parameters s_{ij}^{t} $(i, j = 1, 2)$ for the two antennas are calculated and recorded for every (x', y') position as the antennas perform the 2-D scan together on aperture 1 and aperture 2. The numerical noise is estimated through the numerical convergence error which is 0.02 for the magnitude of the S-parameters. The same setup is simulated without the target to obtain the background scattering parameters s_{ij}^{b}. Then, the calibrated S-parameters at each (x', y') position are calculated as

$$s_{ij}^{\mathrm{cal}}(x', y') = s_{ij}^{\mathrm{t}}(x', y') - s_{ij}^{\mathrm{b}} . \tag{4.27}$$

These calibrated S-parameters are then used in the holographic reconstructions. Here, due to the uniform background, the background simualtions need to be performed only once in a sample (x', y') position since in all other positions they are the same.

Since the dipoles are horizontally polarized along the x axis, the x component of the simulated incident electric field E_x^{inc} is recorded at the imaged planes. These planes are of size $120\ \text{mm} \times 120\ \text{mm}$. The recorded E_x^{inc} is considered as $s_0^{\text{inc}}(x, y, \bar{z})$. Also, since the frequency in the simulations is 35 GHz, from (4.26), Δx has to be smaller than 2.14 mm. A sampling rate of 1 mm along both x and y is adopted.

4.2.5.1 Reconstruction of "X" Shape Dielectric Target in Free Space

As a first example, an "X" shape target parallel to the x-y plane is simulated as shown in Fig. 4.3. Each arm of the "X" object is 16 mm long with a square cross-section with a side of 2 mm. The center of the target is located at $\bar{z} = 15$ mm. The target has a relative permittivity of $\varepsilon_r = 5$ and conductivity of $\sigma = 0$ S/m. It is located in free space. First, in order to find the range location of the target, we apply the reconstruction formula (4.6) for assumed target positions z, where z changes from 1 mm to 49 mm with a step of 1 mm. The cost function (4.10) is then calculated at each z. Fig. 4.4 shows the cost function $J(z)$ versus the assumed target position along the z-axis. It is evident that the minimum of the cost function is at the true position of the target ($z = 15$ mm). This validates the target's range localization method presented in section 4.2.2.

Knowing the location of the target, we can reconstruct the 2-D shape of the target using the proposed holography method. Figs. 4.5 to 4.8 show the 2-D colour map images of the calibrated *S*-parameters magnitudes and the respective reconstructed images of the target. For instance, Fig. 4.5(a) shows the 2-D colour map of $|s_{11}^{\mathrm{cal}}|$ where the backscattered signal is recorded by the first dipole antenna operating as both a transmitter and a receiver. Fig. 4.5(b) shows the related reconstructed image of the target. All reconstructed images reproduce the shape of the target accurately. In contrast, the 2-D colour maps of the *S*-parameters magnitudes do not provide any clue about the shape of the target. It is worth noting that since the object is dielectric, the transmission *S*-parameters (s_{21} and s_{12}) are stronger than the reflection *S*-parameters (s_{11} and s_{22}) and this leads to reconstruction of images with better quality.

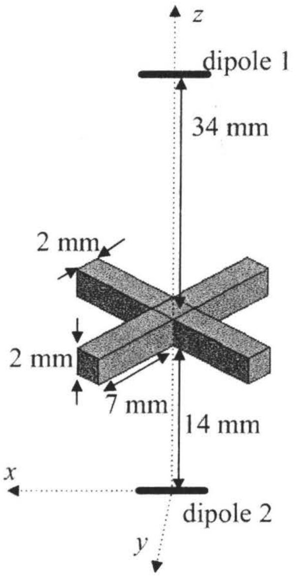

Fig. 4.3. The X-shape object scanned by two horizontally-polarized dipoles at 35 GHz.

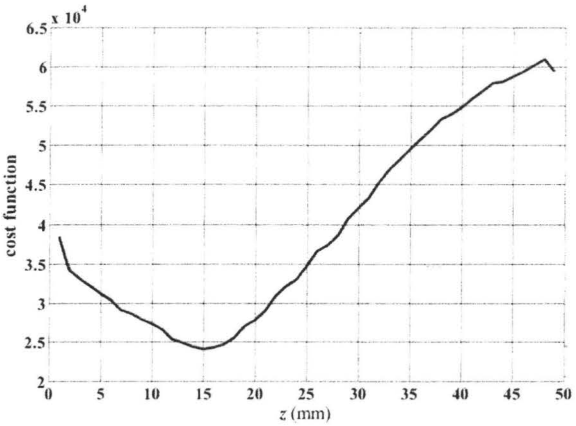

Fig. 4.4. Computed cost function versus target range location along the z-axis (the true target position is at $\bar{z} = 15$ mm).

4.2.5.2 Reconstruction of "X" Shape Lossy Dielectric Target in Lossy Medium

As a second example, the same setup as the one shown in Fig. 4.3 is simulated with a dielectric target with $\varepsilon_r = 5$ and $\sigma = 2$ S/m. It is located in a lossy background medium with $\varepsilon_r = 1$ and $\sigma = 0.4$ S/m. Figs. 4.9 to 4.12 show the images based on the calibrated S-parameters magnitudes as well as the reconstructed images after applying the holography algorithm. It is evident that the reconstruction algorithm works well in a lossy background medium. This could be of interest in microwave imaging for medical diagnostics. We note that the reconstructed image from the s_{11} parameter is blurrier compared to the rest of the images. This arises from the fact that the signal transmitted and received by antenna 1 travels the longest distance in the lossy medium compared to the rest of the cases. This leads to more attenuation and weaker signals and, therefore, less accurate results.

4.2.5.3 Reconstruction of "X" Shape Conductor Target in Free Space

As a third example, for the sake of comparison with the previous examples, the same setup shown in Fig. 4.3 is simulated with a perfectly conductive target in free space. Figs. 4.13 to 4.16 show the reconstructed images after applying the holography algorithm. It is observed that the images obtained from the reflection *S*-parameters (s_{11} and s_{22}) have slightly better quality. We believe that this is due to the fact that reflection *S*-parameters for the conductor are stronger than the transmission *S*-parameters (s_{21} and s_{12}). It is observed that the holography reconstruction operates well with conducting targets, too. This could be of interest in applications such as concealed weapon detection.

4.2.5.4 Single Reconstruction of "X" Shape Targets From Four S-Parameters

We have also generated single images from all data sets provided from the four *S*-parameters for the above examples. Fig. 4.17 show the reconstructed images obtained using (4.7) to produce images for the examples discussed above. We observe that the quality of the images when using all four *S*-parameters is comparable with the images created from the individual *S*-parameters.

4.2.5.5 The Effect of Random Noise on Target Reconstructions

In order to investigate the effect of random noise on the reconstruction technique, we consider two types of noises: 1) adding white Gaussian noise to the

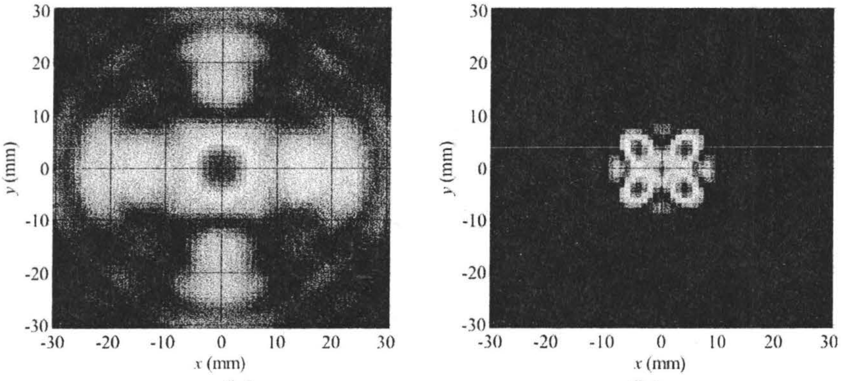

(a) (b)

Fig. 4.5. (a) Simulated $|s_{11}^{\text{cal}}|$ and (b) the reconstructed image for the dielectric target in Fig. 4.3 with $\varepsilon_r = 5$ and $\sigma = 0$ S/m in free space.

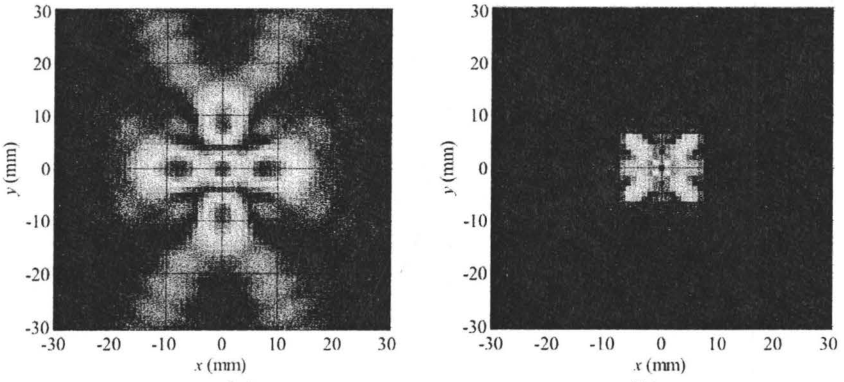

(a) (b)

Fig. 4.6. (a) Simulated $|s_{22}^{\text{cal}}|$ and (b) the reconstructed image for the dielectric target in Fig. 4.3 with $\varepsilon_r = 5$ and $\sigma = 0$ S/m in free space.

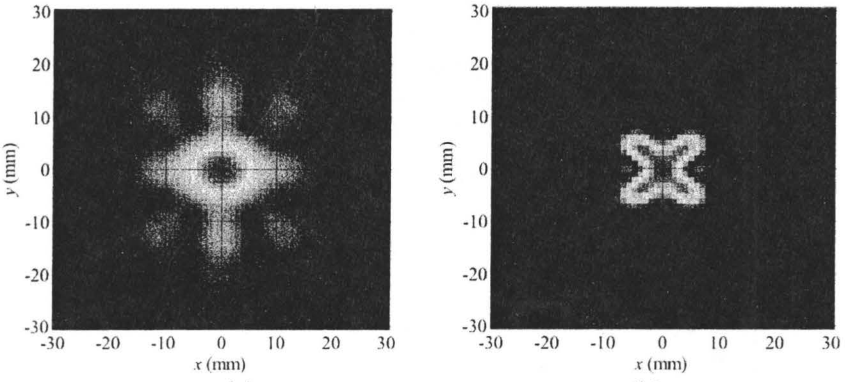

(a) (b)

Fig. 4.7. (a) Simulated $|s_{21}^{\text{cal}}|$ and (b) the reconstructed image for the dielectric target in Fig. 4.3 with $\varepsilon_r = 5$ and $\sigma = 0$ S/m in free space.

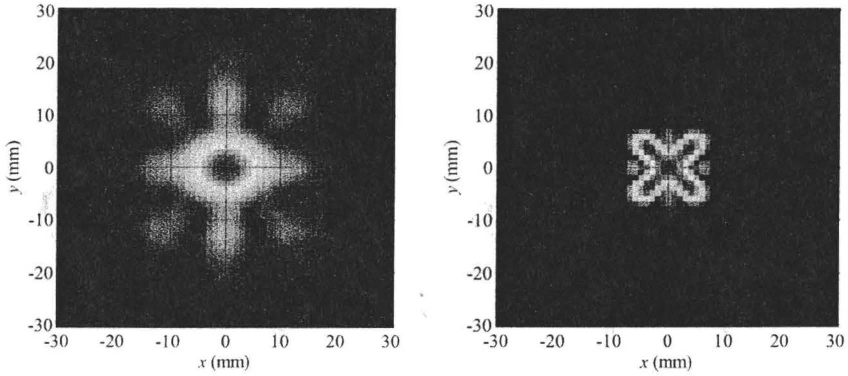

(a) (b)

Fig. 4.8. (a) Simulated $|s_{12}^{\text{cal}}|$ and (b) the reconstructed image for the dielectric target in Fig. 4.3 with $\varepsilon_r = 5$ and $\sigma = 0$ S/m in free space.

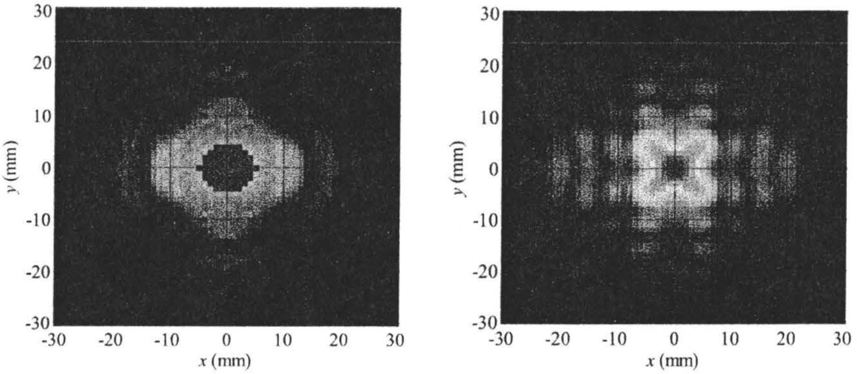

(a) (b)

Fig. 4.9. (a) Simulated $|s_{11}^{\text{cal}}|$ and (b) reconstructed image for the target in Fig. 4.3 with $\varepsilon_r = 5$ and $\sigma = 2$ S/m in a lossy medium with $\varepsilon_r = 1$ and $\sigma = 0.4$ S/m.

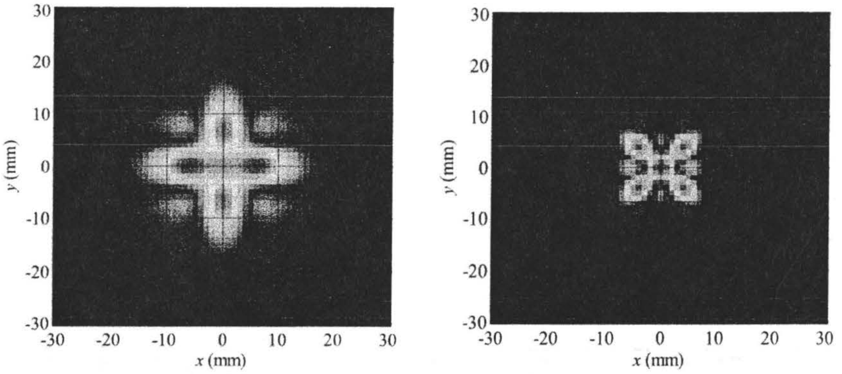

(a) (b)

Fig. 4.10. (a) Simulated $|s_{22}^{\text{cal}}|$ and (b) reconstructed image for the target in Fig. 4.3 with $\varepsilon_r = 5$ and $\sigma = 2$ S/m in a lossy medium with $\varepsilon_r = 1$ and $\sigma = 0.4$ S/m.

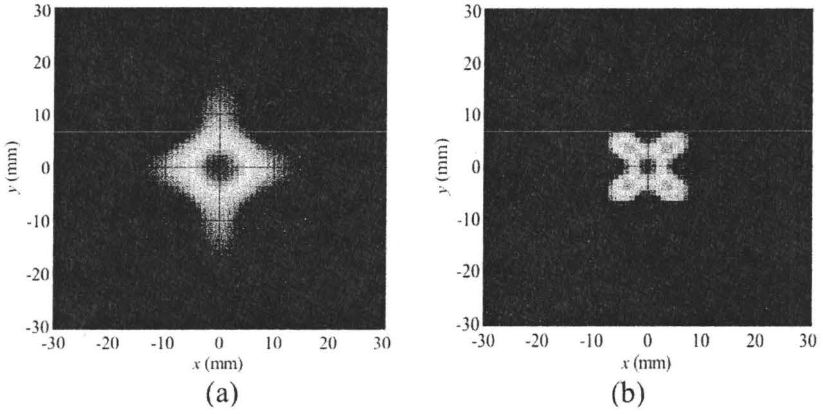

(a) (b)

Fig. 4.11. (a) Simulated $|s_{21}^{\text{cal}}|$ and (b) reconstructed image for the target in Fig. 4.3 with $\varepsilon_r = 5$ and $\sigma = 2$ S/m in a lossy medium with $\varepsilon_r = 1$ and $\sigma = 0.4$ S/m.

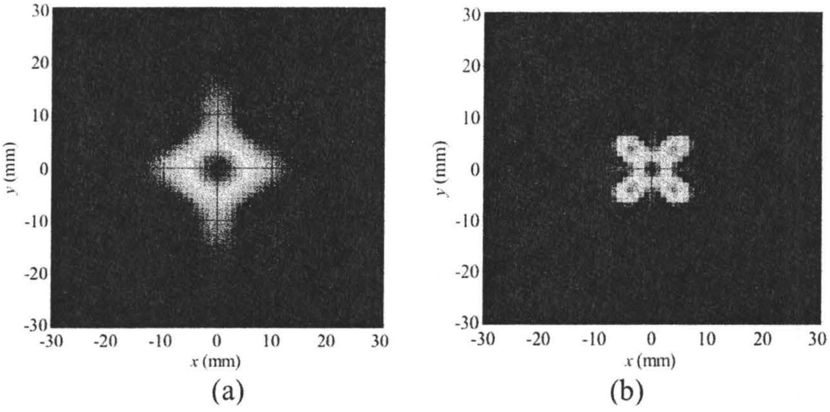

(a) (b)

Fig. 4.12. (a) Simulated $|s_{12}^{\text{cal}}|$ and (b) reconstructed image for the target in Fig. 4.3 with $\varepsilon_r = 5$ and $\sigma = 2$ S/m in a lossy medium with $\varepsilon_r = 1$ and $\sigma = 0.4$ S/m.

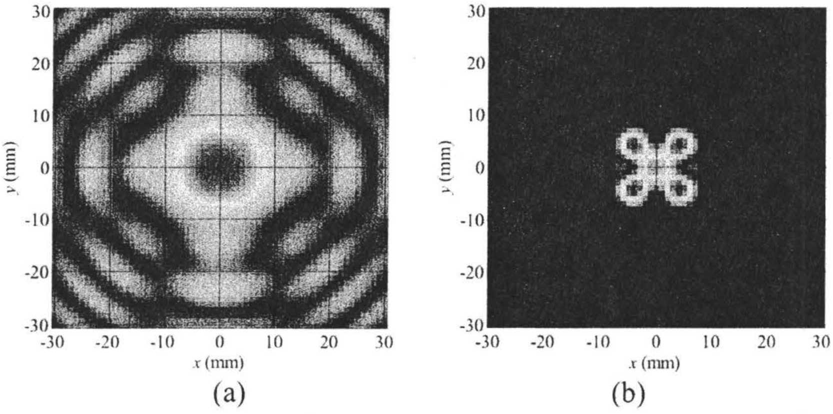

(a) (b)

Fig. 4.13. (a) Simulated $|s_{11}^{\text{cal}}|$ and (b) reconstructed image for a perfectly conducting target in Fig. 4.3 in free space.

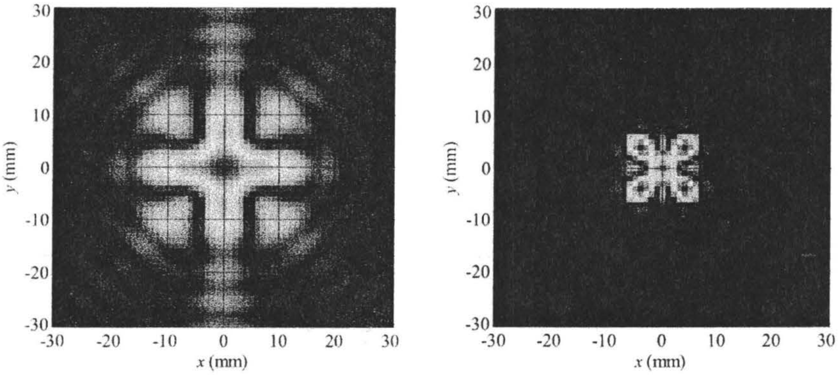

(a) (b)

Fig. 4.14. (a) Simulated $|s_{22}^{\text{cal}}|$ and (b) reconstructed image for a perfectly conducting target in Fig. 4.3 in free space.

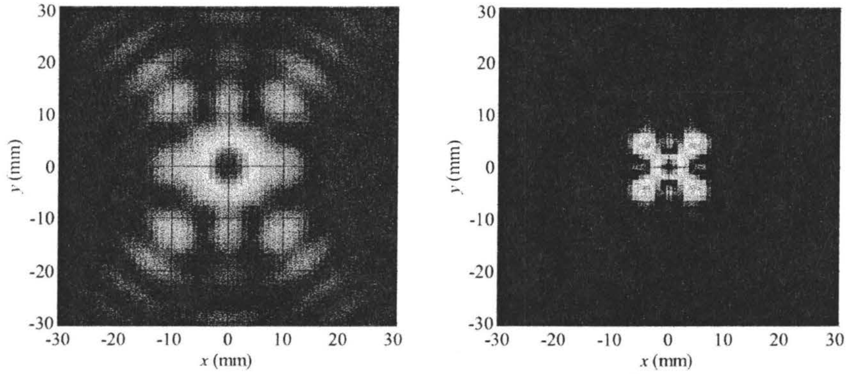

(a) (b)

Fig. 4.15. (a) Simulated $|s_{21}^{\text{cal}}|$ and (b) reconstructed image for a perfectly conducting target in Fig. 4.3 in free space.

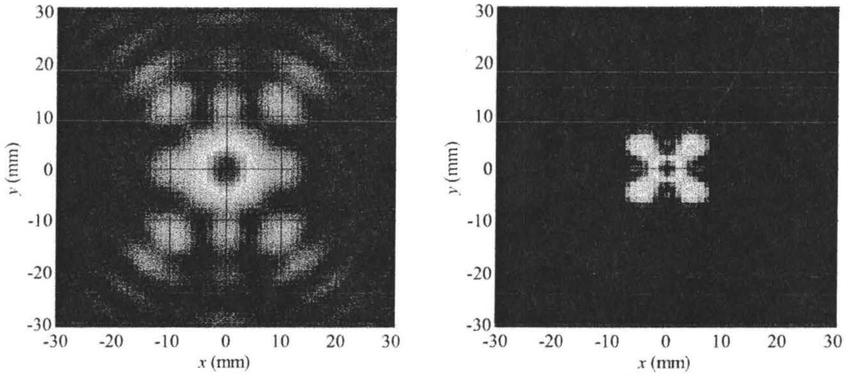

(a) (b)

Fig. 4.16. (a) Simulated $|s_{12}^{\text{cal}}|$ and (b) reconstructed image for a perfectly conducting target in Fig. 4.3 in free space.

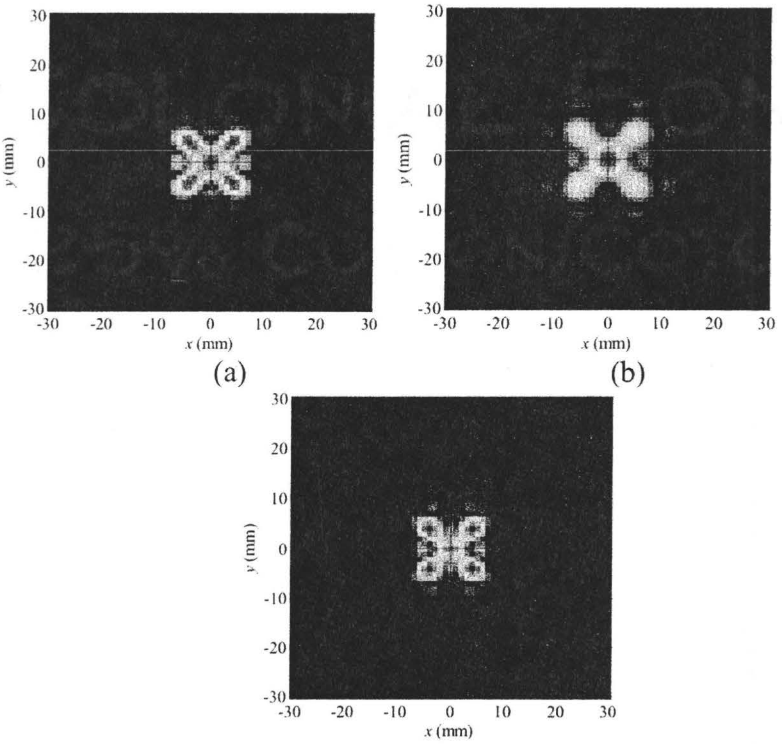

(a) (b) (c)

Fig. 4.17. Reconstructed images obtained from the least-square solution of the system of equations in (4.7) for the example of: (a) section 4.2.5.1, (b) section 4.2.5.2, and (c) section 4.2.5.3.

complex values of the *S*-parameters assuming that this type of noise is produced by the electronic devices or the environment, 2) adding white Gaussian noise only to the phase of the *S*-parameters assuming possible mechanical variations of the antennas during the 2-D scan which would affect the phase more seriously than the magnitude of the *S*-parameters. For both types, we apply high levels of noise. For the first case we apply signal-to-noise ratios (SNR) of 0 dB, -10 dB, and -20 dB while for the second type of noise we apply SNR values of 20 dB, 10 dB, and 0 dB. Furthermore, for the first type of noise we add noise to both the *S*-parameters and the scattering functions.

Figs. 4.18, 4.19, and 4.20 show the reconstructed images obtained from noisy data for the examples in sections 4.2.5.1, 4.2.5.2, and 4.2.5.3, respectively, when solving (4.7) to produce a single image. As observed in these images, for an SNR value as low as 0 dB for the first type of noise and 20 dB for the second type, the quality of the reconstructed images is still comparable with the images obtained from noiseless data shown in Figs. 4.17(a), (b), and (c). Similar conclusion is derived when reconstructing images from individual *S*-parameters. This indicates that the proposed reconstruction technique is very robust to noise. To illustrate the amount of distortion due to 0 dB type 1 noise, Fig. 4.21 shows the distribution of $|s_{11}^{\text{cal}}|$ and $|s_{22}^{\text{cal}}|$ of Figs. 4.5 and 4.6 after adding noise. It is with this distorted data that the image in Fig. 4.18(a) was obtained.

To further study the effect of noise on the reconstructed images, in Fig. 4.22, we plot the distribution of the modulus of the 2-D FT of the noiseless and the noisy s_{11} (with SNR = 0 dB) for the case presented in Fig. 4.5. As Fig. 4.22(a) shows, the highest values of 2-D FT are at lower spatial frequencies close to the origin. Fig. 4.22(b) shows that the Gaussian noise affects mostly the higher spatial frequencies that have much lower amplitudes. Thus, although the SNR is as low as 0 dB, the reconstructed images still are of good quality. For SNR values lower than 0 dB, we observe that the images deteriorate [refer to Figs. 4.18 to 4.20].

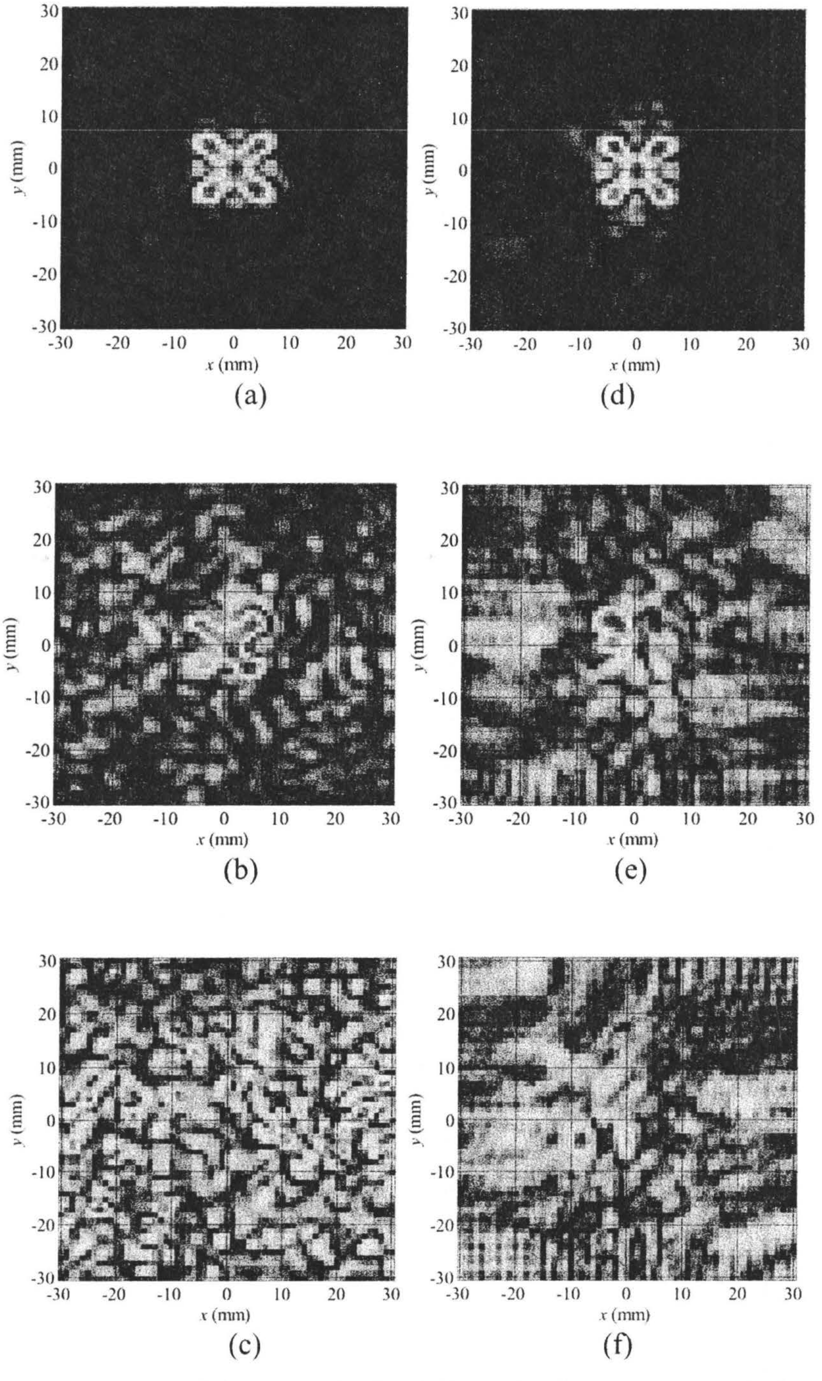

(a) (d)

(b) (e)

(c) (f)

Fig. 4.18. Reconstructed images obtained from the least-square solution of the system of equations in (4.7) for the example of section 4.2.5.1 when adding noise to the complex *S*-parameters with: (a) SNR = 0 dB, (b) SNR = -10 dB, and (c) SNR = -20 dB; and when adding noise only to the phase of the *S*-parameters with: (d) SNR = 20 dB, (e) SNR = 10 dB, and (f) SNR = 0 dB.

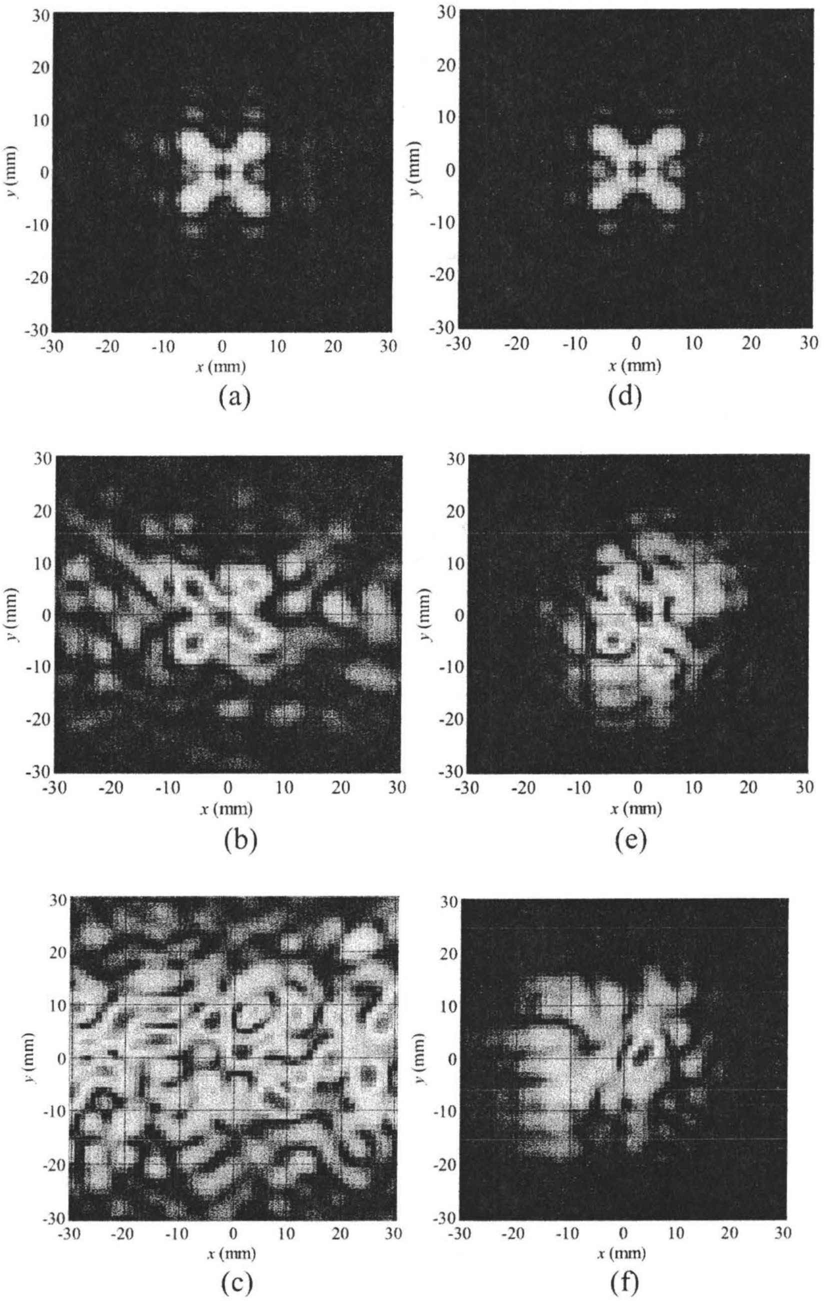

Fig. 4.19. Reconstructed images obtained from the least-square solution of the system of equations in (4.7) for the example of section 4.2.5.2 when adding noise to the complex *S*-parameters with: (a) SNR = 0 dB, (b) SNR = -10 dB, and (c) SNR = -20 dB; and when adding noise only to the phase of the *S*-parameters with: (d) SNR = 20 dB, (e) SNR = 10 dB, and (f) SNR = 0 dB.

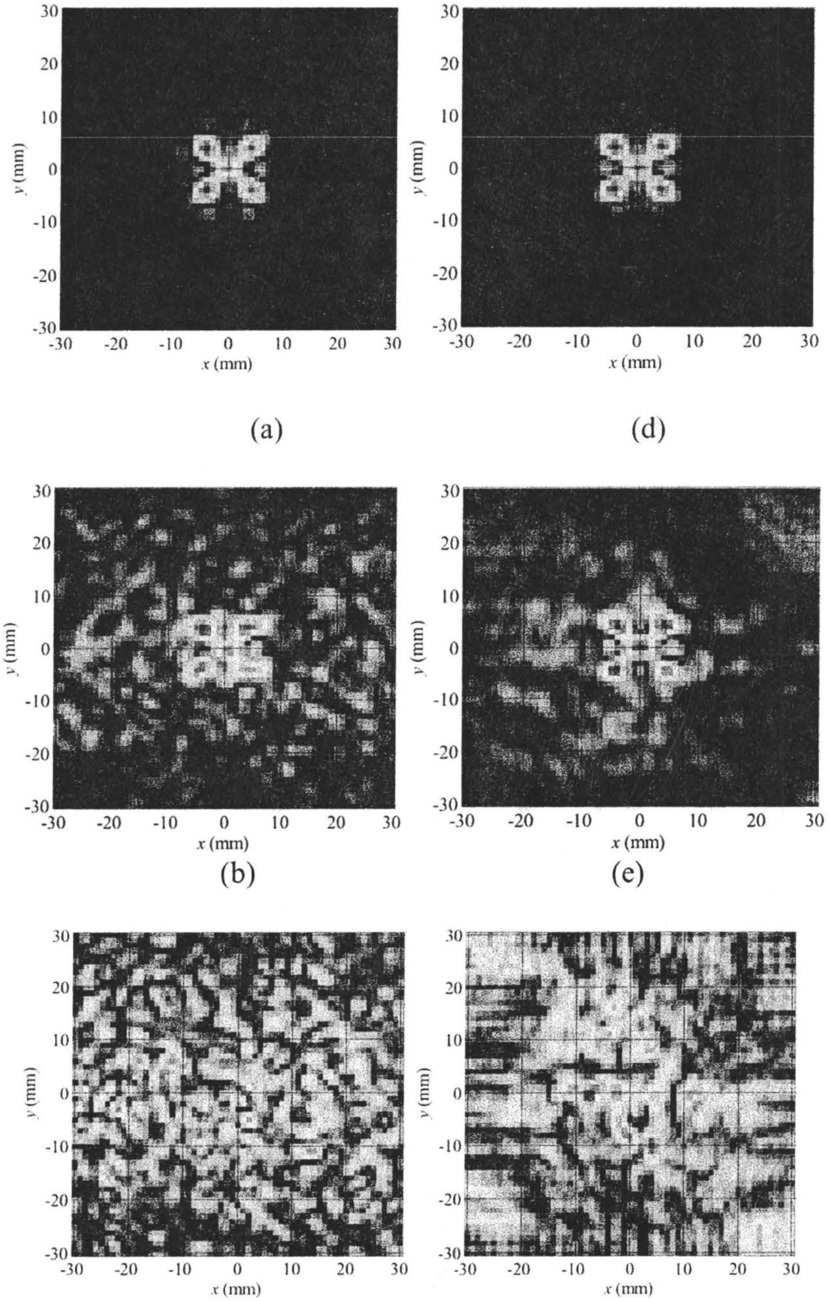

(a) (d)

(b) (e)

(c) (f)

Fig. 4.20. Reconstructed images obtained from the least-square solution of the system of equations in (4.7) for the example of section 4.2.5.3 when adding noise to the complex S-parameters with: (a) SNR = 0 dB, (b) SNR = -10 dB, and (c) SNR = -20 dB; and when adding noise only to the phase of the S-parameters with: (d) SNR = 20 dB, (e) SNR = 10 dB, and (f) SNR = 0 dB.

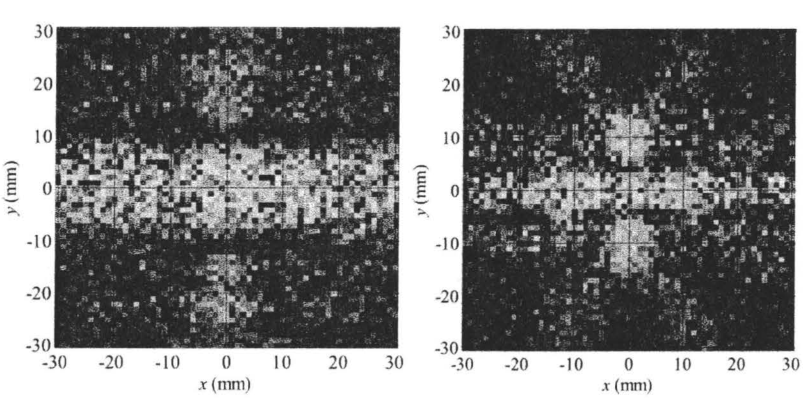

(a) (b)

Fig. 4.21. Distribution of the modulus of the reflection *S*-parameters after adding white Gaussian noise of type 1 with SNR = 0 dB for: (a) $|s_{11}^{\mathrm{cal}}|$ in Fig. 4.5 and (b) $|s_{22}^{\mathrm{cal}}|$ in Fig. 4.6.

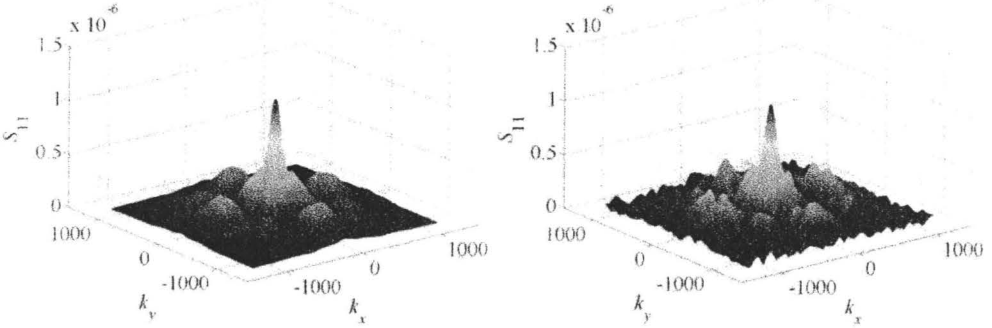

(a) (b)

Fig. 4.22. Distribution of the modulus of the 2-D FT of s_{11}^{cal}, $|S_{11}^{\mathrm{cal}}|$, for the case presented in Fig. 4.5: (a) noiseless, (b) after adding white Gaussian noise with SNR = 0 dB.

4.2.5.6 Resolution Study

In order to investigate the resolution of the proposed method with respect to frequency, we simulate the setup shown in Fig. 4.23 in which the targets are two conductor cuboids with a side of 2 mm. Their edges are $d = 3$ mm apart. These cuboids are at $\bar{z} = 25$ mm between the two $\lambda/2$ horizontally-polarized

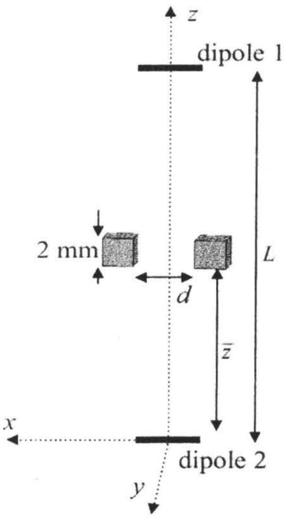

Fig. 4.23. Two conductor cuboids with a side of 2 mm and distance from edge to edge of *d* scanned by two horizontally-polarized dipoles.

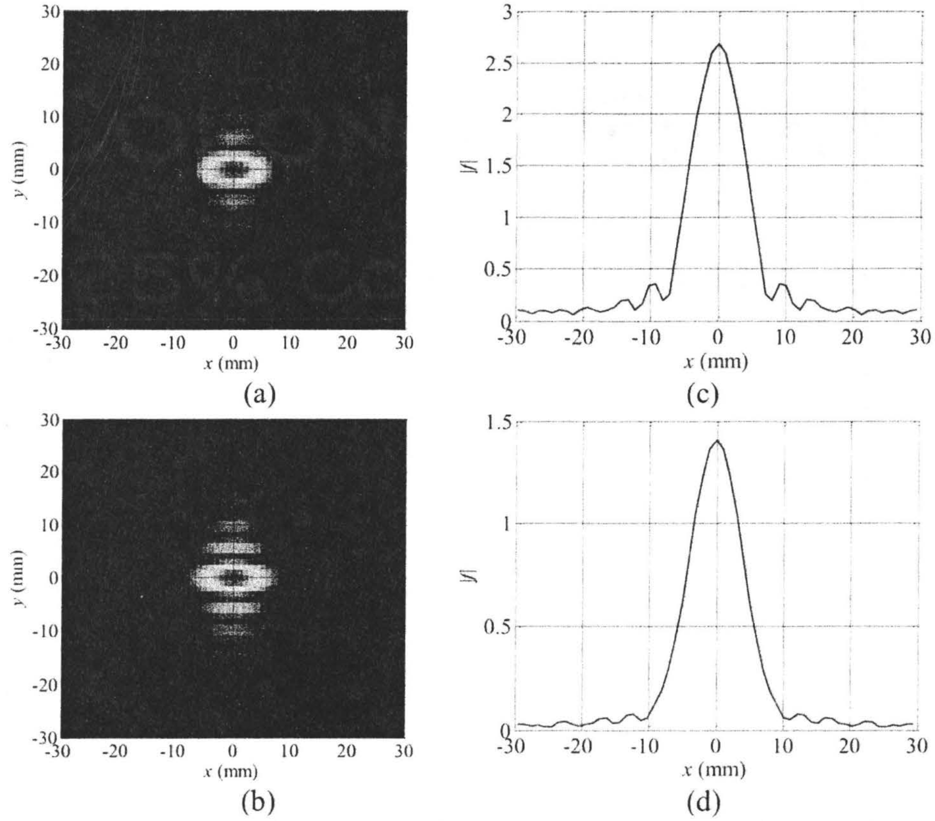

Fig. 4.24. Reconstructed images for the setup shown in Fig. 4.23 at 25 GHz. 2-D image obtained from: (a) s_{11}^{cal} and (b) s_{12}^{cal}. The cut-through plot at $y = 0$ for the image obtained from: (c) s_{11}^{cal} and (d) s_{12}^{cal}.

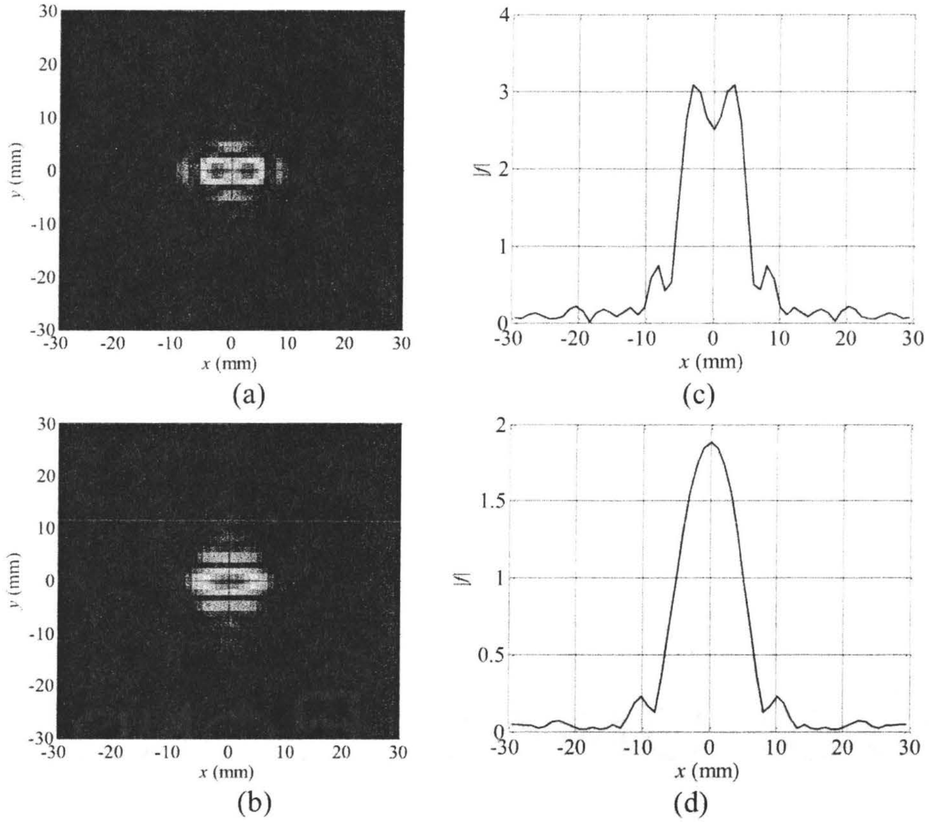

Fig. 4.25. Images reconstructed using the holography algorithm for the setup shown in Fig. 4.23 at 30 GHz. 2-D image obtained from: (a) s_{11}^{cal} and (b) s_{12}^{cal}. The cut-through plot at $y = 0$ for the image obtained from: (c) s_{11}^{cal} and (d) s_{12}^{cal}.

dipole antennas which are $L = 50$ mm apart. The scanning data are collected at three frequencies: 25 GHz, 30 GHz, and 35 GHz. Since the targets are in the midway between the two antennas, we expect $s_{11} \approx s_{22} \approx s_{12} \approx s_{21}$. Using (4.25), the theoretical cross-range resolution for both reflection S-parameters and transmission S-parameters at these three frequencies are 3.90 mm, 3.25 mm, and 2.79 mm, respectively. Figs. 4.24 to 4.26 show the reconstructed images as well as the cut-through plots at $y = 0$ when we use the calibrated complex S-parameters at the three different frequencies. As Fig. 4.24 shows, at 25 GHz,

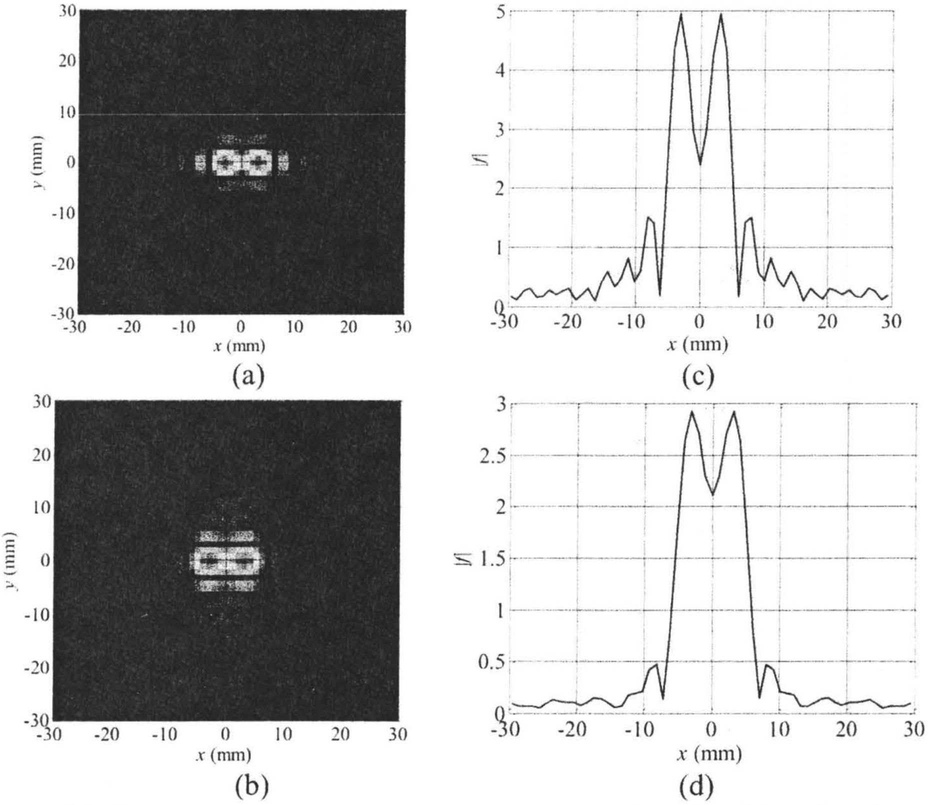

(a) (c)

(b) (d)

Fig. 4.26. Images reconstructed using the holography algorithm for the setup shown in Fig. 4.23 at 35 GHz. 2-D image obtained from: (a) s_{11}^{cal} and (b) s_{12}^{cal}. The cut-through plot at $y = 0$ for the image obtained from: (c) s_{11}^{cal} and (d) s_{12}^{cal}.

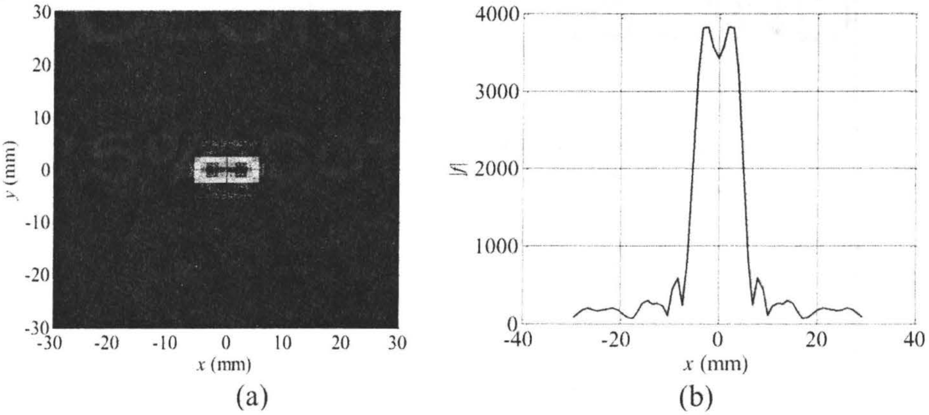

(a) (b)

Fig. 4.27. (a) Reconstructed image for the setup shown in Fig. 4.23 from the complex reflection coefficients (s_{11}^{cal} or s_{22}^{cal}) at 35 GHz using the method in [1], and (b) its cut-through plot at $y = 0$.

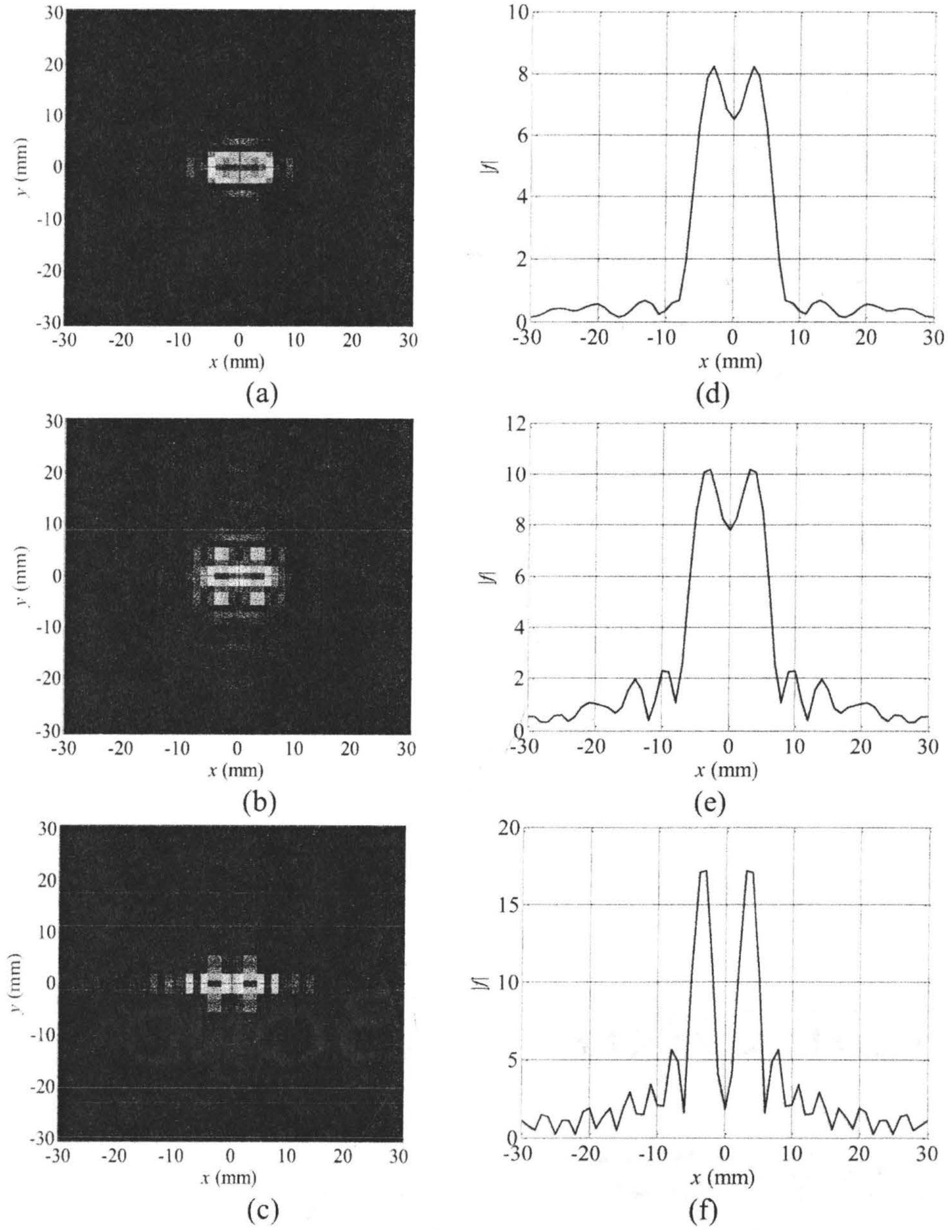

(a) (d)
(b) (e)
(c) (f)

Fig. 4.28. Images reconstructed using the holography algorithm for the setup shown in Fig. 4.23 from the complex scattering coefficients at 35 GHz. 2-D image obtained from: (a) s_{11}^{cal}, (b) $s_{12}^{\mathrm{cal}} = s_{21}^{\mathrm{cal}}$, and (c) s_{22}^{cal}. The cut-through image at $y = 0$ for the image obtained from: (d) s_{11}^{cal}, (e) $s_{12}^{\mathrm{cal}} = s_{21}^{\mathrm{cal}}$, and (f) s_{22}^{cal}.

one can not distinguish the two cuboids. Increasing the frequency to 35 GHz (Fig. 4.26) leads to improved resolution and the two cuboids are clearly distinguishable. This is in agreement with the theoretically calculated resolution. It is observed that the images obtained from the reflection *S*-parameters (s_{11} and s_{22}) have slightly better quality. We believe that it is due to the fact that the reflection *S*-parameters for the conductor are stronger than the transmission *S*-parameters (s_{21} and s_{12}).

Fig. 4.27 shows the reconstructed image as well as the cut-through image at $y = 0$ obtained from the calibrated complex s_{11} when we apply the method in [1] at 35 GHz. A comparison of Fig. 4.27 with Fig. 4.26 demonstrates that the proposed method can distinguish the two cubes better. This is due to the use of the simulated incident field E_x^{inc} instead of an assumed spherical wave. Also, our algorithm considers the attenuation term of $1/r$ in calculating the scattering function g_0 (refer to equation (4.3)), which is not the case in [1].

To examine the resolution of the method when different *S*-parameters have different resolutions (the cuboids are not in the middle of the two antennas), we simulate the setup shown in Fig. 4.23 at 35 GHz where the two cuboids are located at $\bar{z} = 10$ mm with $d = 2.5$ mm. In this case, the theoretical resolutions for s_{11}^{cal}, s_{12}^{cal}, and s_{22}^{cal} computed from (4.25) are 3.57 mm, 2.77 mm and 2.26 mm, respectively. Fig. 4.28 shows the reconstructed images as well as the cut-through plots at $y = 0$ when we use the calibrated *S*-parameters s_{11}^{cal}, s_{12}^{cal}, and s_{22}^{cal}. As observed from these figures, the two cuboids are not separated completely in the reconstructed images from s_{11} and s_{12}, while they are clearly separated in the reconstructed images from s_{22}, which is consistent with the theoretical resolution estimates.

4.3 THEORY OF 3-D MICROWAVE HOLOGRAPHY

The 3-D microwave holography setup in this work consists of two x-polarized dipole antennas and a 3-D target in between as shown in Fig. 4.29. The radiation field of the x-polarized antennas can be reasonably approximated by TM polarization. Thus, in this work we consider the x-components of the incident and scattered fields only. This leads to a simplified dyadic Green's function in which we only consider the G_x^x element. The antennas perform a 2-D scan while moving together on two separate planes positioned at $z=0$ and $z=D$. Assume that at any measurement frequency f_l $(l=1,2,\ldots,N_f)$, we know the incident field $s_0^{\text{inc}}(x,y,z,f_l)$ at any inspected target point (x,y,z) when the transmitting and receiving antennas are at $(0,0,0)$ and $(0,0,D)$, respectively. Let the signal $s(x',y',f_l)$ be the scattered wave received at (x',y',D), when the transmitting antenna is at $(x',y',0)$. Following Appendix A, this signal can be expressed as

$$\begin{aligned} s(x',y',f_l) &= \iiint_{z\,y\,x} f(x,y,z)\cdot\frac{s_0^{\text{inc}}(x-x',y-y',z,f_l)e^{-ik_l r}}{r}\,dxdydz \\ &= \iiint_{z\,y\,x} f(x,y,z)\cdot\frac{s_0(x'-x,y'-y,z,f_l)e^{-ik_l r}}{r}\,dxdydz \end{aligned} \qquad (4.28)$$

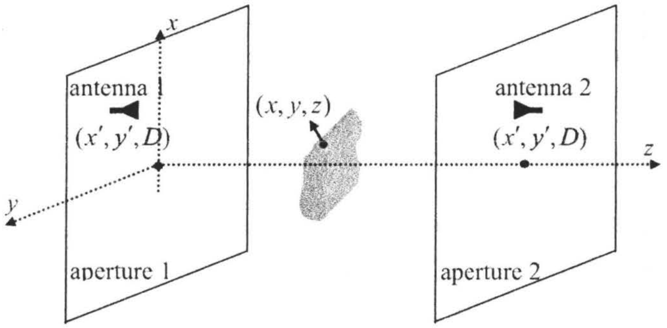

Fig. 4.29. 3-D microwave holography setup.

where $f(x,y,\bar{z}) = (k_s(x,y) - k_0)$ and is called the reflectivity function of the target (assumed to be constant over the frequency band of interest), $s_0(x,y,z,f_l)$ $= s_0^{\text{inc}}(-x,-y,z,f_l)$, G_x^x element has been approximated by $e^{-ik_l r}/r$ where $r = \sqrt{(x'-x)^2 + (y'-y)^2 + (D-\bar{z})^2}$ and k_l is the wavenumber in the background medium at the frequency f_l.

We define the scattering function $g_0(x,y,z,f_l)$ as

$$g_0(x,y,z,f_l) = \frac{s_0(x,y,z,f_l)\, e^{-ik_l r}}{r} \tag{4.29}$$

so that $s(x',y',f_l)$ in (4.28) is expressed as

$$s(x',y',f_l) = \int_z \int_y \int_x f(x,y,z) \cdot g_0(x'-x, y'-y, z, f_l)\, dx dy dz. \tag{4.30}$$

In the above equation, the integrals over x and y can be interpreted as a 2-D convolution integral. Thus, the 2-D FT of $s(x',y',f_l)$, $S(k_x,k_y,f_l)$, can be written as

$$S(k_x,k_y,f_l) = \int_z F(k_x,k_y,z)\, G_0(k_x,k_y,z,f_l)\, dz \tag{4.31}$$

where $F(k_x, k_y, z)$ and $G_0(k_x, k_y, z, f_l)$ are the 2-D FT of $f(x, y, z)$ and $g_0(x, y, z, f_l)$ while k_x and k_y are the Fourier variables with respect to x and y, respectively.

To reconstruct the reflectivity function $f(x, y, z)$, we approximate the integral in (4.31) by the following discrete sum with respect to z for N_z reconstruction planes

$$S(k_x, k_y, f_l) = \sum_{n=1}^{N_z} F(k_x, k_y, z_n) G_0(k_x, k_y, z_n, f_l) \Delta z \tag{4.32}$$

where Δz is the distance between two neighboring reconstruction planes.

Since we perform measurements at N_f frequencies, writing (4.32) for all frequencies leads to the following system of equations at each spatial frequency pair (k_x, k_y)

$$\begin{bmatrix} S(k_x, k_y, f_1) \\ \vdots \\ S(k_x, k_y, f_{N_f}) \end{bmatrix} = \begin{bmatrix} G_0(k_x, k_y, z_1, f_1)\Delta z & \cdots & G_0(k_x, k_y, z_{N_z}, f_1)\Delta z \\ \vdots & \ddots & \vdots \\ G_0(k_x, k_y, z_1, f_{N_f})\Delta z & \cdots & G_0(k_x, k_y, z_{N_z}, f_{N_f})\Delta z \end{bmatrix} \begin{bmatrix} F(k_x, k_y, z_1) \\ \vdots \\ F(k_x, k_y, z_{N_z}) \end{bmatrix} \tag{4.33}$$

Then, the system of equations (4.33) is solved with least-squares to find $F(k_x, k_y, z_n)$, $n = 1, 2, \ldots, N_z$. Once we obtain the values of $F(k_x, k_y, z_n)$ for all (k_x, k_y) spatial frequency pairs, we apply inverse 2-D FT to $F(k_x, k_y, z_n)$ to reconstruct a 2-D slice of the reflectivity function $f(x, y, z_n)$ at each $z = z_n$ plane. Then, the modulus $|f(x, y, z_n)|$, is plotted versus the spatial coordinates x and y

to show a 2-D image of the target at each $z = z_n$ plane. By putting together all 2-D slice images, a 3-D image of the target is obtained.

For the setup shown in Fig. 4.29, the acquired scattered waves are obtained by measuring the four complex *S*-parameters at the two antenna terminals at each scanning position on the apertures. These waves constitute four scattered signals as the one in (4.28). The collected data from each *S*-parameter can be processed separately as described above to create an image of the target. In this case, we obtain four separate images at each $z = z_n$ plane. Another approach is to reconstruct a single image from the data sets of all *S*-parameters. To implement this, we re-write (4.33) using all four *S*-parameters at each (k_x,k_y), assuming that $F(k_x,k_y,z_n)$ is the same in all four cases. The resulting system of equations is usually over-determined since at each (k_x,k_y), $4\times N_f$ equations need to be solved simultaneously to find N_z unknowns $F(k_x,k_y,z_n)$ $n=1,2,\cdots,N_z$. Again, a least-square solution is sought at each spatial-frequency pair (k_x,k_y) to find the corresponding values of $F(k_x,k_y,z_n)$.

4.3.1 Range and Cross-Range Resolutions in 3-D Holography

As suggested in [1], we approximate the resolution at the center frequency of the system bandwidth $f_c = (f_1 + f_{N_f})/2$. Thus, similarly to (4.25) in 2-D holography, the cross-range resolution is calculated as

$$\delta_x = \frac{\lambda_c}{2(\sin(\theta_t/2)+\sin(\theta_r/2))} \tag{4.34}$$

where λ_c is the wavelength corresponding to the frequency f_c, and θ_t and θ_r are the angles subtended by the transmitting and receiving apertures or the full beamwidths of the antennas, whichever is less.

The range resolution δ_z for small targets is approximately [1]

$$\delta_z = \frac{c}{2B} \tag{4.35}$$

where c is the wave velocity in the medium and B is the frequency bandwidth.

4.3.2 Spatial and Frequency Sampling in 3-D Holography

Similar to 2-D holography, the sampling rate can be expressed considering the Nyquist criterion as [1]

$$\Delta x < \lambda_{\min} / 4 \tag{4.36}$$

where $\lambda_{\min}$ is the wavelength corresponding the maximum frequency f_{N_f}.

The required frequency sampling is determined in a similar way. The maximum phase shift resulting from a change in the wavenumber Δk is $2\Delta k R_{\max}$, where $R_{\max}$ is the maximum target range. Requiring that this phase shift is less than π yields [1]

$$\Delta f < \frac{c}{4R_{\max}} \tag{4.37}$$

where Δf is the frequency sampling interval.

4.3.3 Reconstruction Results in 3-D Holography

To validate the accuracy of the proposed 3-D microwave holography technique, two $\lambda/2$ (at 35 GHz) horizontally-polarized (x-polarized) dipole antennas with targets in between are simulated in FEKO as shown in Fig. 4.30. The antennas perform a 2-D scan by moving together on aperture planes and collecting wideband data at each position. The aperture planes are located at z = 50 mm and z = 0 so that the examples represent near-field imaging. We refer to them as aperture 1 and aperture 2 corresponding to antenna 1 and antenna 2, respectively. The apertures have a size of 60 mm$\times$60 mm with their centers being on the z axis.

The S-parameters s_{jk}^{t} $(j,k = 1,2)$ for the two antennas are computed and recorded for every (x',y') position as the antennas perform the 2-D scan together on aperture 1 and aperture 2. The numerical noise is estimated through the numerical convergence error which is 0.02 for the magnitude of the S-parameters. The proposed holography technique is applied to the calibrated S-parameters as discussed before.

Since the dipoles are horizontally polarized along the x axis, the x-component of the simulated incident electric field $E_x^{\mathrm{inc}}(x,y)$ is recorded at the imaged planes $z=z_n$, $n=1,2,\cdots,N_z$. These planes are of size 40 mm$\times$40 mm. Thus, the recorded $E_x^{\mathrm{inc}}(x,y)$ at the planes $z=z_n$ $(n=1,2,\cdots,N_z)$ at each sampling frequency f_l is considered as $s_0^{\mathrm{inc}}(x,y,z_n,f_l)$.

The wideband data is in the range of 25 GHz to 45 GHz. This gives a range resolution of $\delta_z=7.5$ mm as per (4.35). Since $\Delta z \geq \delta_z$ must be fulfilled, in all examples, we set the distance between the reconstruction planes as 8 mm. Also N_z equals 5 in our examples. Since the maximum frequency in the simulations is 45 GHz, from (4.36), the spatial sampling rate for the 2-D scan has to be smaller than 1.6 mm. Therefore, a sampling rate of 1.5 mm along both x and y is adopted. Also, we approximate the minimum number of frequencies from (4.37) which depends on $R_{\max}$. For example, for $R_{\max}$ being 40 mm, the maximum Δf is 1.8 GHz. Here, we use $\Delta f = 2$ GHz which leads to 11 frequencies in the range of 25 GHz to 45 GHz. We note that in section 4.3.3.2 we study the effect of increasing and decreasing the number of frequencies.

4.3.3.1 Reconstruction Examples

In the first example, two dielectric cuboids with a side of 3 mm and wall-to-wall distance of 6 mm are placed midway between the two antennas at $z = 25$ mm as shown in Fig. 4.30(a). The constitutive parameters of the cuboids are $\varepsilon_r = 2$ and $\sigma = 0$ S/m while the background is free space. The separation distance between the reconstruction planes along the range ($z = z_n$ planes, n = 1,2,…,5) is 8 mm. The system of equations (4.33) is solved at each spatial-frequency pair (k_x, k_y) when the S-parameters are used separately to reconstruct the 2-D images on 5 planes along the z axis. Figs. 4.31 to 4.33 show the reconstructed images obtained from the reflection and transmission S-parameters. As Figs. 4.31 and 4.32 show, the images obtained from s_{11} and s_{22} reconstruct the target at the plane $z = 25$ mm properly but also show some artifacts 8 mm away.

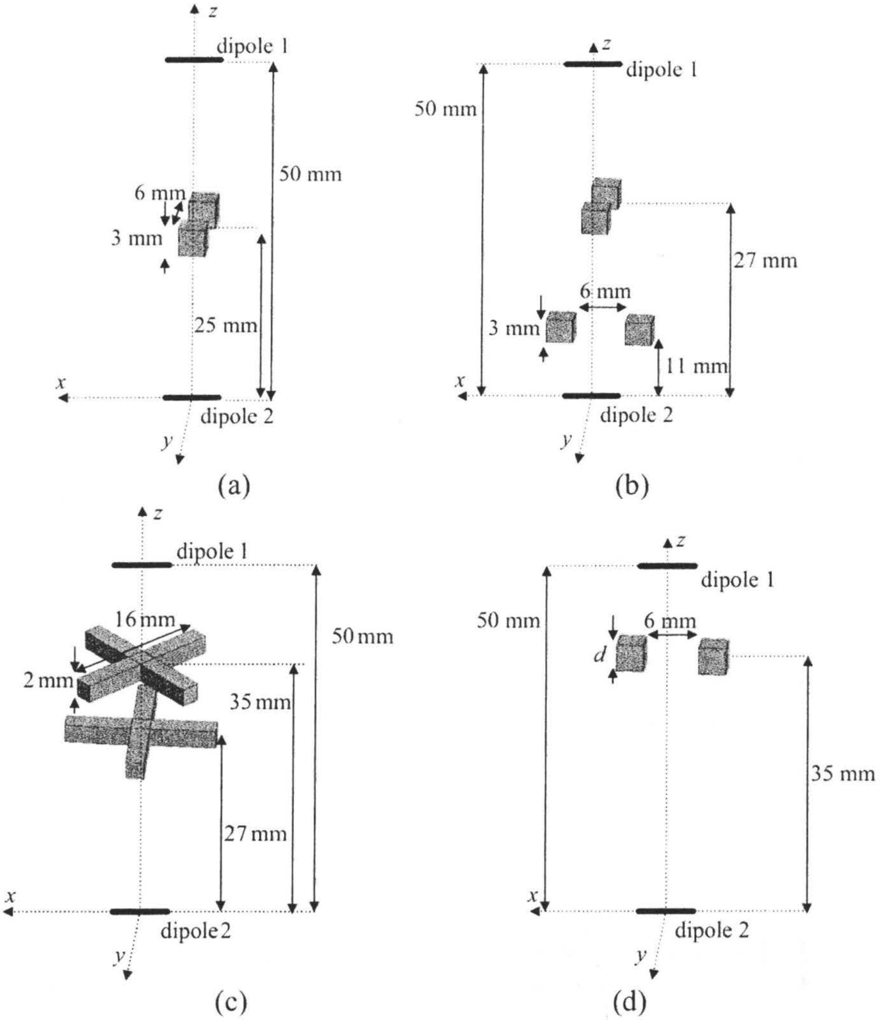

Fig. 4.30. Dielectric targets in free space scanned by two $\lambda/2$ (at 35 GHz) horizontally-polarized (x-polarized) dipoles; dipole 1 is moving on the z = 50 mm plane while dipole 2 is moving on the z = 0 mm plane. The simulated S-parameters are recorded in the frequency band of 25 GHz to 45 GHz for: (a) two identical cuboids with sides of 3 mm, centered at (0,-4.5,25) mm and (0,4.5,25) mm with dielectric properties of $\varepsilon_r = 2$ and $\sigma = 0$ S/m; (b) four identical cuboids with sides of 3 mm, centered at (-4.5,0,11) mm, (4.5,0,11) mm, (0,-4.5,27) mm, and (0,4.5,27) mm and all having dielectric properties of $\varepsilon_r = 2$ and $\sigma = 0$ S/m; (c) two identical X-shape objects with square cross-sections 2 mm on a side and length of each arm 16 mm, parallel to the x-y plane, one centered at (0,0,27) mm with its arms along the x and y axes, the other one centered at (0,0,35) mm, with the arms rotated by 45 degrees with respect to the x and y axes, both targets having dielectric properties of $\varepsilon_r = 2$ and $\sigma = 0$ S/m; (d) two identical cuboids with sides of d, centered at (-4.5,0,35) mm and (4.5,0,35) mm, with dielectric properties $\varepsilon_r = 5$ and $\sigma = 0$ S/m.

The images obtained from s_{21} are not conclusive at all although the image obtained at $z = 25$ mm plane is good [refer to Fig. 4.33]. Using s_{12} leads to similar results as s_{21}.

Next, we solve the systems of equations (4.33) when all the *S*-parameters are used simultaneously. In this case, at each (k_x, k_y), 44 equations are available to find the 5 unknowns $F(k_x, k_y, z_n)$, $n = 1, 2, \ldots, 5$. Fig. 4.34 shows the reconstructed images. It is observed that the targets are reconstructed properly at the plane $z = 25$ mm. At the same time, the images at the other range locations do not contain artifacts. For this example, the cross-range resolution estimated from (4.34) is 3.8 mm. Thus, the two targets, which are 6 mm apart, are resolved well.

From now on, we only present the results when the data collected from all *S*-parameters contribute simultaneously to the image reconstruction.

In the next example, a more challenging recosntruction problem is solved. As shown in Fig. 4.30(b), a pair of cuboids similar to those in Fig. 4.30(a) is placed at $z = 11$ mm and another identical pair of cuboids, rotated by 90° about the z axis, is placed at $z = 27$ mm. The constitutive parameters of the cuboids are $\varepsilon_r = 2$ and $\sigma = 0$ S/m while the background is free space. Fig. 4.35 shows the reconstructed images. It is observed that the targets are recovered well in the planes at $z = 11$ mm and $z = 27$ mm. Also, the images at the other range locations do not show artifacts.

As a third example, we consider more complex shapes. As shown in Fig. 4.30(c), an "X" shape object parallel to the x-y plane is placed at $z = 27$ mm. The

"X" shape object is created from two arms of length 16 mm and cubic cross-sections 2 mm on a side. Another identical "X" shape object is rotated by 90° about the z axis and is placed at $z = 35$ mm. The constitutive parameters of the objects are $\varepsilon_r = 2$ and $\sigma = 0$ S/m while the background is free space. The distance between the two objects is 8 mm, which is very close to the range resolution limit $\delta_z = 7.5$ mm. Fig. 4.36 shows the reconstructed images. The targets are recovered well at $z = 27$ mm and $z = 35$ mm. The images formed at other range locations do not show significant artifacts.

Figs. 4.37 and 4.38 show the reconstructed images for the targets in Fig. 4.30(c) when applying the 3-D holography technique presented in [1]. Note that this technique can make use of the reflection (back-scattered) signals only. The same number of frequencies is adopted and the reconstructed images are shown on the same planes. As observed, some artifacts are present and the target shapes are not recovered well. For the sake of comparison, Figs. 4.39 and 4.40 show the reconstructed images obtained from our proposed technique where only the reflection S-parameters are processed. The comparison of the images in Figs. 4.37 and 4.38 with those in Figs. 4.39 and 4.40 confirms the advantages of using adequate representation of the incident field in our formulation instead of using a spherical wave assumption as in [1]. The latter assumption is inadequate in near-field imaging. In addition, the possibility of using transmission S-parameters in conjunction with the reflection ones in our technique leads to even better results as shown in Fig. 4.36.

4.3.3.2 Effect of Number of Frequencies

For the three examples presented above, we have used the data recorded at 11 frequencies in the range of 25 GHz to 45 GHz ($\Delta f = 2$ GHz). We observe that when using the data at more frequencies, e.g., 21 frequencies or $\Delta f = 1$ GHz, the quality of the reconstructed images remains almost the same. Also, we observe that very similar results with slight degradation of quality are obtained when using the simulated data only at 5 frequencies in the same band ($\Delta f = 5$ GHz). However, reducing the number of frequencies to 3 ($\Delta f = 10$ GHz) or 2 ($\Delta f = 20$ GHz) leads to serious degradation of the reconstructed images. As an

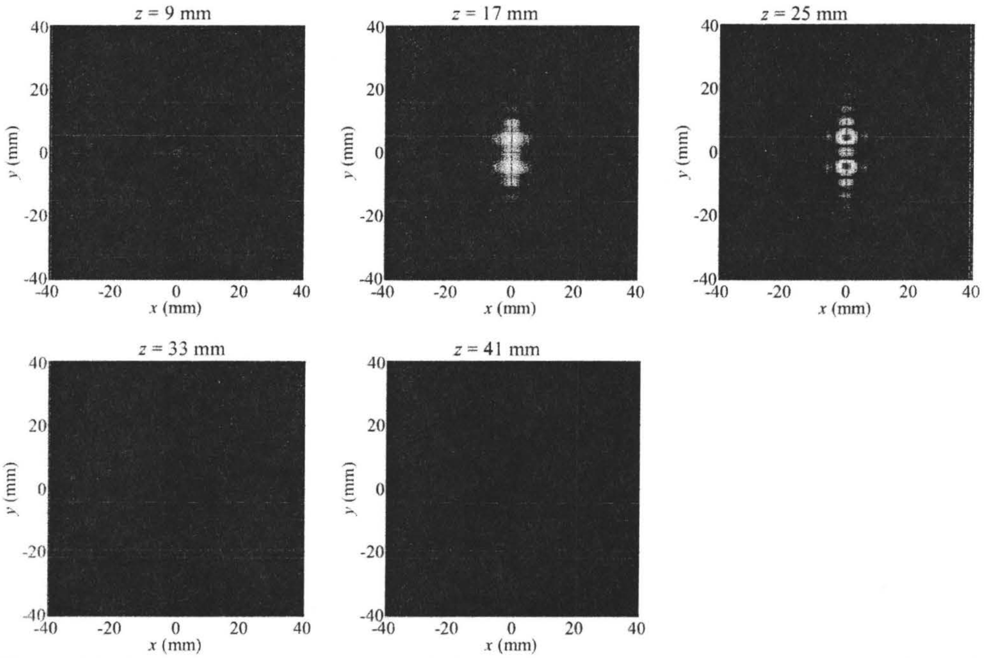

Fig. 4.31. Reconstructed images of the dielectric target in Fig. 4.30(a) when the system of equations in (4.33) is solved using only s_{11}^{cal}.

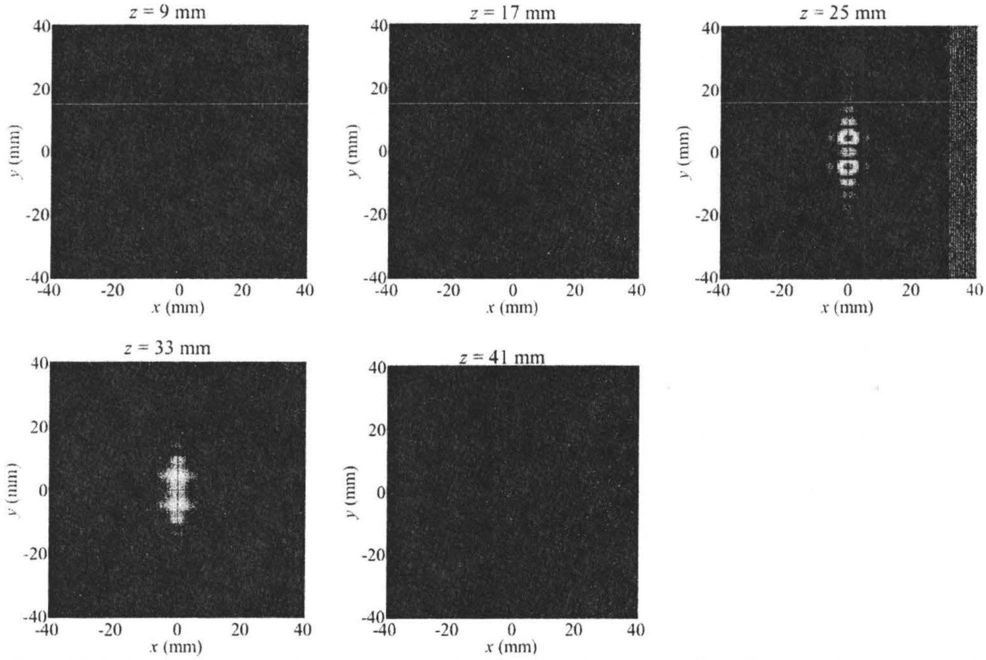

Fig. 4.32. Reconstructed images of the dielectric target in Fig. 4.30(a) when the system of equations in (4.33) is solved using only s_{22}^{cal}.

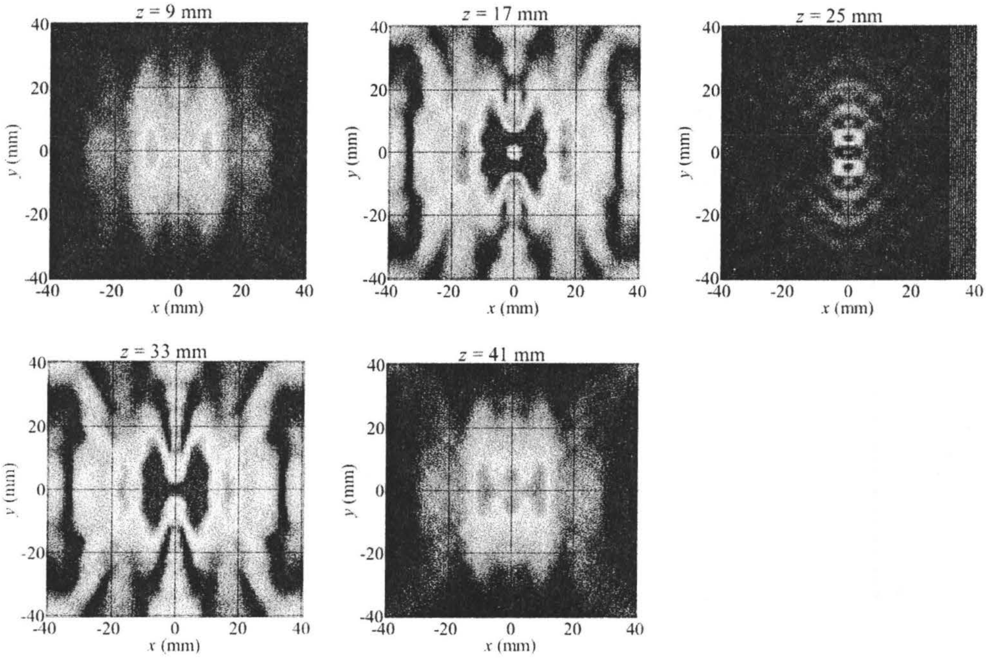

Fig. 4.33. Reconstructed images of the dielectric target in Fig. 4.30(a) when the system of equations in (4.33) is solved using only s_{21}^{cal}.

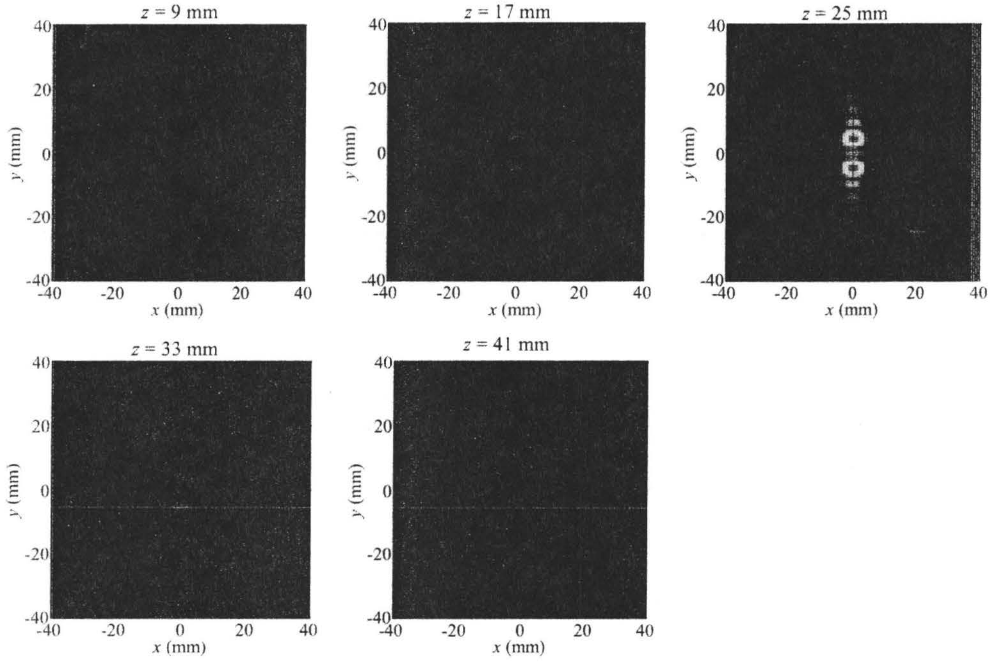

Fig. 4.34. Reconstructed images when using all *S*-parameters simultaneously for the dielectric targets in Fig. 4.30(a).

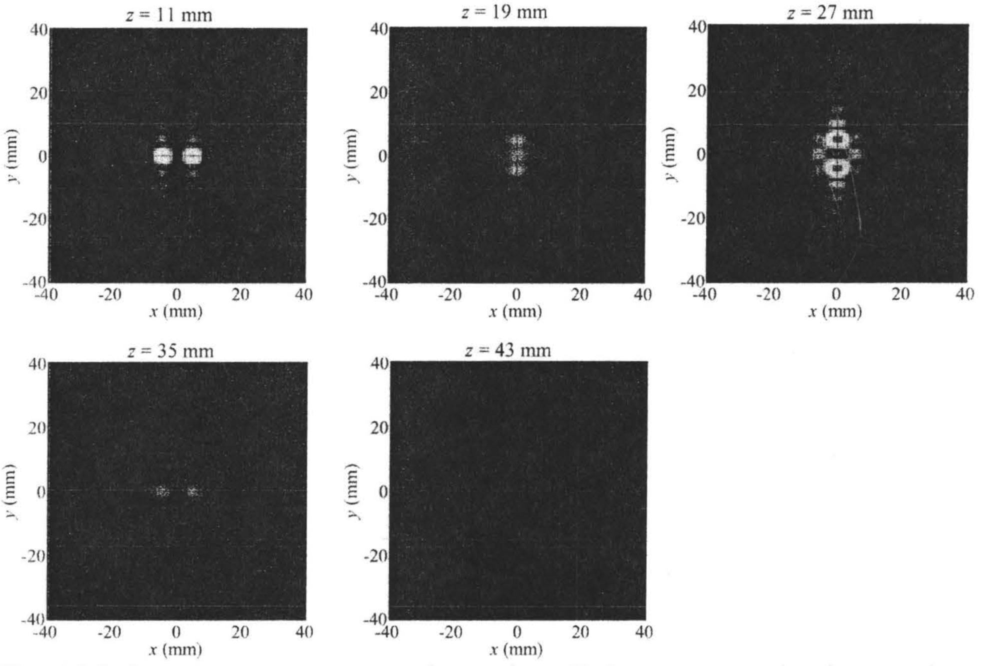

Fig. 4.35. Reconstructed images when using all *S*-parameters simultaneously for the dielectric targets in Fig. 4.30(b).

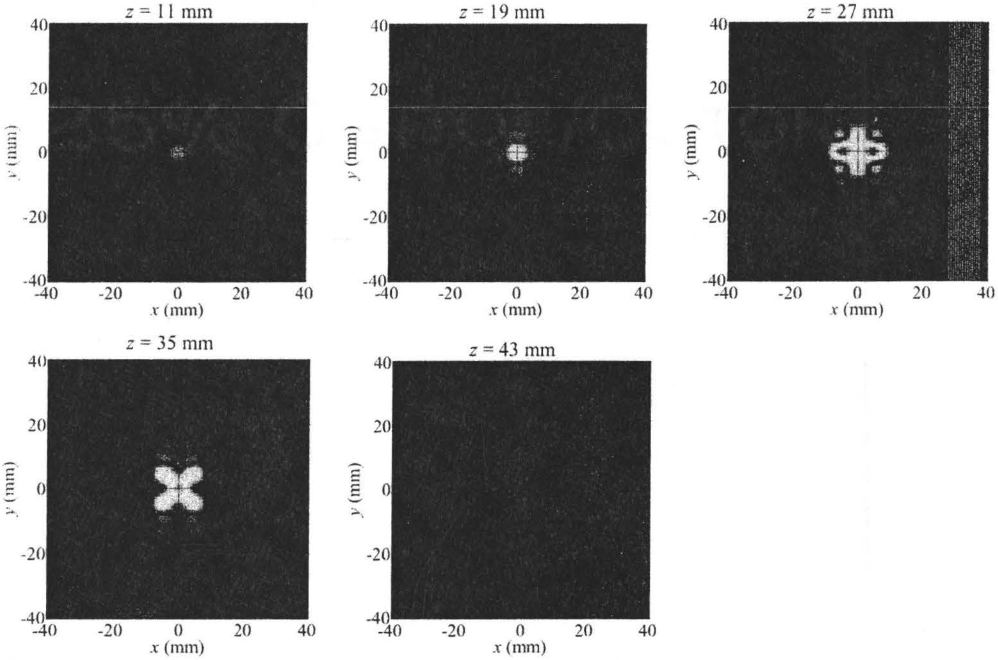

Fig. 4.36. Reconstructed images when using all *S*-parameters simultaneously for the dielectric targets in Fig. 4.30(c).

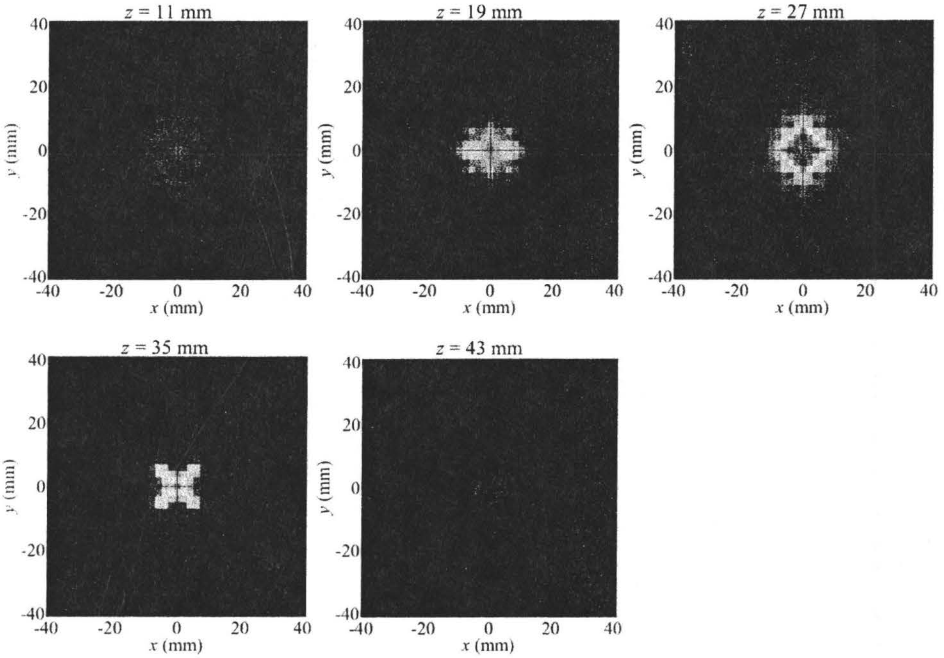

Fig. 4.37. Reconstructed images obtained from the simulation of dielectric targets in Fig. 4.30(c) when applying the 3-D holography technique in [1] to s_{11}^{cal}.

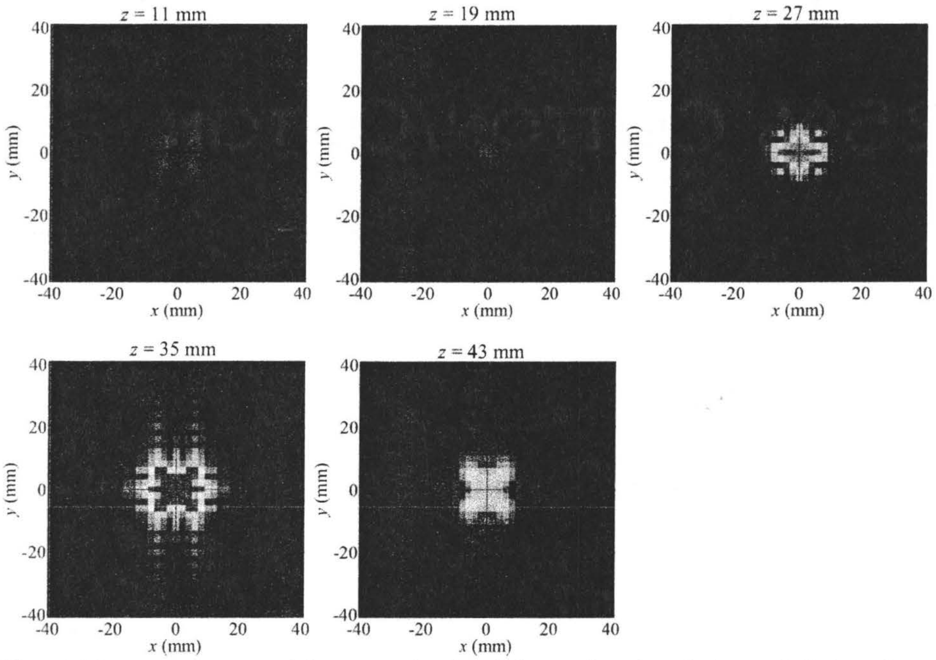

Fig. 4.38. Reconstructed images obtained from the simulation of dielectric targets in Fig. 4.30(c) when applying the 3-D holography technique in [1] to s_{22}^{cal}.

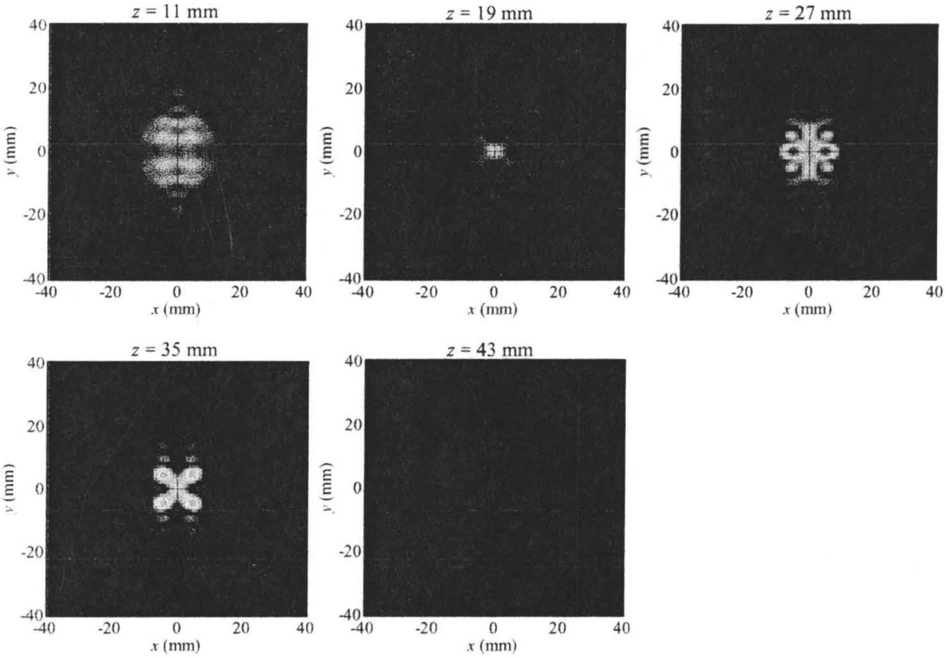

Fig. 4.39. Reconstructed images obtained from the simulation of dielectric targets in Fig. 4.30(c) when applying our proposed 3-D holography technique to s_{11}^{cal}.

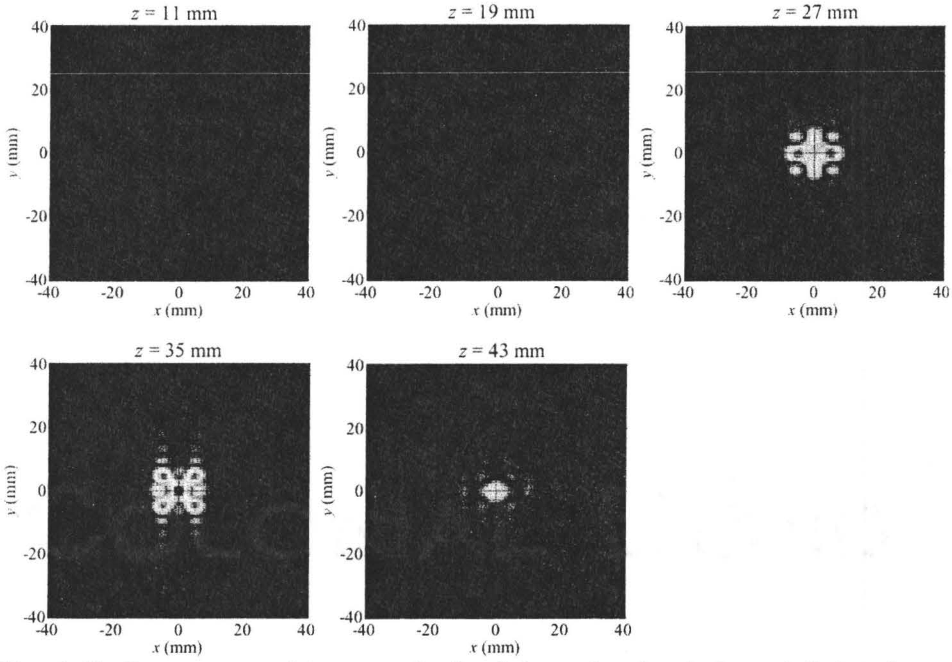

Fig. 4.40. Reconstructed images obtained from the simulation of dielectric targets in Fig. 4.30(c) when applying our proposed 3-D holography technique to s_{22}^{cal}.

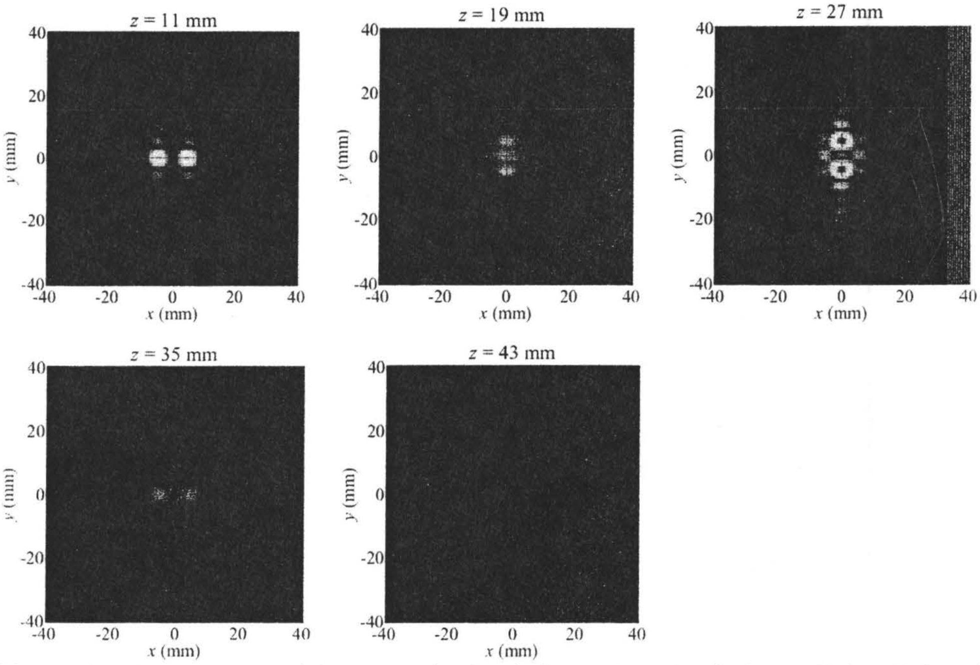

Fig. 4.41. Reconstructed images obtained from the simulation of the dielectric target in Fig. 4.30(b) when using 5 frequencies ($N_f = 5$).

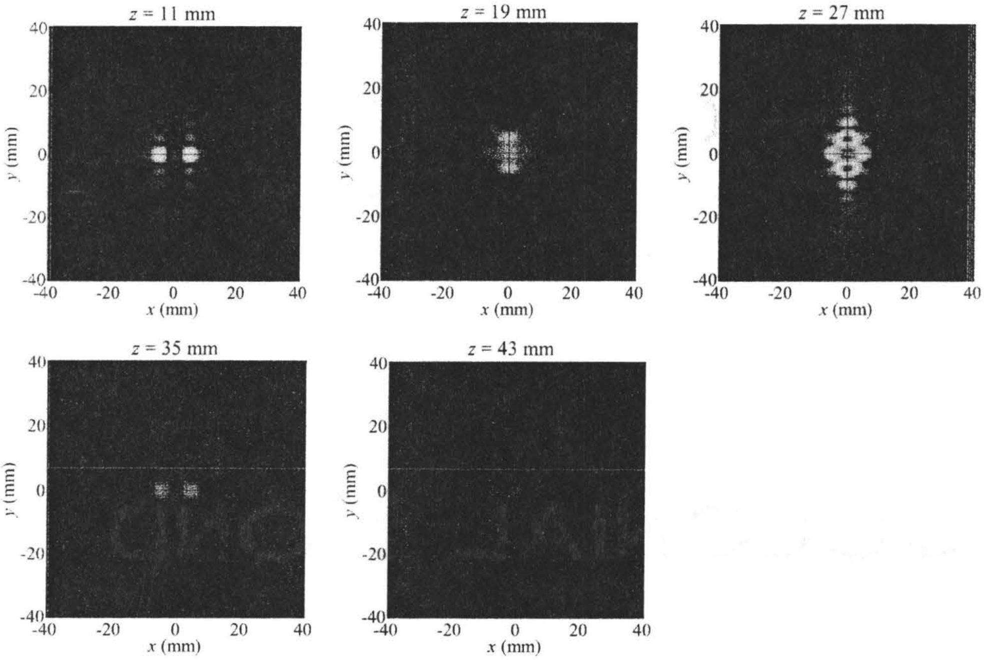

Fig. 4.42. Reconstructed images obtained from the simulation of the dielectric target in Fig. 4.30(b) when using 3 frequencies ($N_f = 3$).

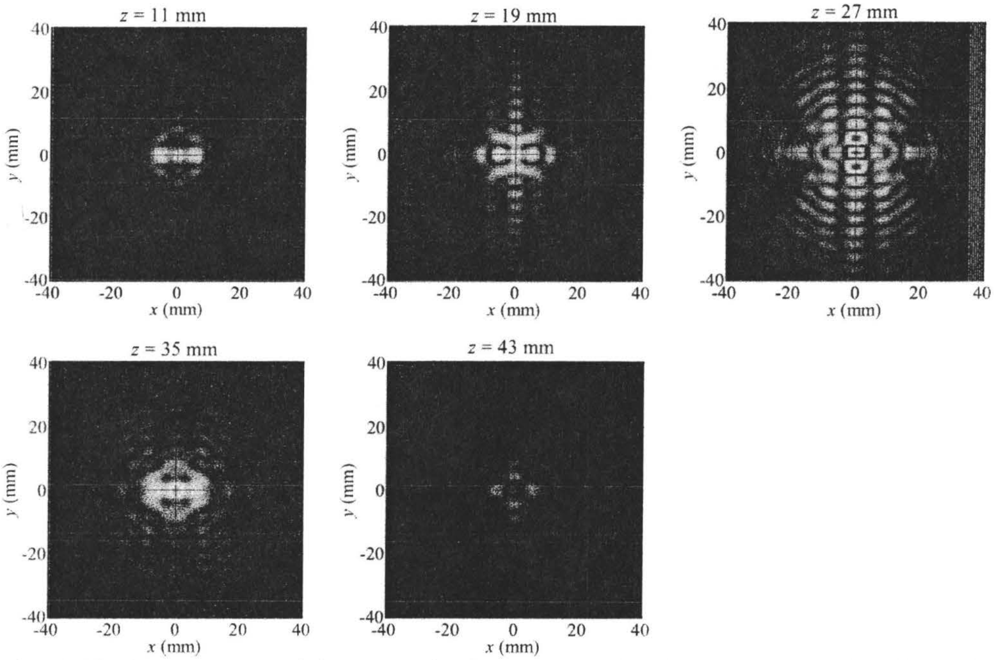

Fig. 4.43. Reconstructed images obtained from the simulation of the dielectric target in Fig. 4.30(b) when using 2 frequencies ($N_f = 2$).

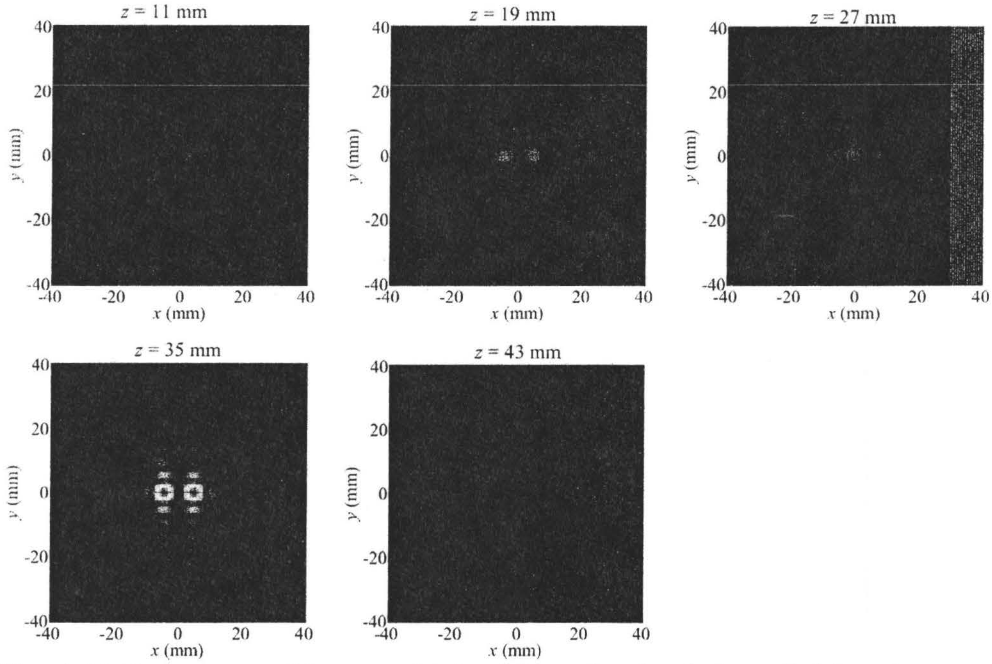

Fig. 4.44. Reconstructed images obtained from the simulation of dielectric targets in Fig. 4.30(d) with $d = 2$ mm.

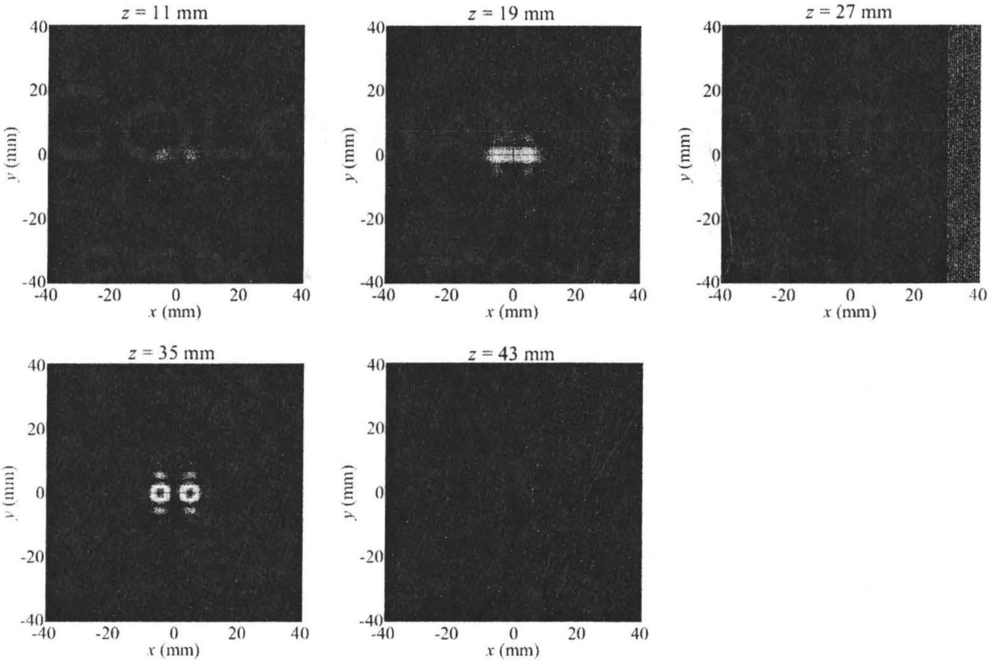

Fig. 4.45. Reconstructed images obtained from the simulation of dielectric targets in Fig. 4.30(d) with $d = 2.6$ mm.

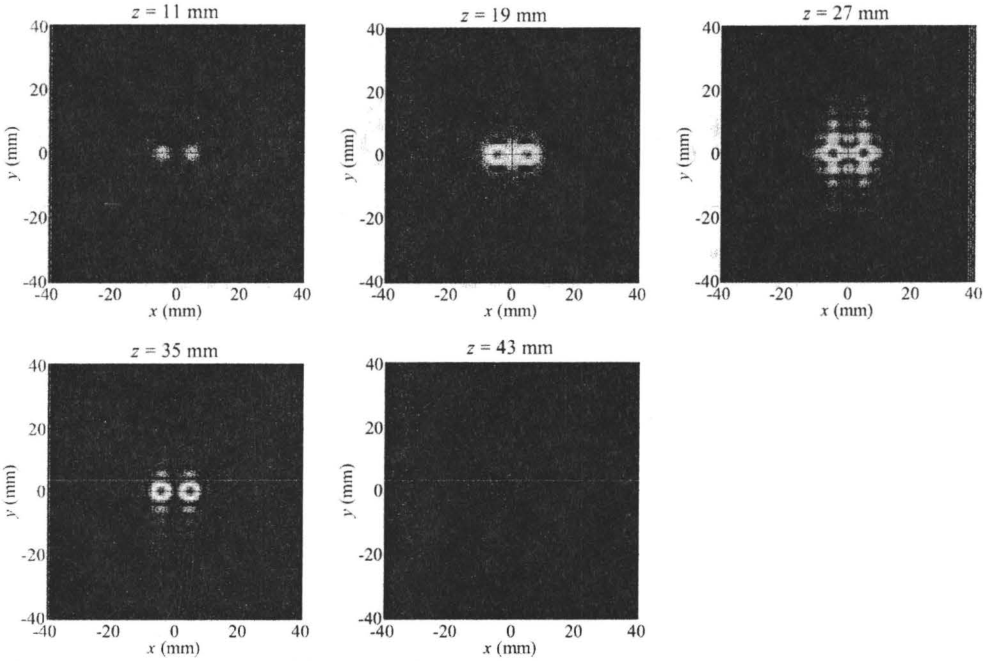

Fig. 4.46. Reconstructed images obtained from the simulation of dielectric targets in Fig. 4.30(d) with $d = 3$ mm.

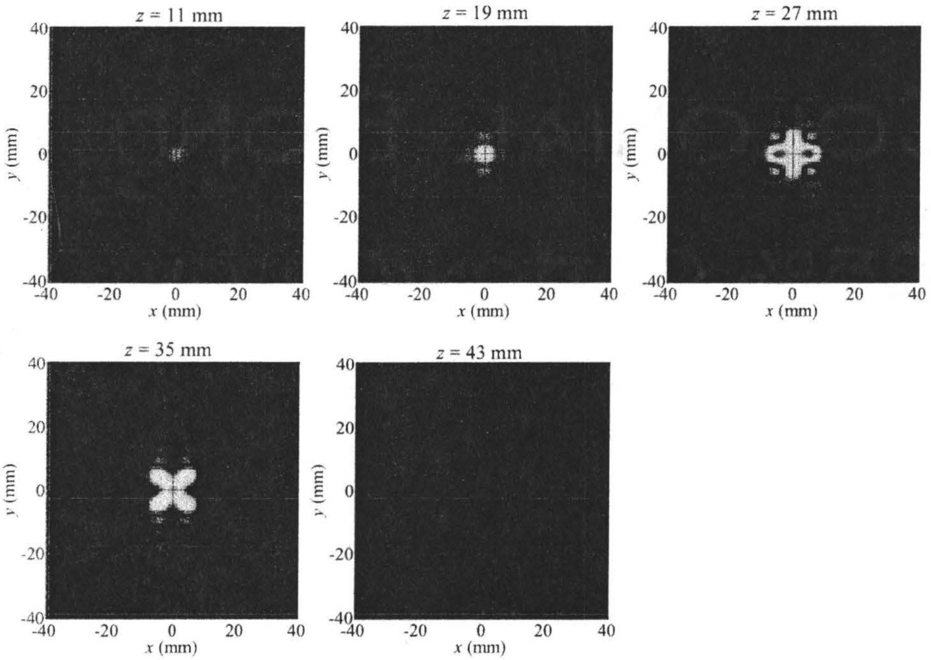

Fig. 4.47. Reconstructed images for the example of Fig. 4.30(c) when adding noise to the complex *S*-parameters with SNR = 0 dB.

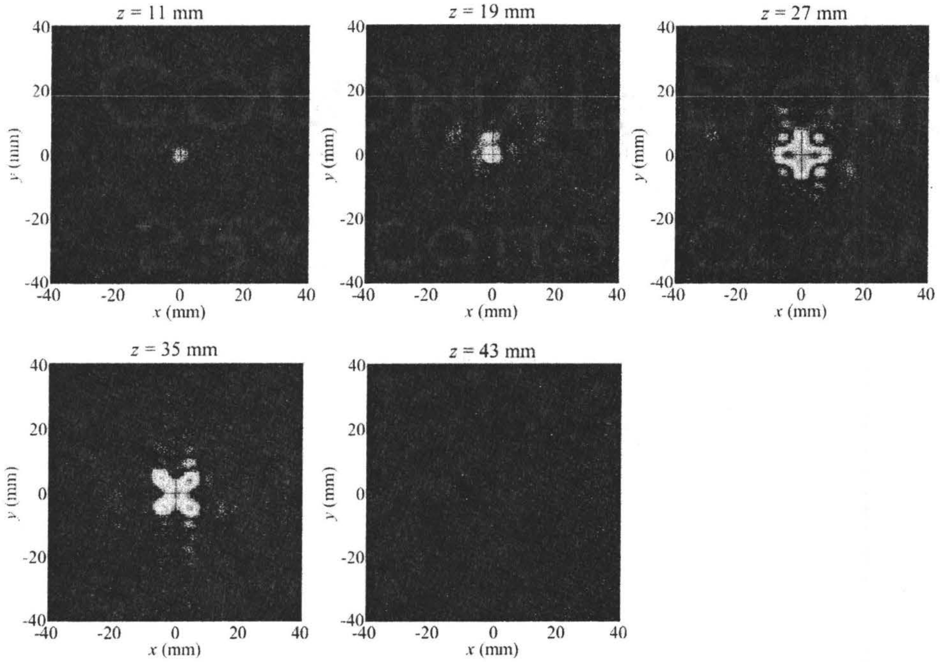

Fig. 4.48. Reconstructed images for the example of Fig. 4.30(c) when adding noise to the complex S-parameters with $\mathrm{SNR} = -10$ dB.

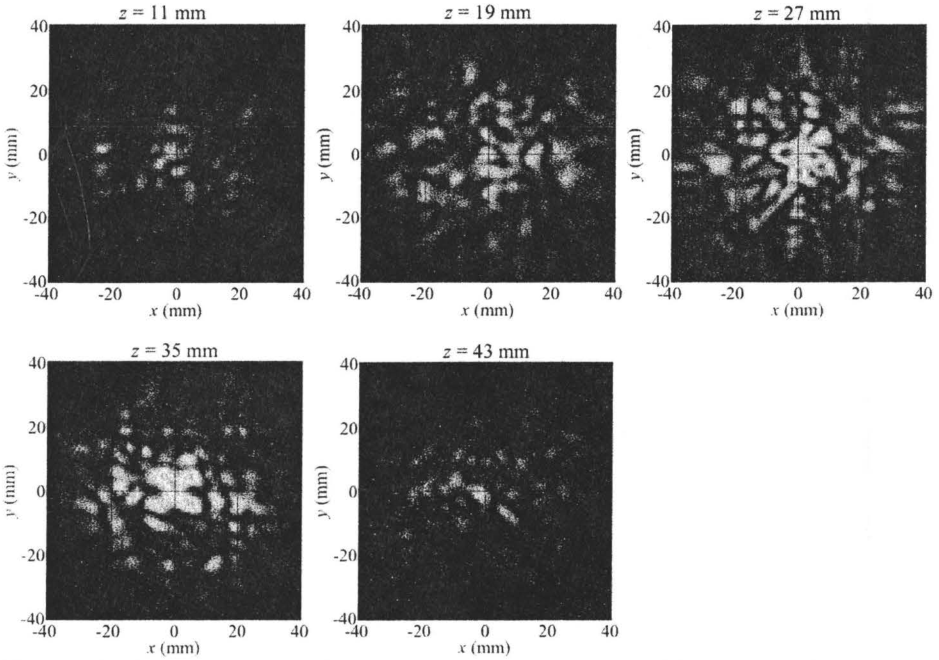

Fig. 4.49. Reconstructed images for the example of Fig. 4.30(c) when adding noise to the complex S-parameters with $\mathrm{SNR} = -20$ dB.

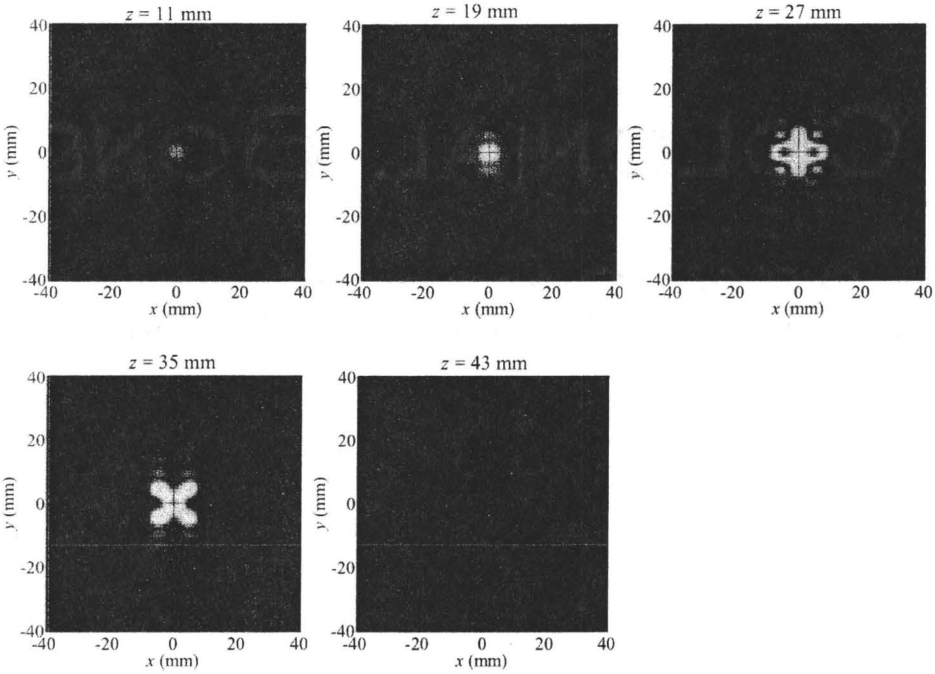

Fig. 4.50. Reconstructed images for the example of Fig. 4.30(c) when adding noise only to the phase of the *S*-parameters with SNR = 20 dB.

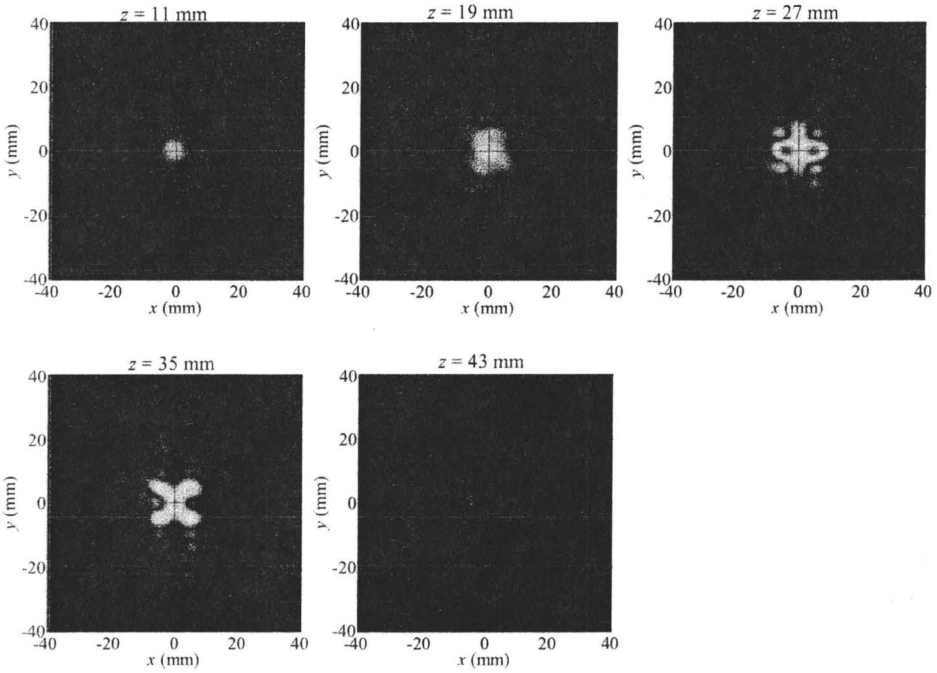

Fig. 4.51. Reconstructed images for the example of Fig. 4.30(c) when adding noise only to the phase of the *S*-parameters with SNR = 10 dB.

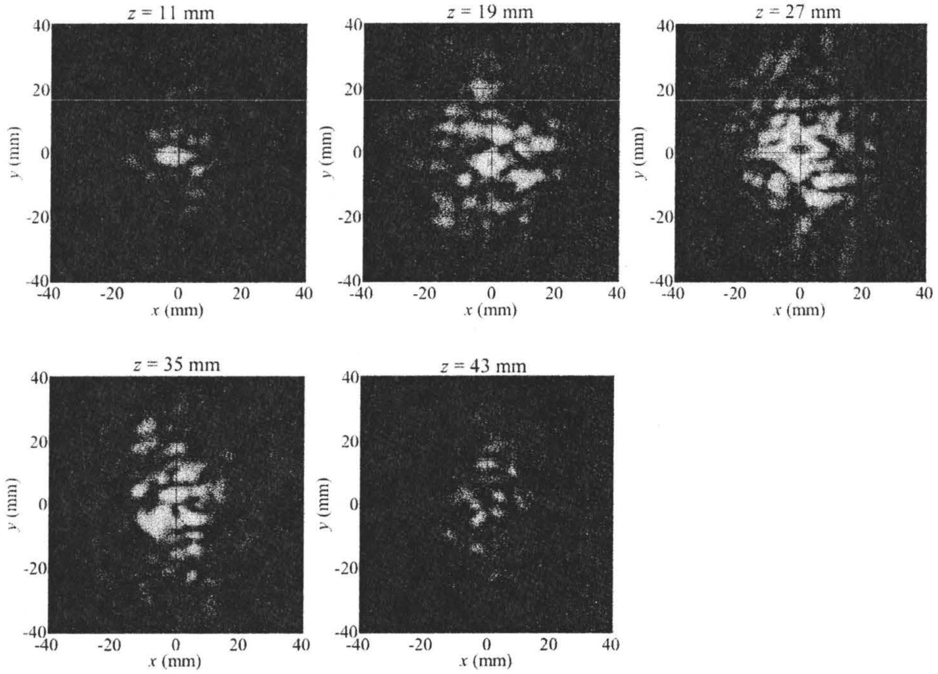

Fig. 4.52. Reconstructed images for the example of Fig. 4.30(c) when adding noise only to the phase of the *S*-parameters with SNR = 0 dB.

example, Figs. 4.41, 4.42, and 4.43 show the results of reconstructing the targets in Fig. 4.30(b) with the data recorded at 5, 3, and 2 frequencies, respectively.

4.3.3.3 Reconstruction for Larger Target Sizes

To investigate the quality of imaging for targets with higher dielectric property contrast, a pair of cuboids are placed at z = 35 mm as shown in Fig. 4.30(d). The constitutive parameters of the cuboids in this example are $\varepsilon_r = 5$ and $\sigma = 0$ S/m while the background is free space. Three cases are investigated where the cuboids have a side of d = 2 mm, 2.6 mm, and 3 mm. Fig. 4.44 shows the reconstructed images for the case of d = 2 mm. It is clear that the objects are reconstructed well. However, for larger objects (d = 2.6 mm and 3 mm), the quality degrades, i.e., artifacts appear. We believe that the degradation of the images when increasing the size of the cuboids is due to the fact that the criterion for the first-order Born approximation [16] is violated for larger cuboids. This approximation is indeed used in deriving (4.28) when approximating the field inside the targets with the incident field. The condition for applying first-order Born approximation is that the radius a of the sphere circumscribing the target and the refractive index n satisfy

$$(n-1)a < \frac{\lambda_{\min}}{4}. \tag{4.38}$$

For $\varepsilon_r = 5$, $n = 2.23$. Thus, for $f_{N_f} = 45$ GHz ($\lambda_{\min} = 6.7$ mm), the radius of the object needs to be smaller than 1.4 mm for the linear Born approximation to hold.

4.3.3.4 Effect of Random Noise on the Reconstruction Results

In order to investigate the effect of random noise on the proposed 3-D holography technique, we consider two types of noise: 1) white Gaussian noise added to the complex values of the *S*-parameters (such noise could be produced by electronic devices or the environment), 2) white Gaussian noise added only to the phase of the *S*-parameters (such noise could be due to the mechanical vibrations of the antennas during the 2-D scan). For both types, we apply high levels of noise. In the first case, the signal-to-noise ratios (SNR) are 0 dB, -10 dB, and -20 dB, while for the second type of noise, the SNRs are 20 dB, 10 dB, and 0 dB.

Figs. 4.47 to 4.52 show the reconstructed images for the targets in Fig. 4.30(c) when adding noise of type 1 and 2, respectively. For SNR value as low as -10 dB for the first type of noise and 10 dB for the second type, the quality of the reconstructed images is still comparable to that of the images obtained from noiseless data [see Fig. 4.36]. This indicates that the proposed reconstruction technique is very robust to noise.

4.4 SUMMARY

In this chapter, we presented 2-D and 3-D holography techniques for near-field microwave imaging of dielectric targets. The data is acquired by two antennas moving on two parallel apertures on the opposite sides of the inspected region and recording single frequency (in the 2-D technique) or wideband data (in the 3-D technique) at each position. The reconstruction algorithm is based on the Fourier-transform and a least-square solution. This direct inversion algorithm is indeed fast and can perform in real time. The incident field due to the transmitting antenna is simulated or measured on the reconstruction planes prior to the data acquisition. The advantages of this technique compared to the previously proposed 3-D holography technique [1] are: (1) the incident field can have any arbitrary distribution in the region of interest; (2) forward-scattered signals can contribute in image reconstruction in addition to the back-scattered signals. These two factors lead to enhancements of the reconstructed images especially in near-field imaging.

REFERENCES

[1] D. M. Sheen, D. L. McMakin, and T. E. Hall, "Three-dimensional millimeter-wave imaging for concealed weapon detection," *IEEE Trans. on Microwave Theory and Tech.*, vol. 49, no. 9, pp. 1581–1592, 2001.

[2] N H Farhat, "Microwave holography and its applications in modern aviation," *Proc. SPIE Eng. Applicat. Holography Symp.*, pp. 295–314, 1972.

[3] D. M. Sheen, D. L. McMakin, and T. E. Hall, "Near field imaging at microwave and millimeter wave frequencies," *IEEE/MTT-S Int. Microwave Symp.*, pp. 1693–1696, 2007.

[4] N. H. Farhat and W. R. Guard, "Millimeter wave holographic imaging of concealed weapons," *Proc. of the IEEE*, vol. 59, pp. 1383–1384, 1971.

[5] J. Detlefsen, A. Dallinger, and S. Schelkshorn, "Effective reconstruction approaches to millimeter-wave imaging of humans," *XXVIIIth General Assembly of Int. Union of Radio Science (URSI)*, pp 23–29, 2005.

[6] D. Slater, *Near-Field Antenna Measurements*, Artech House, Boston, 1991.

[7] M. Elsdon, M. Leach, S. Skobelev, and D. Smith, "Microwave holographic imaging of breast cancer," *IEEE Int. Symp. on Microwave, Antenna, Propag., and EMC Tech. For Wireless Commun.*, pp. 966–969, 2007.

[8] J. T. Case, I. Robbins, S. Kharkovsky, F. Hepburn, and R. Zoughi, "Microwave and millimeter wave imaging of the space shuttle external fuel tank spray on foam insulation (SOFL) using synthetic aperture focusing techniques," (SAFT) *Review of Quantitative Nondestructive Evaluation*, vol. 25, pp. 1546–1553, 2006.

[9] M. Ravan, R. K. Amineh, and N. K. Nikolova, "Two-dimensional near-field microwave holography," accepted for publication in *Inverse Problems*.

[10] M. Ravan, R. K. Amineh, and N. K. Nikolova, "Microwave holography for near-field imaging," *AP-S/URSI 2010*, Canada.

[11] M. Ravan, R. K. Amineh, and N. K. Nikolova, "Near-field microwave holographic imaging: target localization and resolution study," *URSI/EMTS 2010*, Germany.

[12] R. K. Amineh, M. Ravan, and N. K. Nikolova, "Three-dimensional microwave holography for near-field imaging of dielectric bodies," submitted to *Inverse Problems*.

[13] D. Pozar, *Microwave Engineering*, John Wiley & Sons, Inc., 2005.

[14] A. Banos, *Dipole Radiation in the Presence of a Conducting Half-Space*, Pergamon Press, New York, 1966.

[15] D. C. Munson, J. D. Jr. O'Brien, and W. K. Jenkins, "A tomographic formulation of spotlight-mode synthetic aperture radar," *Proc. of the IEEE*, vol. 71, no. 8, pp. 917–925, 1983.

[16] EM Software & Systems-S.A. (Pty) Ltd., http://www.feko.info.

[17] M. Slaney, A. C. Kak, and L. E. Larsen, "Limitation of imaging with first-order diffraction tomography," *IEEE Trans. on Microwave Theory and Tech.*, vol. 32, no. 8, pp. 860–874, 1984.

CHAPTER 5

DEFECT SIZING IN METALLIC STRUCTURES USING MAGNETIC FLUX LEAKAGE TECHNIQUE

5.1 INTRODUCTION

The magnetic flux leakage (MFL) measurements play an important role in the nondestructive testing (NDT) of buried oil and gas pipelines in order to find metal-loss regions usually caused by corrosion, fatigue, etc. The size and shape of the defects can be obtained by studying the distribution of the MFL output signal. After the leakage field is measured, an inverse problem must be solved so that the shape characteristics of the flaw, such as width, length, and depth can be estimated. The correct assessment of this information is vital in order to determine critical regions in the pipelines.

The MFL inversion techniques often use an iterative approach where a forward model calculates the leakage field for a given set of defect parameters. Three major groups of forward models are commonly used. The first group involves numerical simulations typically based on the finite element method (FEM) [1]-[3]. These models provide accurate results but the drawback is that they are computationally very demanding. The second group consists of closed-form analytical formulas for defects of certain canonical shapes [4]-[7]. These models typically utilize magnetic poles or a dipolar charge on the defect walls. They are very fast but less accurate and versatile due to the assumptions made in deriving the analytical formulas [5][7]. The third group of forward MFL models is based on artificial neural networks for two-dimensional and three-dimensional flaws [8]-[12]. These models are fast but are limited to the region in parameter space for which the neural network is trained.

The work in this chapter is two-fold. In the first part, a direct procedure is proposed for full characterization of rectangular surface-breaking cracks based on the measurements of only one tangential component of the magnetic field with the MFL technique. The parameters of interest include orientation, length, and depth of the cracks. In the second part, a space-mapping methodology is proposed to expedite the optimization process for two types of defects: rectangular cracks and cylindrical pits. The work in this chapter has been presented in [13]-[17].

5.2 DIRECT INVERSION TECHNIQUE FOR RECTANGULAR CRACKS

The most critical defects associated with pipelines are crack-like defects (welding cracks, fatigue cracks, stress corrosion cracks, hydrogen-induced cracks, and sulfide corrosion cracks [18]). For these surface breaking cracks, the length l and the depth d are typically much larger than the crack width w so that the variation of the MFL signal with respect to the width is negligible (Fig. 5.1). It is also assumed that the investigated cracks are straight along their length and the crack walls are perpendicular to the metal surface. Furthermore, small irregularities in the depth (the bottom of the crack) are ignored since they have negligible effect on the MFL response [4]. Therefore, the parameters of interest are the length l, the depth d, and the orientation θ of the crack.

The location of the peaks in the normal z-component (Fig. 5.1) of the magnetic field gives a proper approximation of the length of a crack which is along the direction of the applied field [4][5][19][20]. However, in practice, cracks may have arbitrary orientations (θ in Fig. 5.1). More importantly, the z-component of the magnetic field is often not available.

Regarding the depth, calibration of the MFL signals in terms of defect depth has been studied both through finite-element modeling [19]-[23] and through analytical methods [4][24]. However, the obtained calibration curves do not take into account the effect of the crack length on the signal strength. Here, we show that neglecting the crack length in constructing the calibration curves may lead to significant errors in the depth estimation.

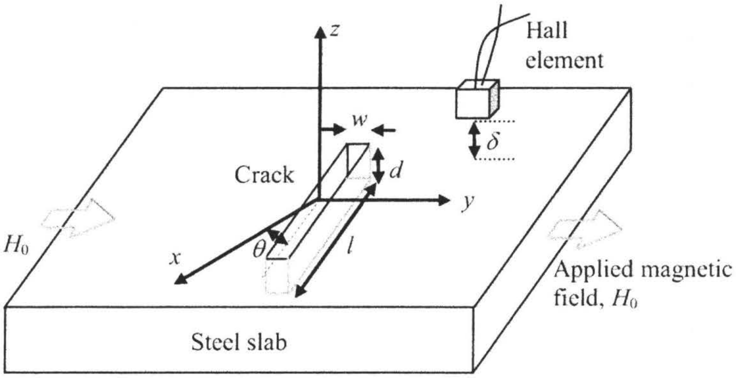

Fig. 5.1. Illustration of the MFL technique.

In this section, we propose a direct methodology to estimate the crack parameters only from the measured y-component (Fig. 5.1) of the magnetic leakage field in accordance with the available experimental setup. In order to achieve accurate estimation of the length and the depth, the orientation of the crack (θ in Fig. 5.1) is estimated first. Unlike the method presented in [25], where all three components of the magnetic field are used to estimate the orientation, our method uses only the y-component. Thus, our method implies much simpler measurement apparatus.

The proposed procedure consists of the following separate direct estimation steps, which must be carried out consecutively: 1) estimation of orientation, 2) estimation of length, and 3) estimation of depth (Fig. 5.2).

In the first step, the estimation of the orientation is based on the fact that the maximum MFL signal is always along the crack and its direction is across the crack mouth.

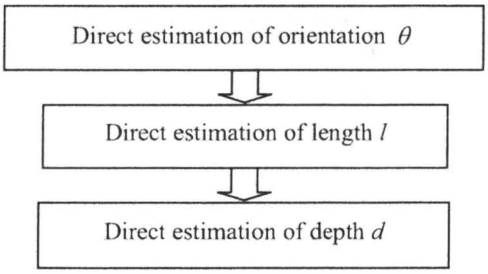

Fig. 5.2. Sizing procedure for surface breaking cracks using direct methods for estimation of orientation, length, and depth.

In the second step, we use the fact that the locations of the peaks in the first derivative of the MFL response along the crack mouth coincide approximately with the beginning and the ending of the crack. Having these locations, the estimation of the crack length is straightforward. Since this derivative approach is very sensitive to noise especially for near-orthogonal crack orientations where the signal-to-noise ratio (SNR) is small, we utilize a simple and robust wavelet de-noising algorithm applied to the derivative curves. Wavelet de-noising, especially with soft thresholding [26], has been widely employed with MFL signals [27]-[30] to eliminate high-frequency noise. Here, since we are only interested in the positions of the major peaks in the derivative, we set all the wavelet coefficients corresponding to high-frequency components to zero. This eliminates the ambiguous task of determining proper thresholds.

In the third step, in order to estimate the crack depth, we construct a calibration surface. This surface describes the maximum amplitude of the MFL signal at the crack as a function of the length and the depth of the crack. Once this surface is constructed, the length estimated in the previous step, together with the maximum amplitude of the associated MFL signal, are employed to extract the crack depth. It is worth noting that the calibration surface is constructed for cracks that are parallel to the x-axis. For other crack orientations, we propose an appropriate coefficient that adapts the calibration surface.

We examine the accuracy of the proposed method via simulations based on the FEM as well as available experimental MFL data.

5.2.1 Simulation of MFL Response Using FEM

A common type of MFL NDT uses permanent magnetic fields induced by powerful magnets which come in close contact with the imaged steel slab [31]. Maxwell's equations in a nonlinear permanent magnet system lead to [32]:

$$\nabla \times \nabla \times \mathbf{A} = \mu_0 (\mathbf{J} + \nabla \times \mathbf{M}) \tag{5.1}$$

where μ_0, **J** and **A** are the magnetic permeability of vacuum, the current density and the magnetic vector potential, respectively. The magnetization **M** is a non-linear function of $\mathbf{B} = \nabla \times \mathbf{A}$. Therefore, equation (5.1) is solved iteratively.

A nonlinear structural FEM solver (Maxwell v. 11.1.1 [33]) is used for simulating the three-dimensional (3-D) magnetic field around and inside a surface crack in a steel slab. Fig. 5.3 shows the model geometry. Steel_1010 is selected from the simulator's library as the material type for the steel slab.

In order to decrease the computational time and still maintain good accuracy, the steel slab is magnetized using two parallel magnets as shown in Fig. 5.3. Such a magnetizing setup is much simpler than the real magnetizer [31] but it meets the purpose of inducing parallel field lines along the y axis. NDFe35 is selected as the magnet material. It magnetizes the steel plate with a coercivity such that the operating point is in the knee area of the B-H curve for Steel_1010. This is desirable because it leads to the maximum SNR for obtaining the leakage crack signal [32].

We note that the FEM simulations do not match the absolute values of the magnetic field distribution obtained through measurements. However, they match reasonably well the normalized field distributions.

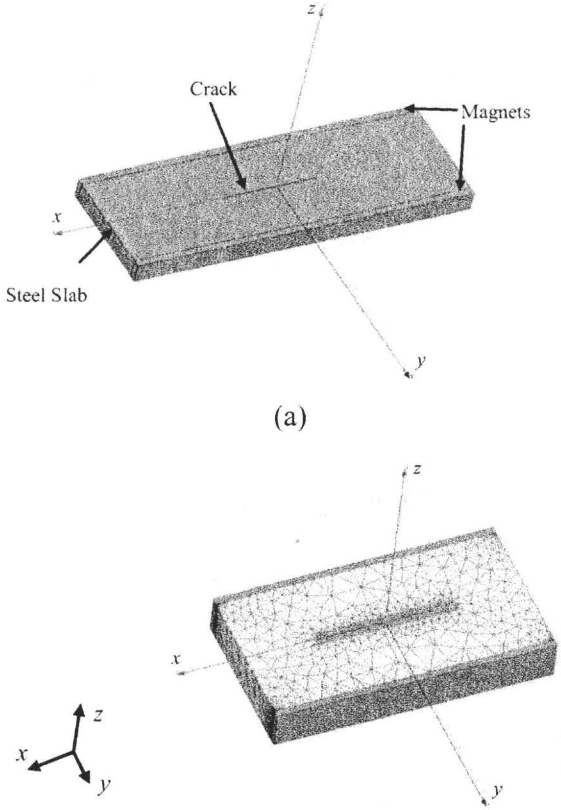

(a)

(b)

Fig. 5.3. 3-D view of the simulated model in Maxwell v. 11.1.1: (a) structure, (b) FEM mesh on the surface of the metal slab with enforced refinement of elements in the region around the crack.

Some additional boundary conditions are set to enforce the magnetic field inside the metal to be parallel to the *y*-axis. These boundary conditions are: (a) zero normal component of the magnetic field to all faces of the magnetizers except the faces which are parallel to the *x*-*z* plane; (b) zero tangential components of the magnetic field at the faces of the magnetizers which are parallel to the *x*-*z* plane; (c) zero normal component of the magnetic field at the faces of the steel which are parallel to the *y*-*z* plane.

5.2.2 Direct Method for Estimation of Orientation

We assume that only the H_y field component can be measured. We integrate H_y along a line $L(\theta)$ which is within the imaged area and is titled at an angle θ with respect to the x-axis as (Fig. 5.4):

$$f(\theta) = \int_{L(\theta)} H_y dL . \tag{5.2}$$

We refer to $f(\theta)$ as the θ-line integral. We evaluate $f(\theta)$ for all angles $0 \leq \theta \leq 180^\circ$ ($\Delta\theta = 1^\circ$) and solve the optimization problem:

$$\theta^* = \arg \max_{\theta} f(\theta) . \tag{5.3}$$

The validity and the accuracy of our technique are tested with data acquired through simulations. This is because all available measurements are associated with nearly $\theta = 0^\circ$ orientations. Figs. 5.5(a) to 5.7(a) show the MFL signal distributions in the x-y plane monitored at a lift-off distance (δ in Fig. 5.1) of 3.5 mm above the metal surface for cracks with l = 25 mm, d = 2.2 mm, and actual orientations of $\bar{\theta} = 0^\circ$, 60°, and 85°. The noise in the simulations is of numerical nature and it is not representative of the noise level in the measurement system. However, noise is always present in the measurements as well. Its sources relate to physical factors such as surface roughness, magnitude of the magnetization vector, local degradation of the magnetic properties of steel, etc. Thus, it is important to investigate the influence of noise on the estimation of the crack orientation, especially in the case of cracks oriented along the magnetizing field H_0 because this is the case of vanishingly small leakage field. As we observe from Figs. 5.5(a) to 5.7(a), the SNR decreases with increasing $\bar{\theta}$ due to the decreasing leakage field.

It is also clear that the maximum of the H_y leakage field component follows the crack. This implies that the θ-line integral attains a maximum value when the line $L(\theta)$ tracks the crack mouth.

Figs. 5.5(b) to 5.7(b) show the variation of the corresponding θ-line integrals. As predicted, the angle at which the θ-line integral is maximum coincides with the actual orientation of the crack. The accuracy of the orientation estimation is practically independent of the crack length and depth and the results for other cracks are very similar to the ones shown in Figs. 5.5 to 5.7.

Table 5.1 summarizes the results of the estimation of the orientation θ^* for a range of actual orientations $\bar{\theta} = 0^\circ$ to 85°. We observe that the estimation errors are less than 9° when the actual orientation is in the range of $\bar{\theta} = 0^\circ$ to 70°. The estimation suffers larger errors (between 9° and 17°) when the actual orientation is in the range of $\bar{\theta} = 70^\circ$ to 80°. The estimation results are unreliable for actual orientations of more than 80°. It is clear that the accuracy of the estimated orientation decreases for larger angles $\bar{\theta}$. The reason is that the SNR of the MFL signal is the highest when the crack is perpendicular to the applied field H_0 ($\bar{\theta} = 0^\circ$) and it decreases as $\bar{\theta}$ tends to 90° due to the decreasing leakage field.

5.2.3 Direct Method for Estimation of Length

In order to estimate the crack length, we employ the directional derivative of the magnetic field along the crack. We use the estimated orientation of the crack in the previous step to monitor the MFL signal along the crack. The position of the peaks in this derivative gives a proper approximation of the start and end points of the crack.

This method can be applied directly to low-noise signals. However, since the derivative approach could be sensitive to noise in different measurement setups or different crack orientations, we propose a de-noising algorithm based on the wavelet decomposition to discern the desired major peaks in the derivatives from the spurious ones.

5.2.3.1 De-noising the Derivatives of MFL Response

Both simulated and experimental MFL responses may suffer from high-frequency noise such that their derivatives contain a large number of peaks, which are much sharper than the peaks of interest at the two ends of the crack. Therefore, we utilize wavelet de-noising [26]-[30] to reduce these spurious peaks. The derivative of the MFL response monitored along the crack is decomposed at level 3, using a Coiflet wavelet. After setting all the wavelet coefficients corresponding to the details to zero, we reconstruct the signal again. The reconstructed signal does not contain spurious peaks and possesses only a positive and a negative peak at the two ends of the crack.

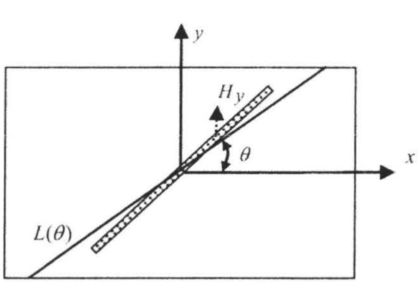

Fig. 5.4. Schematic of the θ-line integration of H_y along $L(\theta)$.

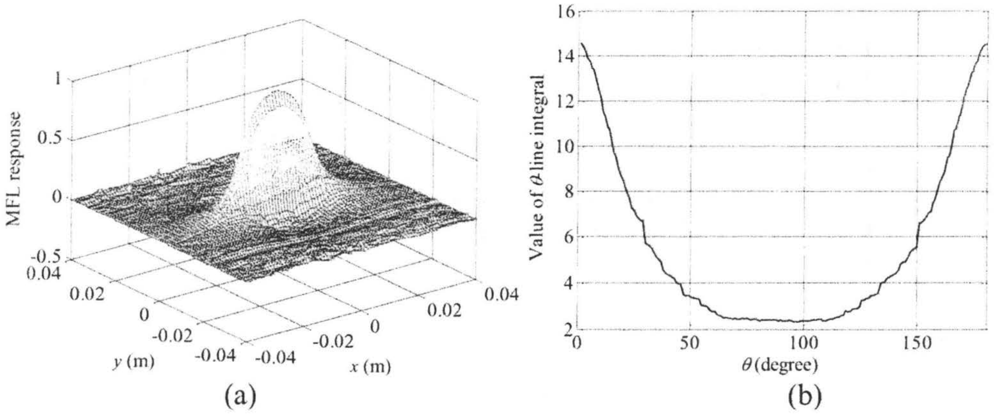

(a) (b)

Fig. 5.5. (a) Simulated 2-D MFL signal (normalized) for a crack with $l = 25$ mm, $d = 2.2$ mm, and $\theta = 0^\circ$, (b) the variation of the θ-line integral.

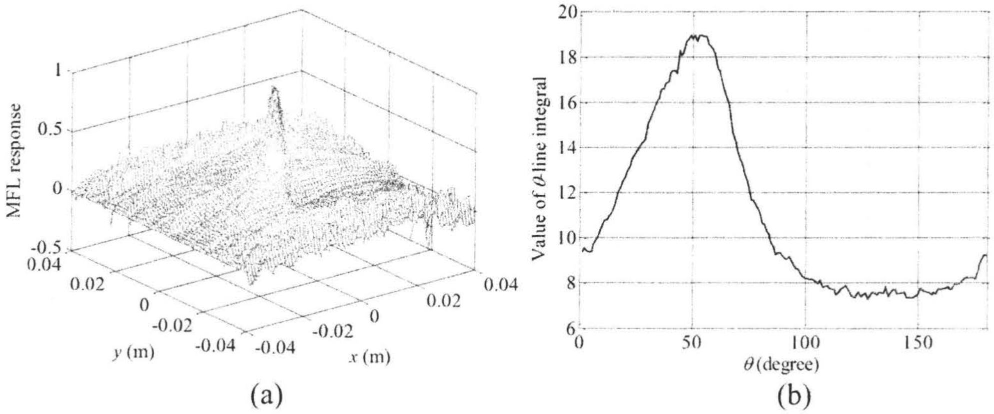

(a) (b)

Fig. 5.6. (a) Simulated 2-D MFL signal (normalized) for a crack with $l = 25$ mm, $d = 2.2$ mm, and $\theta = 60^\circ$, (b) the variation of the θ-line integral.

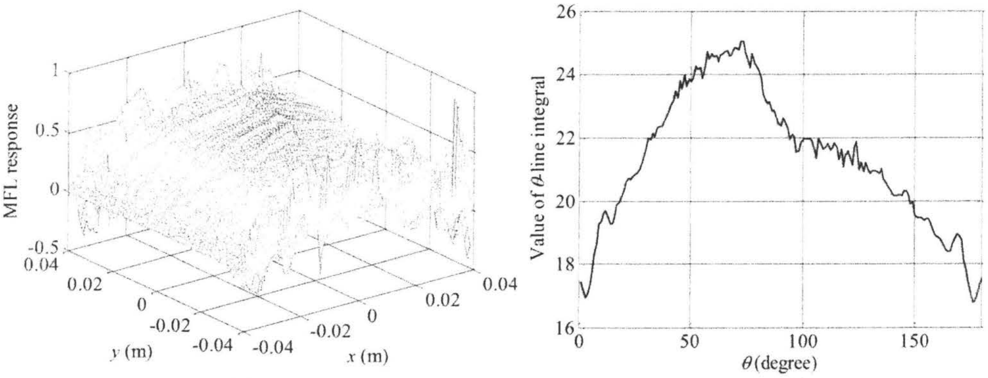

(a) (b)

Fig. 5.7. (a) Simulated 2-D MFL signal (normalized) for a crack with l = 25 mm, d = 2.2 mm, and $\theta = 85^\circ$, (b) the variation of the θ-line integral.

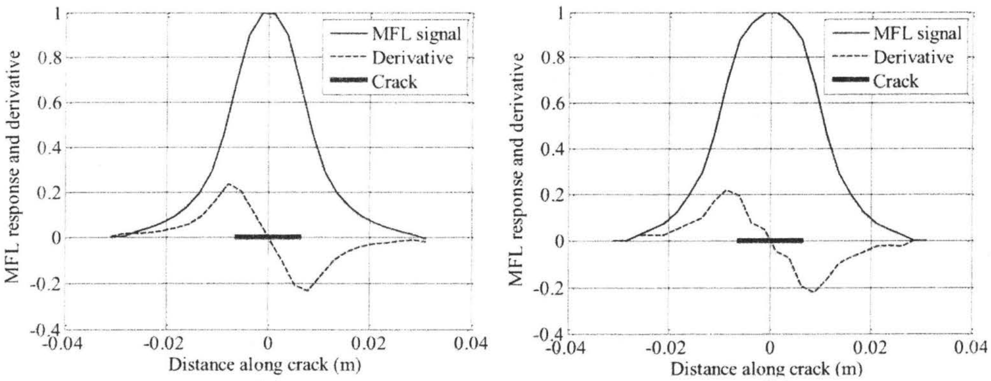

(a) (b)

Fig. 5.8. Normalized MFL response and its derivative for a crack with l = 13 mm, d = 2.2 mm, and $\theta = 0^\circ$: (a) simulation, (b) measurement.

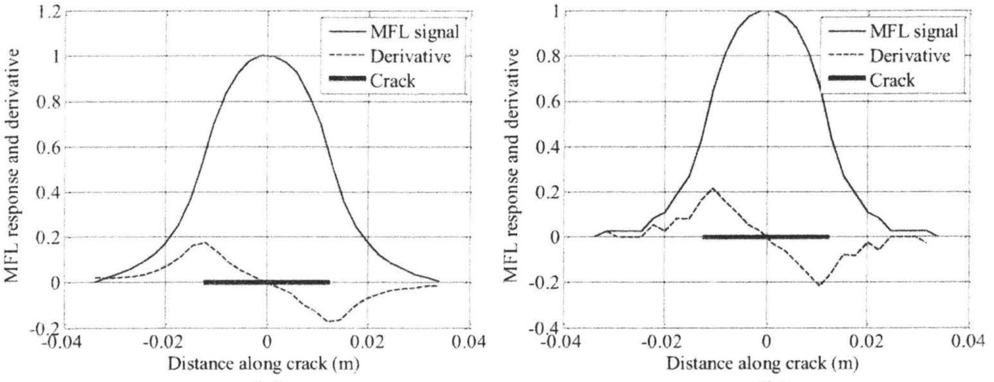

(a) (b)

Fig. 5.9. Normalized MFL response and its derivative for a crack with l = 25 mm, d = 2.2 mm, and $\theta = 0^\circ$: (a) simulation, (b) measurement.

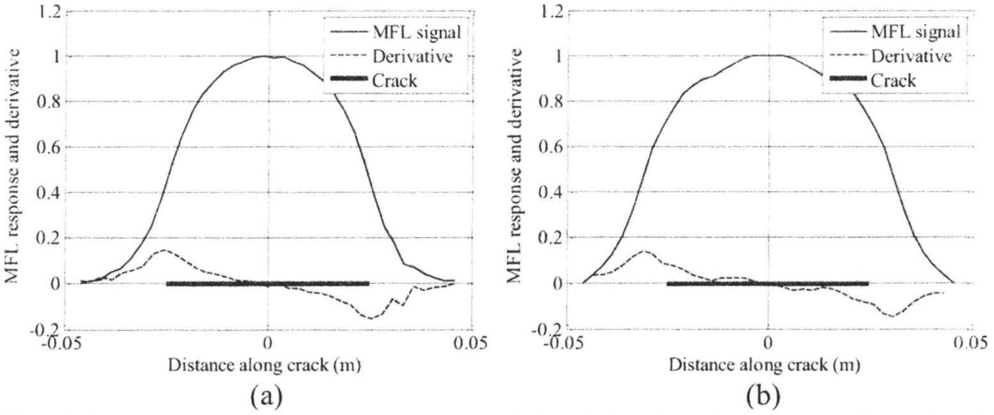

Fig. 5.10. Normalized MFL response and its derivative for a crack with l = 50 mm, d = 2.2 mm, and $\theta = 0^\circ$: (a) simulation, (b) measurement.

TABLE 5.1

ESTIMATION OF ORIENTATION FOR SIMULATED MFL SIGNALS FOR A CRACK WITH L = 25 MM AND D = 2.2 MM

Actual angle $\bar{\theta}$ (degree)	Estimated Angle θ^* (degree)
0	0
20	18
60	54
70	61
75	65
80	63
85	68

TABLE 5.2

ESTIMATION OF LENGTH USING DERIVATIVE APPROACH ($\bar{\theta} = 0^\circ$)

Crack parameters (mm)	Estimated length l^* (mm) with simulation	Estimated length l^* (mm) with measurement
d = 1.2 , l = 13	15.6	12.6
d = 2.2 , l = 13	15.4	16
d = 3.3 , l = 13	15.6	10.4
d = 1.2, l = 25	25.4	22
d = 2.2, l = 25	24.2	21
d = 3.3, l = 25	25.8	32
d = 1.2, l = 50	50.6	56
d = 2.2, l = 50	51	62
d = 3.3, l = 50	50	56

5.2.3.2 Results of the Length Estimation

Figs. 5.8 to 5.10 show the MFL responses and their corresponding derivatives for three measured cracks along the *x*-axis ($\bar{\theta} = 0^\circ$). Here, we should mention that the detection area of the Hall sensor is 3 mm × 4 mm. In general, the area of the Hall sensor affects the resolution ability of the measurement setup and it has some low-pass filtering effect on the MFL signal. Thus, we expect the largest errors in the length estimation to occur for the shortest cracks. Figs. 5.8 to 5.10 also show the same plots obtained from FEM simulations. Here, both the measured and the simulated MFL signals do not require de-noising because of the high SNR.

The small discontinuities in the derivatives are due to the spatial sampling rate of the measured signal which is 1.5 mm. We have monitored the simulated signals with the same sampling rate.

Table 5.2 summarizes the length estimation results for both simulations and measurements for some sample cracks. In both cases, the estimation errors are below 30 percent.

We investigate the robustness of the direct length estimation method for different crack orientations. Figs. 5.11 to 5.13 show the spatial derivative of the simulated MFL signals along the cracks with l = 25 mm, d = 2.2 mm, and actual orientations of $\bar{\theta} = 20^\circ$, 60°, and 80°. Here, we deal with noisy derivatives and employ the de-noising algorithm. Table 5.3 summarizes the results for the length estimation. These results show that length estimation could be achieved with good accuracy for orientations in the range from 0° to 75°. For orientations above 80°, the SNR is not large enough and the desired peaks in the derivative could not be discerned from the spurious ones. We next investigate the effect of the lift-off distance δ on the accuracy of the proposed length estimation method. Table 5.4 summarizes the results for length estimation with different lift-off distances. The results confirm the robustness of the length estimation method to variations of the lift-off distance.

5.2.4 Direct Method for Estimation of Depth

In order to estimate the crack depth directly, we use a calibration surface, which describes the maximum of the MFL response with respect to the length and depth of the crack. The maximum amplitude of the MFL response is considered after subtracting the background signal [34].

We construct this surface using measurement results for a sample set of 9 artificially manufactured cracks and defining four quadrant sub-surfaces. The calibration surface is then used to estimate the depth of all other measured cracks having their length estimated from the proposed method and the maximum amplitude of their MFL response.

Table 5.5 shows the parameters for the 9 cracks used to construct the calibration sub-surfaces with length and depth values of all combinations of l = 13, 25, 50 mm and d = 1.2, 2.2, 3.3 mm. Each sub-surface element is described by 4 cracks using linear inter/extrapolation. Table 5.6 shows the cracks that are used to define the sub-surfaces in each quadrant. The parameters of the corresponding four cracks are used to describe the sub-surface. We use the following 2-D inter/extrapolation formula to evaluate the sub-surface M at any l and d:

$$M(l,d) = A \cdot l + B \cdot d + C \cdot l \cdot d + D. \tag{5.4}$$

A, B, C, and D are constants which are determined from the system of four equations written for the four cracks defining the vertices of the sub-surface [35]. Fig. 5.14 shows the constructed normalized calibration surface for the 9 measured cracks.

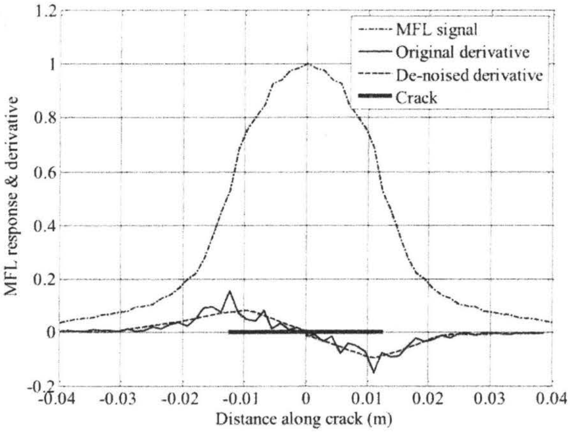

Fig. 5.11. Derivative of the simulated MFL signals (normalized) for a crack with l = 25 mm, d = 2.2 mm, and $\theta = 20^\circ$.

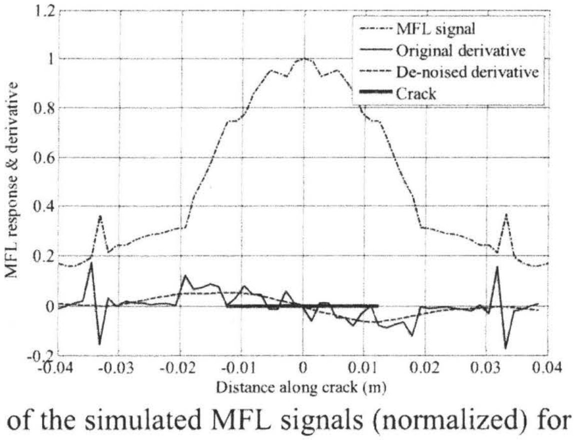

Fig. 5.12. Derivative of the simulated MFL signals (normalized) for a crack with l = 25 mm, d = 2.2 mm, and $\theta = 60^\circ$.

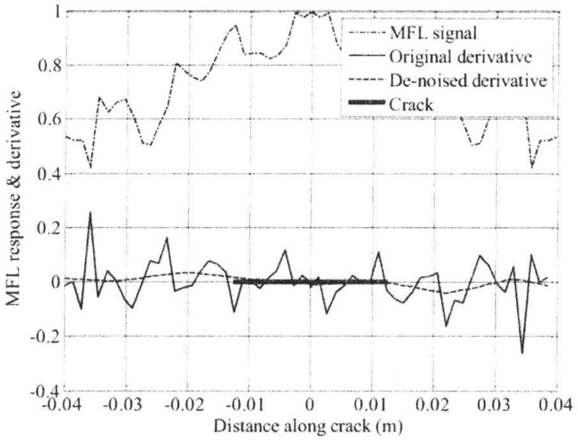

Fig. 5.13. Derivative of the simulated MFL signals (normalized) for a crack with $l = 25$ mm, $d = 2.2$ mm, and $\theta = 80^{\circ}$.

TABLE 5.3
ESTIMATION OF LENGTH FOR A CRACK WITH $L = 25$ MM, $D = 2.2$ MM, AND DIFFERENT ORIENTATIONS

Actual angle $\bar{\theta}$ (degree)	Estimated length l^{*} (mm)
0	28
20	28
60	28
70	28
75	28
80	---
85	---

TABLE 5.4
ESTIMATION OF LENGTH FOR A CRACK WITH $L = 25$ MM AND $D = 2.2$ MM SCANNED AT DIFFERENT LIFT-OFF DISTANCES

Lift-off distance δ (mm)	Estimated length l^{*} (mm)
0.5	28
1	28
2.5	28
4	27

Once we construct the calibration sub-surfaces, the length estimated from the previously discussed method together with the maximum of the measured signal is used to obtain an estimation of the depth for each newly measured crack. Generally, an optimization procedure can be employed for this purpose. However, formula (5.4) allows for a direct computation of the depth from the estimated length and the maximum of the MFL signal:

$$d^* = \frac{\hat{M} - A \cdot l^* - D}{B + C \cdot l^*} \tag{5.5}$$

where $\hat{M}$ is the maximum of the signal; l^* is the estimated crack length; and A, B, C, and D are the computed constants of the subsurface whose parameter region contains l^* and whose magnitude region contains $\hat{M}$.

5.2.4.1 Results for the Depth Estimation

Table 5.7 summarizes the results for the depth estimation of the same 9 measured cracks which were used to construct the calibration surface. Column 2 shows the results when the calibration surface employs all 9 cracks and thus consists of 4 surface elements. We observe that there are errors in the depth estimation despite the fact that the estimated cracks coincide with the nodes of the calibration surface. This is because the calibration surface is constructed using the known (true) length $\bar{l}$ and depth $\bar{d}$ of the cracks while the estimated depth d^* is obtained from the estimated length l^* where, generally, $l^* \neq \bar{l}$.

We investigated the extrapolation capability of the calibration surface by ignoring some of the available crack data and using these cracks as if they were newly measured cracks whose parameters fall outside of the range of the calibration surface. The highest errors occur in the case of cracks of depth $d = 1.2$ mm. This corresponds to extrapolation from known cracks with depths of 2.2 mm and 3.3 mm toward smaller crack depths for which we assume the data are not available. In this case, the highest estimation error is 70% for the crack with $l = 13$ mm and $d = 1.2$ mm. On the other hand, when we ignore calibration for larger depths, the estimation errors are still lower than 28%. Thus, our depth estimations are fairly accurate when extrapolating the calibration surface for deeper cracks. When we ignore calibration points of intermediate depths ($d = 2.2$ mm), the interpolation leads to depth estimation errors lower than 19%.

5.2.4.2 Correction of Calibration Surface at Different Crack Orientations

The calibration surface in Fig. 5.14 is provided for the case where the orientation of the crack is perpendicular to the external applied field ($\theta = 0^\circ$). However, when the crack has any other orientation, the amplitude of the MFL signal weakens and the provided calibration surface needs to be corrected. We propose a simple technique similar to [36] to take into account this change in amplitude. As Fig. 5.15 shows, when the crack has a non-zero orientation, the projection of the applied magnetic field H_0 on an axis perpendicular to the crack (y' in Fig. 5.15) is:

$$H_0' = H_0 \cos\theta . \tag{5.6}$$

TABLE 5.5
PARAMETERS OF THE MEASURED CRACKS

Crack No.	Length, *l* (mm)	Depth, *d* (mm)
Crack 1	13	1.2
Crack 2	13	2.2
Crack 3	13	3.3
Crack 4	25	1.2
Crack 5	25	2.2
Crack 6	25	3.3
Crack 7	50	1.2
Crack 8	50	2.2
Crack 9	50	3.3

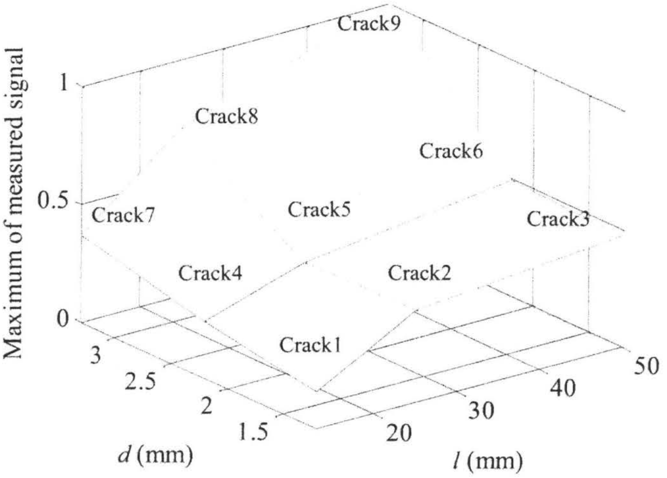

Fig. 5.14. Normalized calibration surface for the measured cracks.

TABLE 5.6
MEASURED CRACKS USED TO CONSTRUCT THE CALIBRATION SURFACE IN THE DESIRED REGIONS

Crack No. in Table 5.5	Parameter Region
1, 2, 4, 5	$l \leq 25$ mm , $d \leq 2.2$ mm
2, 3, 5, 6	$l \leq 25$ mm , $d \geq 2.2$ mm
5, 6, 8, 9	$l \geq 25$ mm , $d \geq 2.2$ mm
4, 5, 7, 8	$l \geq 25$ mm , $d \leq 2.2$ mm

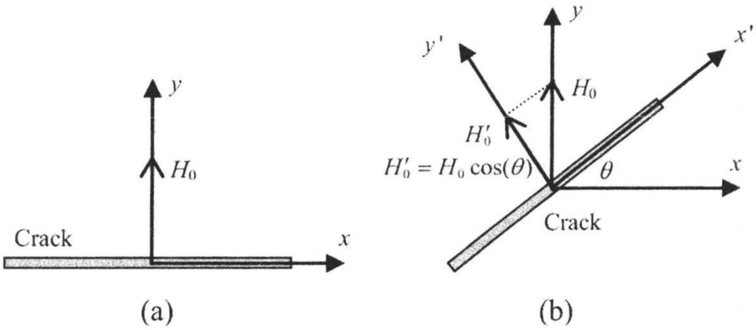

Fig. 5.15. (a) Crack with orientation of zero ($\theta = 0^\circ$); (b) illustration of finding the correction factor for a crack with non-zero orientation ($\theta \neq 0^\circ$).

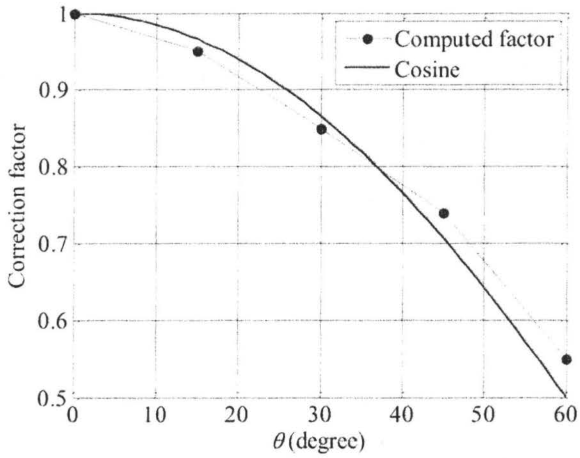

Fig. 5.16. Comparison of the correction factors computed from simulation of cracks with sample orientations with cosine values.

Thus, we can predict that the maximum amplitude of the crack signal changes with the same coefficient $\cos\theta$. Therefore, the calibration surface constructed for cracks with $\theta = 0^\circ$ is corrected using the factor $\cos\theta$. Fig. 5.16 shows the comparison of the correction factors computed from simulation of cracks with sample orientations and the $\cos\theta$ values.

TABLE 5.7
DEPTH ESTIMATION WHEN CALIBRATING WITH ALL CRACKS AND WHEN IGNORING CALIBRATION FOR SOME DEPTHS

Crack parameters (mm)	Calibration with all cracks		Ignoring calibration for d=1.2 mm		Ignoring calibration for d=2.2 mm		Ignoring calibration for d=3.3 mm	
	d^* (mm)	Error (%)	d^* (mm)	Error (%)	d^* (mm)	Error (%)	d^* (mm)	Error (%)
d=1.2, l=13	1.21	0.8	0.35	70	1.21	0.8	1.21	0.8
d=2.2, l=13	2.28	3	2.28	3.6	2.6	18.18	2.24	1.8
d=3.3, l=13	3.31	0.3	3.31	0.3	3.3	0	2.5	24
d=1.2, l=25	1.3	8	1.25	4.1	1.38	15	1.37	14.16
d=2.2, l=25	2.11	4	2.09	5	2.22	0.9	2.11	4
d=3.3, l=25	2.42	26	2.42	26.6	2.8	15	2.39	27.57
d=1.2, l=50	1.15	4.1	0.48	60	1.13	5.8	1.15	4.1
d=2.2, l=50	1.85	15	1.61	26.81	2.03	7.72	1.85	15.9
d=3.3, l=50	2.86	13	2.86	13.33	2.96	10.3	2.6	21.21

5.3 SPACE MAPPING OPTIMIZATION FOR DEFECT CHARACTERIZATION

The availability of the forward models based on FEM simulations [1]-[3] and the analytical formulas [4][7] prompts us to employ space mapping (SM) optimization in the defect parameter estimation from MFL data. SM exploits in an iterative manner two models: an expensive or "fine" model, which is very accurate but expensive or time-consuming, and the so called "coarse" model, which is less accurate but cheaper or faster to evaluate [37]-[40]. Provided that the misalignment between the fine and coarse model is not severe, SM-based algorithms typically provide excellent results after only a few evaluations of the fine model. They are far more efficient than the direct optimization of the fine model alone. The fine model data is utilized in the SM algorithm to update the coarse model iteratively during the optimization process and to create the so-called surrogate model. Thus, SM optimization allows us to benefit from the accuracy of the FEM simulations as a fine model and the speed of the analytical formulas as a coarse model. Based on this scheme, one can significantly reduce the CPU time necessary to characterize the defect parameters.

Here, defect characterization using SM-based optimization is performed for two common types of defects in pipelines–rectangular and cylindrical defects. The results of the parameter estimation for some sample defects demonstrate the efficiency of the SM-based optimization as a reliable and fast inversion method, especially in comparison with classical methods performing direct optimization of the FEM model.

Fig. 5.17(a) shows the MFL setup for the detection and evaluation of a rectangular crack with length l, width w, and depth d. Fig. 5.17(b) shows a similar illustration of a cylindrical defect with radius R and depth D. In this work, we monitor the y-component of the magnetic field as the MFL response.

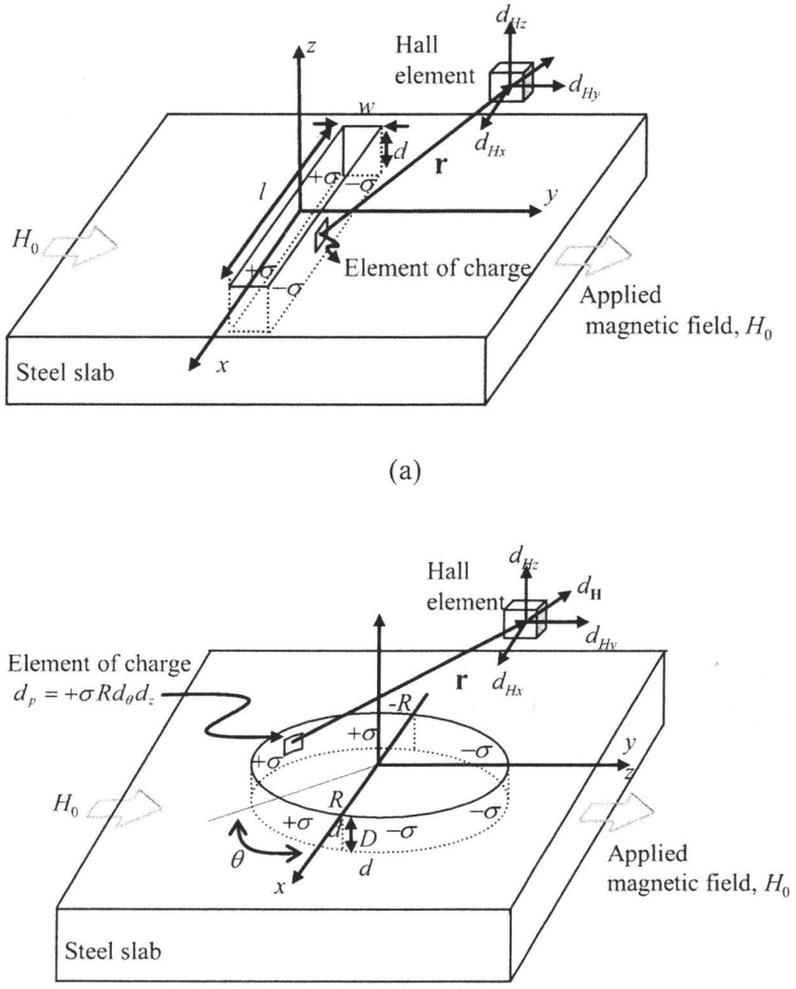

(a)

(b)

Fig. 5.17. Dipolar representation of defect: (a) rectangular, (b) cylindrical.

5.3.1 Analytical Models to Predict MFL Response

In all analytical expressions for the MFL signal [4]-[7], it is assumed that the crack is filled with homogeneously distributed magnetic dipoles, i.e., that the surface density of the magnetic charge has a constant value along the crack walls.

Edwards and Palmer [4] presented analytical solutions for the leakage field of a surface-breaking crack as a function of the applied magnetic field strength, the permeability and the crack dimensions. Also, they approximated the MFL response for a semi-elliptical surface-breaking cavity by an equivalent rectangular slot with constant polarity σ_s, positive poles on one face ($\sigma_s = +\sigma$) and negative poles on the other ($\sigma_s = -\sigma$). Then, the differential charge element d_p in a position (x, y, z) possesses a charge proportional to its area [4]

$$d_p = \sigma_s d_x d_z \, . \tag{5.7}$$

The magnetic field $\mathbf{H}$ is calculated at all observation points by integrating the magnetic field due to all charge elements d_p:

$$\mathbf{H} = \iint\limits_{(x,z)\in S} \frac{d_p}{4\pi r^3} \cdot \mathbf{r} \tag{5.8}$$

where S is the cylindrical surface of the crack wall and $\mathbf{r}$ is the distance vector from the point of integration to the point of observation.

Similar to the previous analytical expressions for surface-breaking cracks, a dipolar magnetic charge model has been developed for cylindrical pit defects [5]. As shown in Fig. 5.17(b), half of the cylinder wall develops positive magnetic charge density $+\sigma$ while the other half has negative charge density $-\sigma$. The angle θ is measured from the positive x-axis to an element of magnetic charge d_p. The differential element d_p has coordinates $(R\cos\theta,\ R\sin\theta,\ z)$ and a charge proportional to its area,

$$d_p = \sigma R d_\theta d_z . \tag{5.9}$$

The magnetic field **H** is calculated using the same integral as in (5.8) but over a cylindrical wall *S*.

It has been shown that the simplifying assumptions made in deriving the analytical expressions, especially neglecting the local variations in the magnetization and the permeability around the crack mouth, lead to errors in calculating the leakage field. This indicates that the distribution of the magnetic dipoles σ along the crack depth are in fact not constant [5][7].

5.3.2 Space Mapping Optimization

Space mapping is a recognized engineering optimization methodology that encompasses a number of efficient approaches [37]-[40]. The main idea behind SM is that the direct optimization of an accurate but computationally expensive high fidelity or "fine" model of interest is replaced by the iterative optimization and updating of a so-called "coarse" model (less accurate but much cheaper to evaluate). An example of a fine model would be a device analyzed using an electromagnetic simulator; the coarse model might be a circuit equivalent of the device analyzed with a conventional circuit simulator. Provided that the misalignment between the fine and coarse models is not significant, SM-based algorithms typically provide excellent results after only a few evaluations of the fine model. In contrast, direct optimization typically requires dozens or hundreds of evaluations and often fails to provide acceptable results.

Let $\boldsymbol{R}_f : X_f \rightarrow R^m$ denote the response vector of the fine model of a given device, where $X_f \subseteq R^n$. Our goal is to solve

$$x_f^* = \arg\min_{x \in X_f} U(\boldsymbol{R}_f(x)) \tag{5.10}$$

where $U : R^m \rightarrow R$ is a given objective function. In many engineering problems, we are concerned with the so-called minimax objective function: if we denote the fine model response components by $\boldsymbol{R}_f = [R_{f.1} \ \ldots \ R_{f.m}]^T$, the lower specification vector by $\boldsymbol{R}_l = [R_{l.1} \ \ldots \ R_{l.m}]^T$, and the upper specification vector by $\boldsymbol{R}_u = [R_{u.1} \ \ldots \ R_{u.m}]^T$, then we require that $R_{f.i} \leq R_{u.i}$ for $i \in I_u$ and $R_{f.i} \geq R_{l.i}$ for $i \in I_l$, where $I_l, I_u \subset \{1, 2, \ldots, m\}$. The minimax objective function is given by

$$U(\boldsymbol{R}_f) = \min\left\{\max_{i \in I_u}(R_{f.i} - R_{u.i}), \max_{i \in I_l}(R_{l.i} - R_{f.i})\right\}. \tag{5.11}$$

In some problems, U can be defined by a norm, i.e.,

$$U(\boldsymbol{R}_f) = \| \boldsymbol{R}_f - \boldsymbol{R}_{spec} \| \tag{5.12}$$

where $\boldsymbol{R}_{spec} = [R_{spec.1} \ \ldots \ R_{spec.m}]^T$ is the target response.

We consider the fine model to be expensive to compute and solving (5.10) by direct optimization to be impractical. Instead, we use surrogate models, i.e., models that are supposed to be good local representations of the fine model and computationally cheap, hence suitable for iterative optimization. According to the SM approach, the surrogate is built based on the coarse model as well as some auxiliary mappings. The mapping parameters are adjusted during the so-called parameter extraction process in order to reduce misalignment between the fine model and the surrogate. The process of updating the surrogate model is performed iteratively using the fine model data accumulated during the optimization process. We consider an optimization algorithm that generates a sequence of points $x^{(i)}$, $i = 0, 1, 2, \ldots$, and a family of surrogate models $\boldsymbol{R}_s^{(i)}$, so that

$$\boldsymbol{x}^{(i+1)} = \arg\min_{\boldsymbol{x}} U(\boldsymbol{R}_s^{(i)}(\boldsymbol{x})). \tag{5.13}$$

Let $\boldsymbol{R}_c : X_f \rightarrow R^m$ denote the response vector of the coarse model that describes the same object as the fine model but is less accurate and much faster to evaluate. Let $\overline{\boldsymbol{R}}_s$ be a generic SM surrogate model, i.e., the coarse model composed with suitable SM transformations. At iteration i, the surrogate model $\boldsymbol{R}_s^{(i)}$ is defined as

$$\boldsymbol{R}_s^{(i)}(\boldsymbol{x}) = \overline{\boldsymbol{R}}_s(\boldsymbol{x}, \boldsymbol{p}^{(i)}) \tag{5.14}$$

where

$$\boldsymbol{p}^{(i)} = \arg\min_{\boldsymbol{p}} \sum\nolimits_{k=0}^{i} w_{i.k} \, \| \boldsymbol{R}_f(\boldsymbol{x}^{(k)}) - \overline{\boldsymbol{R}}_s(\boldsymbol{x}^{(k)}, \boldsymbol{p}) \| \tag{5.15}$$

is a vector of model parameters and $w_{i.k}$ are weighting factors. Typically, we put $w_{i.k} = 1$ for all i and k.

A variety of SM surrogate models is available [40][41]. One of the most popular approaches is the so-called input SM [37], in which the generic SM surrogate model takes the form $\overline{\boldsymbol{R}}_s(\boldsymbol{x}, \boldsymbol{p}) = \overline{\boldsymbol{R}}_s(\boldsymbol{x}, \boldsymbol{B}, \boldsymbol{c}) = \boldsymbol{R}_c(\boldsymbol{B} \cdot \boldsymbol{x} + \boldsymbol{c})$. Another popular approach is the so-called output SM where the surrogate model is defined as $\overline{\boldsymbol{R}}_s(\boldsymbol{x}, \boldsymbol{p}) = \overline{\boldsymbol{R}}_s(\boldsymbol{x}, \boldsymbol{d}) = \boldsymbol{R}_c(\boldsymbol{x}) + \boldsymbol{d}$, where $\boldsymbol{d}$ is a correction term accounting for the difference between the fine and coarse model responses at iteration i, so that

$\boldsymbol{d}^{(i)} = \boldsymbol{R}_f(\boldsymbol{x}^{(i)}) - \boldsymbol{R}_c(\boldsymbol{x}^{(i)})$. In other words, this output SM ensures zero-order consistency between the fine model and the surrogate [42]. In practice, basic mappings are often combined together in order to create more involved surrogate models. Fig. 5.18 illustrates the combination of the input and output space mapping approaches.

The choice of SM surrogate type is normally problem dependent. Some methods of assessing the surrogate model as well as the techniques for automatic selection of the surrogate model for a given optimization problem can be found in [43][44]. In many cases, including this paper, a suitable model can be found using the following approach: (i) start with the simplest model (e.g., shift-based input space mapping with $\boldsymbol{c}$ being the only parameter, (ii) perform parameter extraction, (iii) check the matching between the surrogate and the fine model, (iv) if the matching is not sufficient (which can be examined visually by observing model responses), add degrees of freedom and go back to (ii). The model verification may be performed at the starting point so that no extra fine model evaluations are necessary. Also, over-flexibility of the surrogate model should be avoided because it normally degrades its generalization capabilities [44].

Typically, the starting point $\boldsymbol{x}^{(0)}$ of the SM optimization algorithm is a coarse model optimal solution, i.e., $\boldsymbol{x}^{(0)} = \arg\min\{\boldsymbol{x} : U(\boldsymbol{R}_c(\boldsymbol{x}))\}$.

The SM optimization algorithm flow can be described as follows:

Step 1 Choose the proper coarse model as well as space mapping surrogate type. Set $i = 0$.

Step 2 Evaluate the fine model to find $\boldsymbol{R}_f(\boldsymbol{x}^{(i)})$.

Step 3 Obtain the surrogate model $\boldsymbol{R}_s^{(i)}$ using (5.14) and (5.15).

Step 4 Given $\boldsymbol{x}^{(i)}$ and $\boldsymbol{R}_s^{(i)}$, obtain $\boldsymbol{x}^{(i+1)}$ using (5.13).

Step 5 If the termination condition is not satisfied go to Step 2; else, terminate the algorithm.

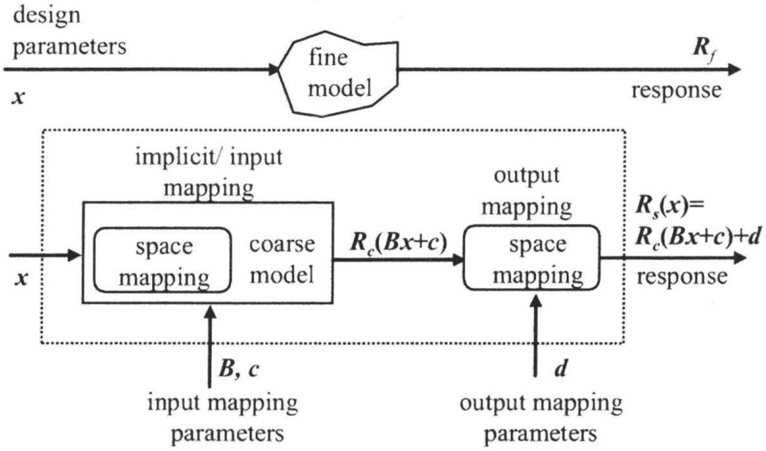

Fig. 5.18. Fine model and the space mapping surrogate based on input and output SM.

Step 3 is the parameter extraction and it plays a crucial role in establishing the surrogate model. Usually, the algorithm is terminated when convergence is obtained or when the user-defined maximum number of iterations is exceeded.

5.3.3 Inversion Procedure Based on SM Optimization

In this work, we estimate the shape parameters of rectangular and cylindrical defects using SM-based optimization. In case of crack-like rectangular defects, we assume that the width of the crack is very small compared to its length and depth such that the variation of the MFL signal with the width is negligible.

Therefore, the inversion problem is a two-variable optimization problem for the length l and the depth d, i.e., $\boldsymbol{x} = [l\ d]^T$. In the case of cylindrical defects, the parameters of interest are the radius R and the depth D. The inversion problem is again a two-variable optimization problem, i.e., $\boldsymbol{x} = [R\ D]^T$. Fig. 5.19 illustrates the flowchart of the SM-based optimization for estimating the parameters of interest. FEM simulations serve as the fine models and the analytical formulas given by (5.7)-(5.9) implemented in Matlab [45] serve as the coarse model. We use the SMF system [46][47] to perform the SM optimization.

The termination condition for the SM algorithm has the following form:

$$\frac{\left\|\boldsymbol{x}^{(i+1)} - \boldsymbol{x}^{(i)}\right\|}{\left\|\boldsymbol{x}^{(i)}\right\|} < \delta \tag{5.16}$$

where $\|\cdot\|$ is the l_2-norm, $\boldsymbol{x}^{(i)}$, $i = 0, 1, \ldots$, is the sequence of solutions produced by the SM algorithm, and δ is a small user-defined constant.

5.3.4 Results of Defect Parameter Estimation Using SM Optimization

Results of various simulation tests are presented here to assess the accuracy and the computational efficiency of the proposed inversion technique based on SM optimization. For this purpose, two rectangular cracks and two cylindrical pits are examined. Tables 5.8 and 5.9 show the parameter values of these defects. The target MFL responses for all cases are the y-component distributions of the magnetic field monitored at a distance of 3.5 mm above the surface of the metal. These are produced using FEM simulations. We assume that the search regions for the parameter values are restricted within the following ranges: (a) for rectangular cracks, $5 \text{ mm} \leq l \leq 65 \text{ mm}$ and $0.1 \text{ mm} \leq d \leq 4.5 \text{ mm}$; and (b) for cylindrical pits, $0.5 \text{ mm} \leq R \leq 10 \text{ mm}$ and $0.5 \text{ mm} \leq D \leq 4.5 \text{ mm}$.

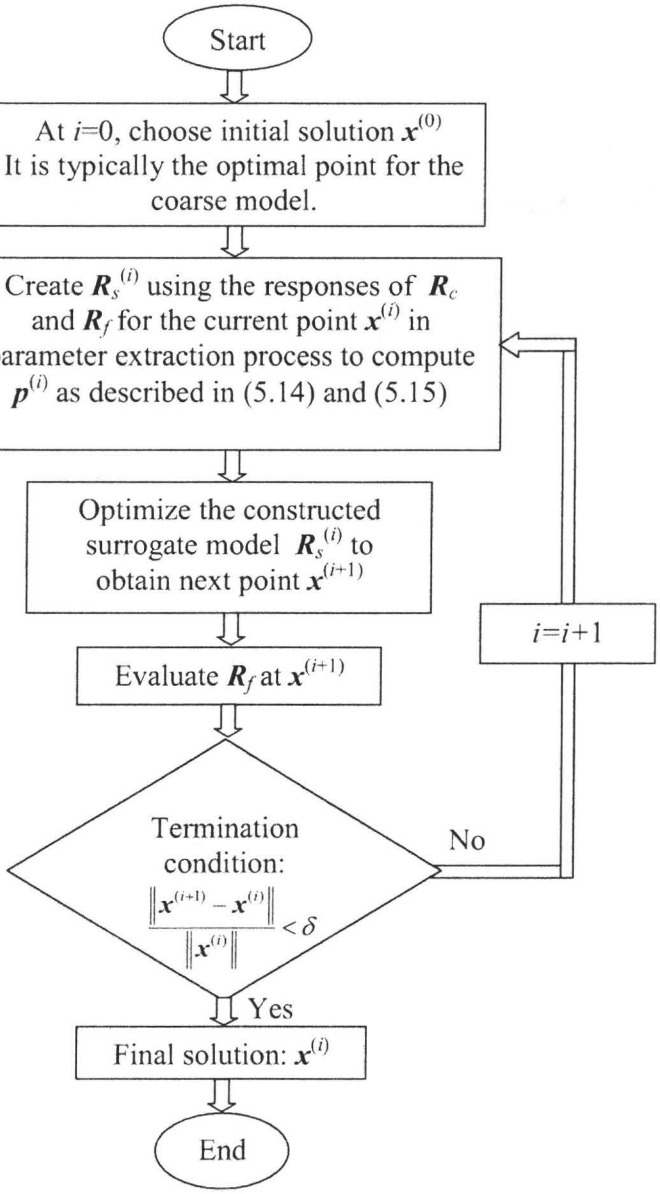

Fig. 5.19. Flowchart of space mapping optimization.

TABLE 5.8
LENGTH AND DEPTH FOR THE RECTANGULAR CRACKS

Crack name	Length, *l* (mm)	Depth, *d* (mm)
Crack1	15	2.5
Crack2	35	1.5

TABLE 5.9
RADIUS AND DEPTH FOR THE CYLINDRICAL PITS

Pit name	Radius, *R* (mm)	Depth, *D* (mm)
Pit1	3	4
Pit2	5	2

It should be noted that the performance of SM algorithms depends on the similarity between the fine model and the coarse model, which can be expressed in rigorous mathematical terms (e.g., [41]). Unfortunately, it is difficult to verify whether this similarity is sufficient or not for a given problem because of the lack of fine model data. Therefore, it is beneficial to ensure as good alignment between the coarse and fine models as much as possible beforehand. In our case, as the maximum amplitudes of the MFL distributions obtained from the coarse and the fine models are substantially different, we use a scaling surface to align them.

The surface describes the coefficient which multiplies the coarse model response to match the corresponding fine model response within the search region. We construct this surface using the coarse and fine model responses for a set of 5 sample defects and defining four quadrant sub-surfaces. These points are selected so that they roughly cover the whole 2-D parameter space of interest. Fig. 5.20 shows the construction of the scaling surface from 4 quadrant sub-surfaces

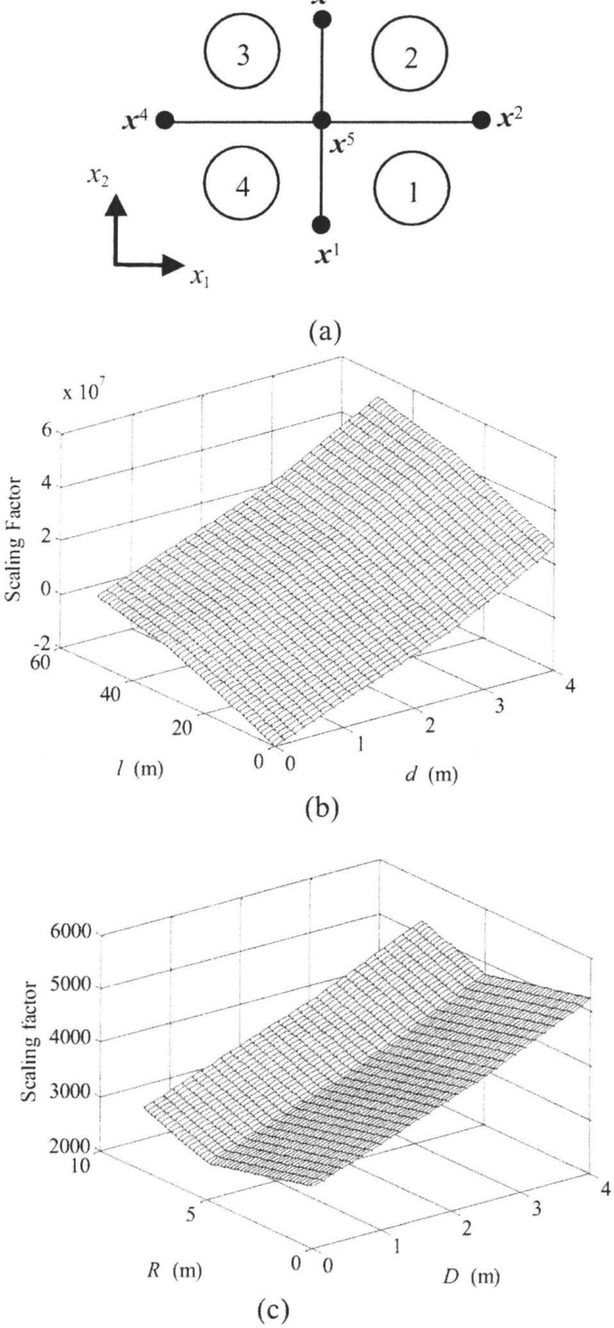

Fig. 5.20. (a) Constructing the scaling surface from four quadrant surfaces and 5 points (defects). (b) Illustration of scaling surface for rectangular cracks. (c) Illustration of scaling surface for cylindrical pits.

TABLE 5.10
CRACKS (POINTS) USED TO DEFINE 4 SUB-SURFACES IN FIG. 5.20.

Region No	Defect vertex No.	Parameter Region
1	1, 2, 5	$x_1 \geq \boldsymbol{x}_1^1, x_2 \leq \boldsymbol{x}_2^2$
2	2, 3, 5	$x_1 \geq \boldsymbol{x}_1^1, x_2 \geq \boldsymbol{x}_2^2$
3	3, 4, 5	$x_1 \leq \boldsymbol{x}_1^1, x_2 \geq \boldsymbol{x}_2^2$
4	1, 4, 5	$x_1 \leq \boldsymbol{x}_1^1, x_2 \leq \boldsymbol{x}_2^2$

(1, 2, 3, and 4) defined by 5 defects (points), $\boldsymbol{x}^1$, $\boldsymbol{x}^2$, $\boldsymbol{x}^3$, $\boldsymbol{x}^4$, and $\boldsymbol{x}^5$. Each sub-surface is defined by 3 points and linear interpolation/extrapolation formula. Table 5.10 shows the cracks that are used to define the 4 sub-surfaces in Fig. 5.20. We use the following 2-D inter/extrapolation formula to evaluate the sub-surface M at any $\boldsymbol{x}$:

$$M(x_1, x_2) = A \cdot x_1 + B \cdot x_2 + C \tag{5.17}$$

where A, B, and C are constants computed using the corresponding 3 points defining this sub-surface. For rectangular cracks, the following points (cracks) are used to construct the scaling surface: $\boldsymbol{x}^1 = [30\ 1]^T$, $\boldsymbol{x}^2 = [50\ 2.5]^T$, $\boldsymbol{x}^3 = [30\ 4]^T$, $\boldsymbol{x}^4 = [10\ 2.5]^T$, and $\boldsymbol{x}^5 = [30\ 2.5]^T$. The sample points in the case of cylindrical pits are: $\boldsymbol{x}^1 = [5\ 1]^T$, $\boldsymbol{x}^2 = [8\ 2.5]^T$, $\boldsymbol{x}^3 = [5\ 4]^T$, $\boldsymbol{x}^4 = [2\ 2.5]^T$, and $\boldsymbol{x}^5 = [5\ 2.5]^T$. Figs. 5.20 (b) and (c) illustrate the constructed scaling surfaces based on the mentioned points for two types of defects. Once we have the scaling surface $M(\boldsymbol{x})$, we use the scaling factor at each $\boldsymbol{x}$ to adjust the level of the coarse model response to that of the fine model. It should be noted that the described scaling method has been chosen as a trade-off between the accuracy of the scaling and the computational cost of extra fine model evaluations required to implement the scaling. More accurate scaling (e.g., with a quadratic regression model) would require more fine model data, whereas 5 points together with a piece-wise linear approximation is sufficient for our purposes. The location of the points is not critical.

We mention that the local alignment between the fine model and the surrogate can also be ensured using an output SM as explained in Section 5.3.2. Unfortunately, when the scaling surfaces are left out and the output SM is used instead, the algorithm is not able to find satisfactory solutions. The reason is that the output SM surrogate "transfers" the residual (i.e., the difference between the fine and coarse model at the current iteration point) to the new surrogate model optimum, which may be misleading if the overall alignment between the fine and coarse models is too poor, as is the case when the scaling surfaces are not used.

Prior to starting the SM optimization, the optimal solution of the corresponding coarse model is computed. In particular, the coarse models are directly optimized using the sequential quadratic programming (SQP) method in Matlab's optimization toolbox. We examined the optimal points, $\boldsymbol{x}_c^*$, obtained from direct optimizations of the coarse models when starting from different initial points. The results demonstrated that the optimization algorithms converge to unique solutions for all investigated defects which are $[17.38\ 3.53]^T$, $[34.2\ 2.46]^T$, $[4.28\ \ 2.50]^T$, and $[6.07\ 1.70]^T$ for Crack1, Crack2, Pit1, and Pit2, respectively. A quantitative comparison of the inversion results from the direct optimization of the coarse model is given in Table 5.11, where the mean relative error (MRE) is defined as:

$$\mathrm{MRE}(\hat{x}) = \frac{1}{2}\left(\frac{|x_2 - \hat{x}_2|}{x_2} + \frac{|x_1 - \hat{x}_1|}{x_1}\right) \times 100. \tag{5.18}$$

Here, $\boldsymbol{x}$ and $\hat{\boldsymbol{x}}$ denote the actual and solution points, respectively.

The SM optimization is performed using the input SM surrogate model of the form $\bar{\boldsymbol{R}}_s(\boldsymbol{x}, \boldsymbol{p}) = \boldsymbol{R}_s(\boldsymbol{x}, \boldsymbol{c}) = \boldsymbol{R}_c(\boldsymbol{x} + \boldsymbol{c})$ with the vector $\boldsymbol{c}$ obtained through the parameter extraction process (5.15). This particular model has been chosen because it provides sufficient matching with the fine model; Thus, there is no need to exploit more involved models. We use the termination condition (5.16) with δ equal to 0.01.

Table 5.11 summarizes the optimization results. The SM initial points, which are the optimal points of the coarse models, are denoted as $\boldsymbol{x}_c^*$. The table also shows the MRE for the coarse model (column 3) and the MRE for the fine model (last column). It is observed that the SM optimization converges to the solution after few fine model evaluations. The solutions for Crack1, Crack2, Pit1, and Pit2 are $[15.13\ \ 2.48]^T$, $[35.11\ \ 1.53]^T$, $[3.09\ \ 3.73]^T$, and $[5.01\ \ 1.99]^T$, which show MRE values of 0.8, 1.1, 6, and 1.2, respectively, when compared to the actual parameter values. These errors demonstrate significant improvement in the parameter estimation when compared with the MRE values obtained from the coarse model optimal points.

Fig. 5.22 compares the target MFL responses with the MFL responses obtained at the optimal points of the coarse models, i.e. $\boldsymbol{x}_c^*$, and the MFL responses obtained at the SM optimal points, i.e. $\bar{x}_f$, for all investigated defects.

In order to confirm the efficiency of the SM optimization in getting fast and accurate results, it is compared with direct optimization of the fine model. We choose $[30\ 3]^T$ and $[4\ 2.5]^T$ as the initial points for Crack1 and Pit1, respectively. The solutions via direct optimization of the fine model using SQP converges after

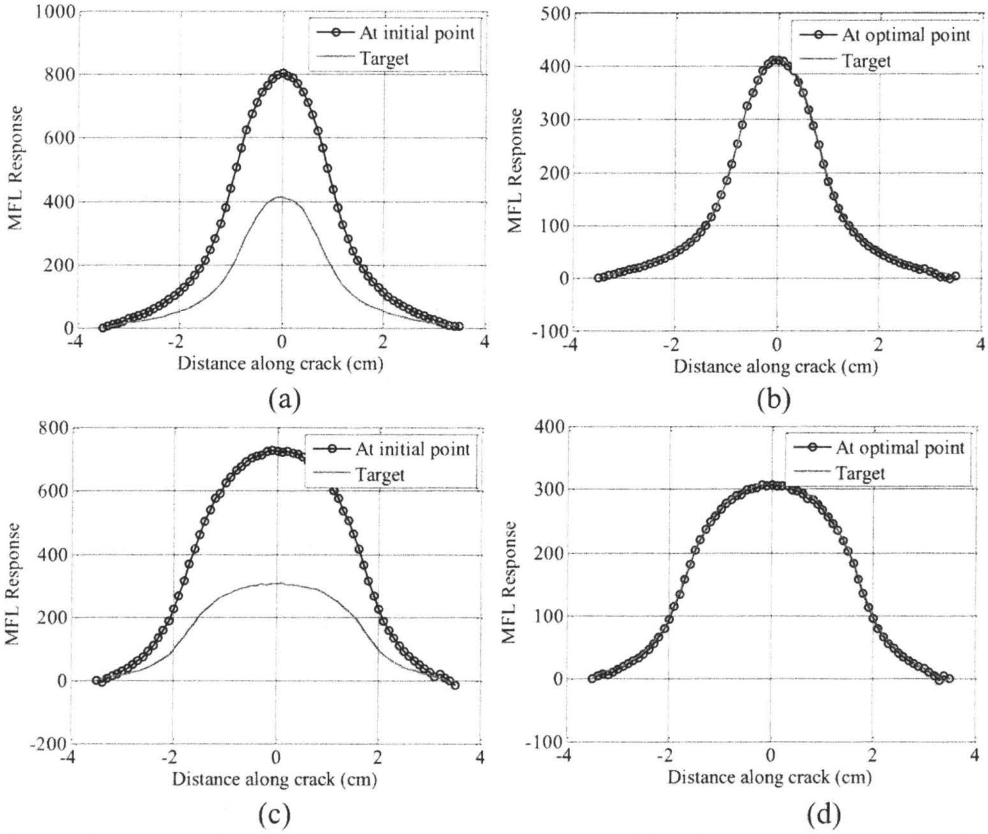

Fig. 5.21. Comparison of the target MFL response with MFL response obtained at the initial point x_c^*, i.e. coarse model optimal point, for: (a) Crack1, c) Crack2; and comparison of the target MFL response with MFL response obtained at the SM optimal point $\bar{x}_f$ for: (b) Crack1, (d) Crack2.

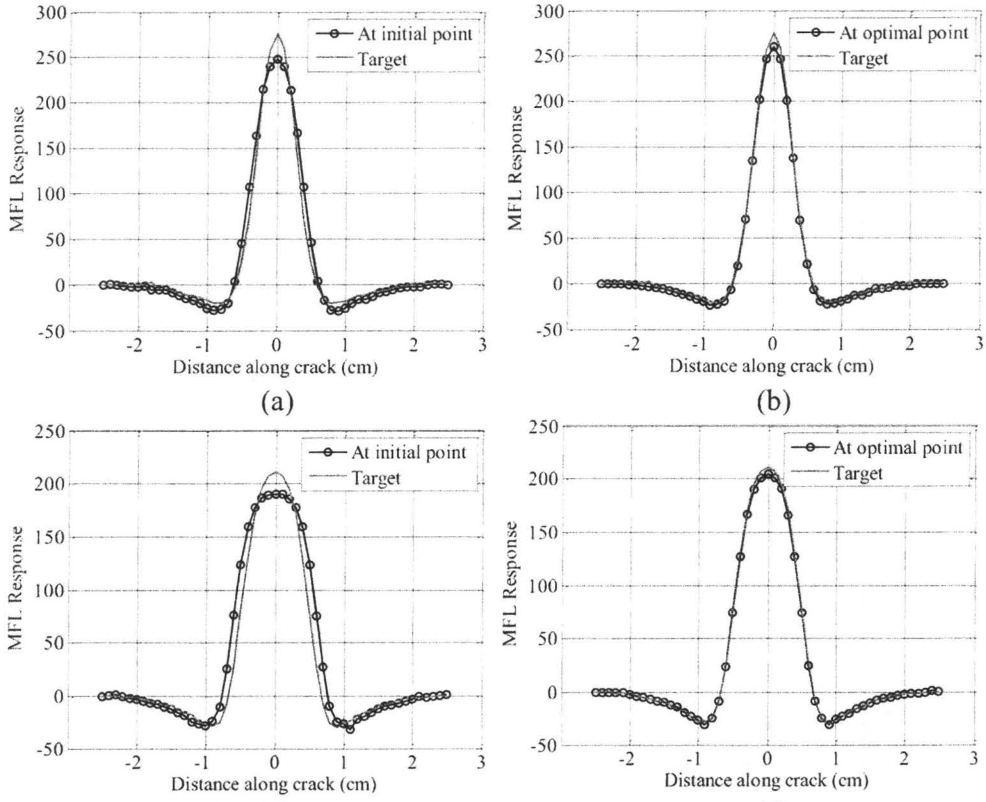

(a) (b) (c) (d)

Fig. 5.22. Comparison of the target MFL response with MFL response obtained at the initial point x_c^*, i.e. coarse model optimal point, for: (a) Pit1, (c) Pit2; and comparison of the target MFL response with MFL response obtained at the SM optimal point $\bar{x}_f$ for: (b) Pit1, (d) Pit2.

43 and 39 fine model evaluations for Crack1 and Pit1, respectively. The solutions found with the termination condition of (5.16) with $\delta = 0.01$ are $[25.9\ 1.65]^T$ and $[4.29\ 2.66]^T$, respectively. The corresponding values of MRE are 53 and 38, respectively. These large errors demonstrate that the direct optimization is trapped in local minima in both cases, which are not the best solutions available. In contrast, SM optimization actually converges to the true solutions with the final

result being of much smaller MRE. Also, these results indicate that the direct optimization of the fine model is far more computationally expensive than the SM optimization.

TABLE 5.11
INVERSION RESULTS FOR SM OPTIMIZATION OF INVESTIGATED DEFECTS

Defect	Initial point ($\mathbf{x}_c^*$)	MRE for ($\mathbf{x}_c^*$)	No of SM Iterations	No of Fine Model Evaluations	Optimal point ($\bar{\mathbf{x}}_f$)	MRE for $\bar{\mathbf{x}}_f$
Crack1	$\begin{bmatrix} 17.38 \\ 3.53 \end{bmatrix}$	29	6	7	$\begin{bmatrix} 15.13 \\ 2.48 \end{bmatrix}$	0.8
Crack2	$\begin{bmatrix} 34.2 \\ 2.46 \end{bmatrix}$	33	6	7	$\begin{bmatrix} 35.11 \\ 1.53 \end{bmatrix}$	1.1
Pit1	$\begin{bmatrix} 4.13 \\ 2.62 \end{bmatrix}$	36	7	8	$\begin{bmatrix} 3.11 \\ 3.66 \end{bmatrix}$	6
Pit2	$\begin{bmatrix} 6.07 \\ 1.70 \end{bmatrix}$	18	3	4	$\begin{bmatrix} 5.00 \\ 1.95 \end{bmatrix}$	1.2

It should be noted that a single FEM simulation takes about 1 hour of CPU time and 1.2 GB of memory using a 3.2 GHz Pentium 4 processor. This means that the direct optimization of the fine model requires in excess of 40 hours of CPU time. The direct optimization of the coarse model is very fast and takes just a few seconds, however, the resulting solutions are not acceptable in terms of accuracy (typical MRE is about 30). Besides, 5 fine model evaluations (i.e., about 5 hours of the CPU time) are required to perform the coarse model scaling. On the other hand, SM optimization gives excellent results (typical MRE about 1) and requires only about 7 hours on average. This confirms that SM optimization is an efficient method of performing the inversion procedure in defect characterization.

5.4 SUMMARY

In this chapter, first we developed and validated a procedure to estimate surface breaking-crack parameters, i.e., orientation, length, and depth, from single-component magnetic field measurements. The procedure consists of the following consecutive steps: estimation of orientation, estimation of length, and estimation of depth. Then, we presented a SM optimization methodology to estimate defect parameters from MFL data. The proposed methodology was tested and verified for two common types of defects, rectangular cracks and cylindrical pits. The results demonstrated that there is a dramatic reduction in the number of fine model evaluations and therefore CPU time when using SM optimization instead of direct fine model optimization. Also, the results show that the proposed fast inversion technique features much improved accuracy, especially when compared to the results obtained using the analytical models.

REFERENCES

[1] R. Schifini and A. C. Bruno, "Experimental verification of a finite element model used in a magnetic flux leakage inverse problem," *J. Phys.D: Appl. Phys.*, vol. 38, no. 12, pp. 1875–1880, Jun. 2005.

[2] Z. Chen, G. Preda, O. Mihalache, and K. Miya, "Reconstruction of crack shapes from the MFLT signals by using a rapid forward solver and an optimization approach," *IEEE Trans. Magn.*, vol. 38, no. 2, pp. 1025–1028, Mar. 2002.

[3] M. Yan, S. Udpa, S. Mandayam, Y. Sun, P. Sacks, and W. Lord, "Solution of inverse problems in electromagnetic NDE using finite element methods," *IEEE Trans. Magn.*, vol. 34, no. 5,pp. 2924–2927, Sept. 1998.

[4] C. Edwards and S. B. Palmer, "The magnetic leakage field of surface-breaking cracks," *J. Phys. D: Appl. Phys.*, vol. 19, no. 4, pp 657–673, Apr. 1986.

[5] C. Mandache and L. Clapham, "A model for magnetic flux leakage signal predictions," *J. Phys. D: Appl. Phys.*, vol. 36, no. 20, pp. 2427–2431, Oct. 2003.

[6] D. Minkov, J. Lee, and T. Shoji, "Study of crack inversions utilizing dipole model of a crack and Hall element measurements," *J. Magn. Magn. Mater.*, vol. 217, no. 1, pp. 207–215, Jul. 2000.

[7] D. Minkov, Y. Takeda, T. Shoji, and J. Lee, "Estimating the sizes of surface cracks based on Hall element measurements of the leakage magnetic field and a dipole model of a crack," *J. Appl. Phys. A*, vol. 74, no. 2, pp. 169–176, Feb. 2002.

[8] P. Ramuhalli, L. Udpa, and S. S. Udpa, "Electromagnetic NDE signal inversion by function-approximation neural networks," *IEEE Trans. Magn.*, vol. 38, no. 6, pp. 3633–3642, Nov. 2002.

[9] W. Han and P. Que, "2D defect reconstruction from MFL signals by a genetic optimization algorithm," *Russian J. of NDT,* vol. 41, no. 12, pp. 809–814, Dec. 2005.

[10] W. Han and P. Que, "Defect reconstruction of submarine oil pipeline from MFL signals using genetic simulated annealing algorithm," *J. Japan Petr. Inst.*, vol. 49, no. 3, pp. 145–150, 2006.

[11] P. Ramuhalli, L. Udpa, and S. S. Udpa, "Neural network-based inversion algorithms in magnetic flux leakage nondestructive evaluation," *J. Appl. Phys.*, vol. 93, no. 10, pp. 8274–8276, May 2003.

[12] A. Joshi, L. Udpa, S. S. Udpa, and A. Tamburrino, "Adaptive wavelets for characterizing magnetic flux leakage signals from pipeline inspection," *IEEE Trans. Magn.*, vol. 42, no. 10, pp. 3168–3170, Oct. 2006.

[13] R. K. Amineh, N. K. Nikolova, J. P. Reilly, and J. R. Hare, "Characterization of surface breaking cracks using one tangential component of magnetic leakage field," *IEEE Trans. Magn.*, vol. 44, no. 4, pp. 516–524, Apr. 2008.

[14] R. K. Amineh, S. Koziel, N. K. Nikolova, J. W. Bandler, and J. P. Reilly, "A space mapping methodology for defect characterization from magnetic flux leakage measurements," *IEEE Trans. Magn.*, vol. 44, no. 8, pp. 2058–2065, Aug. 2008.

[15] R. K. Amineh, N. K. Nikolova, J. P. Reilly, and J. R. Hare, "Characterization of surface breaking cracks," *20th Int. Pipeline Pigging & Integrity Management Conf.*, USA 2008.

[16] R. K. Amineh, S. Koziel, N. K. Nikolova, J. W. Bandler, and J. P. Reilly, "A space mapping methodology for defect characterization," *24th Int.*

Review of Progress in Applied Computational Electromagnetics (ACES), Canada, 2008.

[17] N. K. Nikolova, D. Cronin, S. M. Pasha, R. K. Amineh, I. Smith, R. Thompson, and J. R. Hare, "Electrical resistance welded seam inspection using circumferential flux," *7th Int. Pipeline Conference (IPC)*, Canada, 2008.

[18] L. W. Tsay, Y. C. Chen, and S. L. I. Chan, "Sulfide stress corrosion cracking and fatigue crack growth of welded TMCP API 5L X65 pipe-line steel," *Int. J. Fatigue*, vol. 23, no. 2, pp. 103–113, Jan. 2001.

[19] W. Lord and J. H. Hwang, "Defect characterization from magnetic flux leakage fields," *British J. NDT*, vol. 19, no. 1, pp. 14–18, Jan. 1977.

[20] E. Altschuler and A. Pignotti, "Nonlinear model of flaw detection in steel pipes by magnetic flux leakage," *NDT&E Int.*, vol. 28, no. 1, pp. 35–40, Feb. 1995.

[21] D. L. Atherton and M.G. Daly, "Finite Element Calculation of Magnetic Flux Leakage Detector Signals," *NDT&E Int.*, vol. 20, no. 4, pp. 235–238, Aug. 1987.

[22] W. Lord, J. M. Bridges, W. Yen, and R. Palanisamy, "Residual and active leakage fields around defects in ferromagnetic materials," *Mat. Eval.*, vol. 36, pp. 47–54, Jul. 1978.

[23] S. Mandayam, L. Udpa, S. S. Udpa, and W. Lord, "Invariance transformations for magnetic flux leakage signals," *IEEE Trans. Magn.*, vol. 32, no. 3, pp. 1577–1580, May 1996.

[24] J. Philip, C. B. Rao, T. Jayakumar, and B. Raj, "A new optical technique for detection of defects in ferromagnetic materials and components," *NDT&E Int.*, vol. 33, no. 5, pp. 289–295, Jul. 2000.

[25] Y. Li, J. Wilson, and G. Y. Tian, "Experiment and simulation study of 3D magnetic field sensing for magnetic flux leakage defect characterization," *NDT& Int.*, vol. 40, no. 2, pp. 179–184, Mar. 2007.

[26] D. L. Donoho, "De-noising by soft-thresholding," *IEEE Trans Inf. Theory*, vol. 41, no. 3, pp. 613–627, May 1995.

[27] M. Afzal and S. Udpa, "Advanced signal processing of magnetic flux leakage data obtained from seamless gas pipeline," *NDT&E Int.*, vol. 35, no. 7, pp. 449–457(9), Oct. 2002.

[28] M. Afzal, R. Polikar, L. Udpa, and S. Udpa, "Adaptive noise cancellation schemes for magnetic flux leakage signals obtained from gas pipeline inspection," *IEEE Int. Conf. on Acoustics, Speech, and Signal Processing (ICASSP '01)*, vol. 6, pp. 3389–3392, May 2001.

[29] W. Han and P. Que, "A modified wavelet transform domain adaptive FIR filtering algorithm for removing the SPN in the MFL data," *Meas.*, vol. 39, no. 7, pp. 621–627, Aug. 2006.

[30] J. Tao, Q. Peiwen, C. Liang, and L. Liang, "Research on a recognition algorithm for offshore-pipeline defects during magnetic-flux inspection," *Defektoskopiya*, vol. 41, no. 4, pp. 34–43, Apr. 2005.

[31] W. Lord, *Electromagnetic methods of nondestructive testing*, Gordon and Breach Science Publishers, New York, pp. 71–151, 1985.

[32] G. S. Park and E. S. Park, "Improvement of the sensor system in magnetic flux leakage-type nondestructive testing (NDT)," *IEEE Trans. Magn.*, vol. 38, no. 2, pp. 1277–1280, Mar. 2002.

[33] Maxwell Version 11.1.1, Ansoft Corporatin, http://www.ansoft.com, 2006.

[34] S. O'Connor, L. Clapham, and P. Wild, "Magnetic flux leakage inspection of tailor-welded blanks," *Meas. Sci. Technol.*, vol. 13, no. 2, pp. 157-162, Feb. 2002.

[35] M. N. O. Sadiku, *Numerical Techniques in Electromagnetics.* 2nd ed., CRC Press, pp. 380, 2001.

[36] Y. Melikhov, S. J. Lee, D. C. Jiles, R. Lopez, and L. Brasche, "Analytical approach for fast computation of magnetic flux leakage due to surface defects," *Digests of the IEEE Int. Magnetics Conference (INTERMAG)*, Apr. 2005.

[37] J. W. Bandler, R. M. Biernacki, S. H. Chen, P. A. Grobelny, and R. H. Hemmers, "Space mapping technique for electromagnetic optimization," *IEEE Trans. Microwave Theory Tech.*, vol. 2, no. 12, pp. 2536–2544, Dec. 1994.

[38] J. W. Bandler, Q. S. Cheng, D. H. Gebre-Mariam, K. Madsen, F. Pedersen, and J. Søndergaard, "EM-based surrogate modeling and design exploiting implicit, frequency and output space mappings," in *IEEE MTT-S Int. Microw. Symp. Dig.*, Philadelphia, PA, Jun. 2003, pp. 1003–1006.

[39] J. W. Bandler, Q. S. Cheng, S. A. Dakroury, A. S. Mohamed, M. H. Bakr, K.Madsen, and J. Søndergaard, "Space mapping: The state of the art," *IEEE Trans. Microwave Theory Tech.*, vol. 52, no. 1, pp. 337–361, Jan. 2004.

[40] D. Echeverria and P.W. Hemker, "Space mapping and defect correction," *CMAM The Int. Mathematical J. Computational Methods in Applied Mathematics,* vol. 5, no. 2, pp. 107–136, 2005.

[41] S. Koziel, J. W. Bandler, and K. Madsen, "A space-mapping framework for engineering optimization: theory and implementation," *IEEE Trans. Microwave Theory Tech.*, vol. 54, no. 10, pp. 3721–3730, Oct. 2006.

[42] N. M. Alexandrov and R. M. Lewis, "An overview of first-order model management for engineering optimization," *Optimization Eng.*, vol. 2, no. 4, pp. 413–430, Dec. 2001.

[43] S. Koziel and J. W. Bandler, "Space-mapping optimization with adaptive surrogate model," *IEEE Trans. Microwave Theory Tech.*, vol. 55, no. 3, pp. 541–547, Mar. 2007.

[44] S. Koziel and J.W. Bandler, "Coarse and surrogate model assessment for engineering design optimization with space mapping", *IEEE MTT-S Int. Microwave Symp. Dig*, Honolulu, HI, 2007, pp. 107–110.

[45] Matlab^{TM}, Version 7.1, The MathWorks, Inc., 3 Apple Hill Drive, Natick, MA 01760–2098, 2005.

[46] S. Koziel and J.W. Bandler, "SMF: a user-friendly software engine for space-mapping-based engineering design optimization," *Int. Symp. Signals, Systems and Electronics, URSI ISSSE 2007*, pp. 157–160, 2007.

[47] SMF, Bandler Corporation, P.O. Box 8083, Dundas, ON, Canada L9H 5E7, 2007.

CHAPTER 6

CONCLUSION AND FUTURE WORK

In this thesis, we presented solutions of several inverse problems in the electromagnetics and microwave area. The applications included microwave imaging for breast cancer detection and MFL technique for defect characterization in metallic structures. The inverse problems related to the former application included: UWB antenna design and image reconstruction for breast tumor detection, while for the latter application inverse problems were related to defect shape's parameter estimation. Here, we describe separately the conclusions and future work related to each application.

6.1 ANTENNA DESIGN FOR BREAST IMAGING

In this thesis, a novel UWB TEM horn antenna placed in a dielectric medium was proposed for microwave imaging in breast cancer detection. The outer surface of the antenna was covered by copper sheets and a microwave absorbing sheet. The design was accomplished through full-wave simulation and then experimentally tuned for best impedance match. Simulated and experimental results confirm that the following design requirements are met. (1) The antenna does not need to be immersed in a coupling liquid. (2) The near-field power is directed entirely toward the tissue through the front aperture of the antenna. (3) Excellent isolation from external electromagnetic interference (EMI) is achieved. (4) Good impedance match in the UWB frequency range is achieved. (5) The power density distribution over the antenna aperture is fairly uniform. (6) The investigated fidelity and group velocity of the antenna demonstrates good performance of the antenna for both frequency and time-domain (radar-based) measurements. This antenna enables the development of practical imaging systems which will be easy to maintain in a clinical environment. Such systems will allow for convenient and fast sanitation of the equipment after a patient is examined. Furthermore, the specifications stated in (2) and (3) are crucial for the sensitivity and the EMI immunity of the microwave breast imaging system that have not been properly addressed in previously reported work.

Future work for this antenna may include modifications to enhance its efficiency and further reduce its aperture size. In the current design, a relatively large proportion of the power is radiated via the small apertures on the top copper shielding sheet which is absorbed by microwave absorbing sheet. This is the main reason for the reduced efficiency. An attempt could be made to decrease the size of these apertures while maintaining the UWB impedance match for the antenna.

6.2 APERTURE RASTER SCANNING FOR MICROWAVE IMAGING

In this thesis, we presented an aperture raster scanning setup to test our novel antenna in both measurements and simulations. The scanning setup clearly benefits from the excellent near-field directivity of the proposed antenna. Strong scatterers inside a homogeneous dielectric body were detected both in simulations and measurements. The detection of weak and strong scatterers in a heterogeneous breast model was also examined and the results are encouraging. A blind de-convolution technique was applied to improve the image quality. Overall, the simulation and experimental results confirm the capability of the planar raster scanning setup with the proposed antennas to provide high-quality images through near-field microwave measurements.

The advantages of the proposed system include: (1) an UWB antenna with reduced aperture size, which enables aperture raster scanning in the UWB; (2) elimination of the liquid coupling medium, which simplifies the maintenance and sanitation and reduces the power loss; (3) fast blind de-convolution algorithm to de-blur the images.

It is worth noting that in the examples considered here, the separation distance between the two antenna apertures (object thickness) was 3 cm. This distance may look unrealistic but has been chosen only as a proof of concept. In simulations, this distance was selected to expedite acquisition of the 2-D scanning results. With this current tissue thickness, each simulation takes at least 2 hours on a Pentium 4 with 16 GB of RAM. For a 2-D scan with 20 steps along each direction, more than 800 hours of simulation are required. Although we used parallel simulations on several machines, the simulation time is still very large. In the measurements, this tissue thickness has been chosen to ensure that the response due to the tumor is higher than the noise floor of VNA. In reality, tissue thicknesses will be closer to 10 cm. Thus, the expected signal levels will be much lower and the acquisition system must have larger dynamic range with sufficient SNR. We envision that using low-noise amplifiers will boost the SNR at the receiving side in conjunction with proper suppression of all electromagnetic interferences.

It is possible to further improve the quality of the acquired images while retaining real-time performance by: (i) using chirp-pulse signals similarly to chirp-pulse computed tomography [1], (ii) using holography-based shape identification [2], (iii) employing sensitivity-based detection [3], (iv) applying a complex de-blurring algorithm for improved image quality, (v) reducing the ill-posedness of the blind deconvolution algorithm by combining the de-blurring processes at all frequencies with the goal of reaching a common de-blurred image instead of obtaining individual de-blurred images at each frequency, (vi) obtaining the PSF from the measurement of a point-like scatterer (like in [1]) instead of simulation, and (vii) investigating the images obtained from the measurement of the cross-polarized coupling between the antennas.

6.3 MICROWAVE HOLOGRAPHY FOR NEAR-FIELD IMAGING

In this thesis, 2-D and 3-D holographic microwave imaging techniques were proposed using the data recorded by two antennas scanning two separate rectangular parallel apertures on both sides of a target.

In the 2-D technique, although the method uses only single-frequency measurements, the target can be localized along the range and high-quality images are obtained in the cross-range at the target's range location. The limitation of the 2-D technique is that the target should be sufficiently thin along the range direction and it should lie in a plane, which is parallel to the apertures scanned by the two antennas. The proposed method is verified through the range localization and the 2-D image reconstruction of predetermined simulated targets. The results demonstrate that the method is robust to noise and can precisely find the location of the target and can provide high-quality 2D images.

In the 3-D technique, the data is acquired using a similar setup as in the 2-D technique but wideband data is recorded at each position. The reconstruction algorithm is based on the Fourier-transform and a least-square solution. This direct inversion algorithm is indeed fast and can perform in real time. The incident field due to the transmitting antenna is simulated or measured on the reconstruction planes prior to the data acquisition. As long as the criterion for the first-order Born approximation is fulfilled and the distance between the 2D images along the range is more than the range-resolution limit, high-quality artifact-free images of the targets are created in 3-D. For the examples shown in this thesis, the technique is capable of providing high-quality images even with 5 sampling frequencies. It shows excellent robustness to noise.

These methods have several advantages compared to existing holography techniques. (1) No assumption is made about the incident field. This makes the algorithms applicable to near-field imaging where the target is close to the antenna and the spherical assumption for the illuminating wave is not valid. (2) The techniques are very robust to noise. They are capable of producing images from very noisy data with almost the same quality as the images produced from noiseless data. (3) The techniques allow for the reconstruction of targets not only from the reflection *S*-parameters but also from the transmission *S*-parameters which is appropriate for the case of transmission measurements. (4) The techniques can in principle be applied to heterogeneous media where the spatial distribution of the dielectric properties in the inspected region varies rapidly in comparison with the wavelength. Further developments in this direction are particularly important in medical imaging. (5) In 2-D holography, the target is localized in the range direction by making use of the reflection coefficients of the two antennas. The accuracy of this localization is dependent on the sampling rate along the range when the incident field data is acquired.

The proposed techniques facilitates robust, reliable, and fast near-field microwave imaging of dielectric bodies with possible application in biomedical imaging. Such applications will be the subject of future research. This involves three modifications: (1) the targets will be immersed in strongly heterogeneous lossy medium, (2) the frequency range should preferably be in the FCC approved UWB (from 3.6 to 10.1 GHz), and (3) the acquired data quality must be improved by complex de-blurring. Further, since we need to record the incident field on the target planes, a preliminary knowledge about which field component is the dominant one on the plane of the target for each specific type of transmitting antenna is crucial. Otherwise, the algorithm could be extended to use all three components of the incident field on the target planes. Also, since the techniques rely on calibration data, a good knowledge of the background medium is required in achieving high-quality images.

To further improve the accuracy of these holographic image reconstruction techniques, it is possible to obtain the Green's function related to the wave scattered at each point on the target planes and received by the receiver numerically. For this purpose, one option is to move an infinitesimal x-polarized source on reconstruction planes and compute its response at the receiving dipole antenna for all the points on the reconstruction planes and at all the frequencies. Using reciprocity principle, for each sampling position, the infinitesimal x-polarized source can be at the origin of the aperture planes while the receiver dipole antenna can be on the reconstruction planes. We can consider the latter case but to avoid a large number of simulations, we can extract the x-component of the electric field on the reconstruction planes from a single simulation instead of computing the responses received by the x-polarized dipole antenna moving on the reconstruction planes.

Furthermore, to apply these holographic imaging techniques to breast cancer imaging, the center frequency of operation could be lowered significantly due to the decrease of the wavelength inside the breast tissue. For example, for a background medium (tissue) with permittivity of 25, the operating frequency can be 7 GHz instead of 35 GHz for the examples presented in this thesis for which the background medium is air.

6.4 DEFECT CHARACTERIZATION USING MFL TECHNIQUE

We developed and validated a procedure to estimate surface breaking crack parameters, i.e., orientation, length, and depth, from single-component magnetic field measurements. The procedure consists of the following consecutive steps: estimation of orientation, estimation of length, and estimation of depth. The direct methods for estimation of orientation and length are fast and robust with respect to various lift-off distances. However, these estimations become increasingly unreliable when the crack is oriented along the magnetizing field. The results for the direct depth estimation demonstrate that when the calibration surface employs cracks whose parameters span all possible values, we can obtain accurate estimates. We observe that extrapolation toward larger crack depths is reliable as it yields estimate errors below 28%.

In another work, we presented a space mapping optimization method to estimate defect parameters from MFL data. The proposed methodology was tested and verified for two common types of defects, rectangular cracks and cylindrical pits. The results demonstrated that there is a dramatic reduction in the number of fine model evaluations and therefore CPU time when using space mapping optimization instead of direct fine model optimization. Also, the results show that the proposed fast inversion technique features much improved accuracy, especially when compared to the results obtained using the analytical models.

Here, we have used simulated MFL signals as the target responses. In practice, a measured MFL response may be degraded by mechanical and electronic noise. This may lead to misalignment between fine model and actual measurements. Proper de-noising of the measured signal has to be employed prior to solving the inverse problem. Also, uncertainties in factors such as the B-H curve of the steel pipe, the lift-off distance of the magnetic sensor, the intensity of the excitation, etc., have to be considered. Such considerations would amount to an additional step in the inversion problem where the FEM simulations are aligned with the measured signal. From our experience, excellent alignment between FEM simulation and MFL measurements could be achieved with a simple multiplication of the whole data set by a single scaling (or calibration) factor. It takes into account the differences in the excitation sources employed in reality and in the simulations.

Furthermore, the described coarse models based on the analytical formulas are available only for specific types of defects. For arbitrary shape defects, other coarse models like a lightly-trained neural network or a discretization of the defect shape into small canonical shapes with known coarse models could be used. This indicates that solving arbitrary shape defects is more involved.

Further developments of our SM optimization methodology for defect characterization has been carried out in our group and has been presented in [4][7]. In [4], a procedure to estimate the shape of the opening and the depth profile of an arbitrary three-dimensional (3-D) defect has been proposed. In this procedure, the Canny edge detection algorithm is used to estimate the shape of the defect opening. Then SM methodology is employed to approximate the defect depth profile efficiently. In [5]-[7], an approach has been proposed to estimate the characteristics of multiple narrow-opening cracks. The number, locations, orientations, and lengths of the cracks are the objective of the inversion process. The proposed procedure provides a reliable estimation of crack parameters in two separate consecutive steps. In the first step, the Canny edge detection algorithm is used to estimate the number, locations, orientations and lengths of the cracks. Then, an inversion procedure based on SM is used in order to estimate the crack depths efficiently.

REFERENCES

[1] M. Bertero, M. Miyakawa, P. Boccacci, F. Conte, K. Orikasa, and M. Furutani, "Image restoration in chirp-pulse microwave CT (CP-MCT)," *IEEE Trans. Biomed. Eng.*, vol. 47, no. 5, pp. 690–699, May 2000.

[2] M. Ravan, R. K. Amineh, and N. K. Nikolova, "Two-dimensional near-field microwave holography," *Inverse Problems*, vol. 26, 2010, 055011.

[3] Y. Song and N. K. Nikolova, "Memory efficient method for wideband self-adjoint sensitivity analysis," *IEEE Trans. Microwave Theory Tech.*, vol. 56, no. 8, pp. 1917–1927, Aug. 2008.

[4] M. Ravan, R. K. Amineh, S. Koziel, N. K. Nikolova, and J. P. Reilly, "Sizing of 3-D arbitrary defects using magnetic flux leakage measurements," *IEEE Trans. Magn.*, vol. 46, no. 4, 2010.

[5] M. Ravan, R. K. Amineh, S. Koziel, N. K. Nikolova, and J. P. Reilly, "Sizing of multiple cracks using magnetic flux leakage measurements," *IET Science, Measurement & Tech.*, vol. 4, no. 1, pp. 1–11, Jan. 2010.

[6] M. Ravan, R. K. Amineh, S. Koziel, N. K. Nikolova, and J. P. Reilly, "Sizing of multiple cracks using magnetic flux leakage measurements," *13th Int. Symp. on Antenna Tech. and Applied Electromagnetics and the*

Canadian Radio Sciences Meeting (ANTEM/URSI), Canada, 2009.

[7] M. Ravan, R. K. Amineh, S. Koziel, N. K. Nikolova, and J. P. Reilly, "Estimation of multiple surface cracks parameters using MFL testing," *Int. Union of Radio Science Commission B and Int. Symp. on Electromagnetic Theory (URSI/EMTS)*, Germany, 2010.

Appendix A. Formulation of the Inverse Scattering Problem

The Maxwell's equations in a time-harmonic regime assuming only electric current excitation $\boldsymbol{J}$ are

$$\nabla \times \boldsymbol{E} = -j\omega\mu_0 \boldsymbol{H} \tag{A.1}$$

$$\nabla \times \boldsymbol{H} = j\omega \boldsymbol{D} + \boldsymbol{J} \tag{A.2}$$

where μ_0 and ω are the permeability of the medium and the angular frequency, respectively. By taking the curl of both sides of (A.1) and combining that with (A.2), we obtain the vector Helmholtz equation

$$\nabla \times \nabla \times \boldsymbol{E} - k^2 \boldsymbol{E} = -j\omega\mu_0 \boldsymbol{J} \tag{A.3}$$

where $k^2 = \omega^2 \mu_0 \varepsilon - j\omega\mu_0 \sigma$ and ε and σ are the complex permittivity and conductivity of the medium, respectively.

Now, we consider two scenarios: 1) the target is not present and 2) the target is present. For these two cases (A.3) is written as:

$$\nabla \times \nabla \times \boldsymbol{E}^{\mathrm{inc}} - k_{\mathrm{b}}^2 \boldsymbol{E}^{\mathrm{inc}} = -j\omega\mu_0 \boldsymbol{J} \tag{A.4}$$

$$\nabla \times \nabla \times \boldsymbol{E}^{\mathrm{tot}} - k_{\mathrm{s}}^2 \boldsymbol{E}^{\mathrm{tot}} = -j\omega\mu_0 \boldsymbol{J} \tag{A.5}$$

where $\boldsymbol{E}^{\mathrm{inc}}$ and $\boldsymbol{E}^{\mathrm{tot}}$ are electric fields for the cases without and with the target, respectively, and k_{b} and k_{s} are the complex wavenumbers in the investigated region for the cases without and with the target, respectively. Subtracting (A.4) from (A.5) and doing simplifications lead to

$$\nabla \times \nabla \times \boldsymbol{E}^{\mathrm{sc}} - k_{\mathrm{s}}^2 \boldsymbol{E}^{\mathrm{sc}} = -(k_{\mathrm{s}} - k_{\mathrm{b}}) \boldsymbol{E}^{\mathrm{tot}} . \tag{A.6}$$

The general form solution for (A.6) is 0

$$\boldsymbol{E}^{\mathrm{sc}}(\boldsymbol{r}) = \iiint_V \mathbf{G}(\boldsymbol{r},\boldsymbol{r}') \cdot \boldsymbol{E}^{\mathrm{tot}}(\boldsymbol{r}')(k_{\mathrm{s}}(\boldsymbol{r}') - k_0) d\boldsymbol{r}' \tag{A.7}$$

where V is the target volume and $\mathbf{G}(\boldsymbol{r},\boldsymbol{r}')$ is the dyadic Green's function.

In (A.7), the total field $\boldsymbol{E}^{\mathrm{tot}}$ inside the target can be approximated by the incident field (field in the same region when the target is not present), i.e., $\boldsymbol{E}^{\mathrm{tot}} \approx \boldsymbol{E}^{\mathrm{inc}}$. This is known as the linear Born approximation for the weak or small scatterers 0. Therefore, (A.7) is approximated as:

$$\boldsymbol{E}^{\mathrm{sc}}(\boldsymbol{r}) = \iiint_V \boldsymbol{G}(\boldsymbol{r},\boldsymbol{r}') \cdot \boldsymbol{E}^{\mathrm{inc}}(\boldsymbol{r}')(k_{\mathrm{s}}(\boldsymbol{r}') - k_0) d\boldsymbol{r}' \tag{A.8}$$

REFERENCES

[1] Chew W 1995 *Waves and Fields in Inhomogeneous Media* Piscataway, NJ: IEEE Press.

BIBLIOGRAPHY

A. Abubakar and P. M. van den Berg, "Iterative forward and inverse algorithms based on domain integral equations for three-dimensional electric and magnetic objects," *J. Comput. Phys.*, vol. 195, no. 1, pp. 236–262, Mar. 2004.

A. Abubakar, P. M. van den Berg, and J. J. Mallorqui, "Imaging of biomedical data using a multiplicative regularized contrast source inversion method," *IEEE Trans. Microwave Theory Tech.*, vol. 59, no. 7, pp. 1761–1771, Jul. 2002.

M. Afzal and S. Udpa, "Advanced signal processing of magnetic flux leakage data obtained from seamless gas pipeline," *NDT&E Int.*, vol. 35, no. 7, pp. 449–457(9), Oct. 2002.

M. Afzal, R. Polikar, L. Udpa, and S. Udpa, "Adaptive noise cancellation schemes for magnetic flux leakage signals obtained from gas pipeline inspection," *IEEE Int. Conf. on Acoustics, Speech, and Signal Processing (ICASSP '01)*, vol. 6, pp. 3389–3392, May 2001.

R. Aitmehdi, A. P. Anderson, S. Sali, and M. Ferrando, "The determination of dielectric loss tangent by microwave phase tomography," *Inv. Problems*, vol. 4, no. 2, pp. 333–345, May 1988.

N. M. Alexandrov and R. M. Lewis, "An overview of first-order model management for engineering optimization," *Optimization Eng.*, vol. 2, no. 4, pp. 413–430, Dec. 2001.

E. Altschuler and A. Pignotti, "Nonlinear model of flaw detection in steel pipes by magnetic flux leakage," *NDT&E Int.,* vol. 28, no. 1, pp. 35–40, Feb. 1995.

R. K. Amineh, A. Trehan, and N. K. Nikolova, "TEM horn antenna for ultra-wide band microwave breast imaging," *Progress In Electromagnetics Research B (PIER B)*, vol. 13, pp. 59–74, 2009.

R. K. Amineh, M. Ravan, A. Trehan, and N. K. Nikolova, "Near-field microwave imaging based on aperture raster scanning with TEM horn antennas," submitted to *IEEE Trans. Antennas and Propag.*

R. K. Amineh, M. Ravan, A. Trehan, and N. K. Nikolova, "Microwave imaging for breast cancer diagnosis based on planar aperture scanning," *IEEE Int. Symp. on Antennas and Propag. and USNC/URSI National Radio Science Meeting (AP-S/URSI)*, Canada, 2010.

R. K. Amineh and N. K. Nikolova, "Design, fabrication, and characterization of ultra-wide band TEM horn for microwave imaging," *14th Int. Symp. on Antenna Tech. and Applied Electromagnetics and the Canadian Radio Sciences Meeting (ANTEM/AMEREM)*, Canada, 2010.

R. K. Amineh, M. Ravan, A. Trehan, and N. K. Nikolova, "Near-field microwave imaging based on planar aperture scanning," *IEEE MTT Int. Microwave Symp. (IMS)*, USA, 2010.

R. K. Amineh, A. Trehan, and N. K. Nikolova, "Ultra-wide band TEM horn antenna for microwave imaging of the breast," *IEEE Int. Symp. on Antennas and Propag. and USNC/URSI National Radio Science Meeting (AP-S/URSI)*, USA, 2009.

R. K. Amineh, A. Trehan, and N. K. Nikolova, "Ultra-wide band TEM horn antenna designed for microwave imaging of the breast," *13th Int. Symp. on Antenna Tech. and Applied Electromagnetics and the Canadian Radio Sciences Meeting (ANTEM/URSI)*, Canada, 2009.

R. K. Amineh, A. Trehan, M. Ravan, and N. K. Nikolova, "Planar aperture scanning for microwave imaging of the breast: advances and challenges," *IEEE Int. Symp. on Antennas and Propag. and USNC/URSI National Radio Science Meeting (AP-S/URSI)*, Canada, 2010.

R. K. Amineh, M. Ravan, and N. K. Nikolova, "Three-dimensional microwave holography for near-field imaging of dielectric bodies," submitted to *Inverse Problems*.

R. K. Amineh, N. K. Nikolova, J. P. Reilly, and J. R. Hare, "Characterization of surface breaking cracks using one tangential component of magnetic leakage field," *IEEE Trans. Magn.*, vol. 44, no. 4, pp. 516–524, Apr. 2008.

R. K. Amineh, S. Koziel, N. K. Nikolova, J. W. Bandler, and J. P. Reilly, "A space mapping methodology for defect characterization from magnetic flux leakage measurements," *IEEE Trans. Magn.*, vol. 44, no. 8, pp. 2058–2065, Aug. 2008.

R. K. Amineh, N. K. Nikolova, J. P. Reilly, and J. R. Hare, "Characterization of surface breaking cracks," *20th Int. Pipeline Pigging & Integrity Management Conf.,* USA 2008.

R. K. Amineh, S. Koziel, N. K. Nikolova, J. W. Bandler, and J. P. Reilly, "A space mapping methodology for defect characterization," *24th Int. Review of Progress in Applied Computational Electromagnetics (ACES),* Canada, 2008.

Ansoft Corporation, USA, http://www.ansoft.com.

D. L. Atherton and M.G. Daly, "Finite Element Calculation of Magnetic Flux Leakage Detector Signals," *NDT&E Int.,* vol. 20, no. 4, pp. 235–238, Aug. 1987.

J. W. Bandler, R. M. Biernacki, S. H. Chen, P. A. Grobelny, and R. H. Hemmers, "Space mapping technique for electromagnetic optimization," *IEEE Trans. Microwave Theory Tech.*, vol. 2, no. 12, pp. 2536–2544, Dec. 1994.

J. W. Bandler, Q. S. Cheng, D. H. Gebre-Mariam, K. Madsen, F. Pedersen, and J. Søndergaard, "EM-based surrogate modeling and design exploiting implicit, frequency and output space mappings," in *IEEE MTT-S Int. Microw. Symp. Dig.*, Philadelphia, PA, June 2003, pp. 1003–1006.

J. W. Bandler, Q. S. Cheng, S. A. Dakroury, A. S. Mohamed, M. H. Bakr, K.Madsen, and J. Søndergaard, "Space mapping: The state of the art," *IEEE Trans. Microwave Theory Tech.*, vol. 52, no. 1, pp. 337–361, Jan. 2004.

A. Banos, *Dipole Radiation in the Presence of a Conducting Half-Space*, Pergamon Press, New York, 1966.

M. Benedetti, M. Donelli, G. Franceschini, M. Pastorino, and A. Massa, "Effective exploitation of the *a priori* information through a microwave imaging procedure based on the SMW for NDE/NDT applications," *IEEE Trans. Geosc. Remote Sens.*, vol. 43, no. 11, pp. 2584–2592, Nov. 2005.

R. Benjamin, "Synthetic, post-reception focusing in near-field radar," *Proc. EUREL Int. Conf. on the Detection of Abandoned Land Mines: A Humanitarian Imperative Seeking a Tech. Solution*, Oct. 7–9, 1996, pp. 133–137.

R. Benjamin, "Detecting reflective object in reflective medium," U.K. GB 2313969, Dec. 10, 1997.

M. Bertero, M. Miyakawa, P. Boccacci, F. Conte, K. Orikasa, and M. Furutani, "Image restoration in chirp-pulse microwave CT (CP-MCT)," *IEEE Trans. Biomed. Eng.*, vol. 47, no. 5, pp. 690–699, May 2000.

D. S. C. Biggs and M. Andrews, "Acceleration of iterative image restoration algorithms," *Applied Optics*, vol. 36, no. 8, pp. 1766–1775, Mar. 1997.

J. C. Bolomey, "New concept for microwave sensing," *Adv. Microwave Millim. Wave Detectors*, vol. 2275, 1994.

J. C. Bolomey, A. Izadnegahdar, L. Jofre, C. Pichot, G. Peronnet, and M. Solaimani, "Microwave diffraction tomography for biomedical applications," *IEEE Trans. Microwave Theory Tech.*, vol. 30, no. 11, pp. 1998–2000, Nov. 1982.

J. C. Bolomey, C. Pichot, and G. Gaboriaud, "Planar microwave camera for biomedical applications: Critical and prospective analysis of reconstruction algorithms," *Radio Sci.*, vol. 26, no. 2, pp. 541–549, Mar.–Apr. 1991.

E. J. Bond, L. Xu, S. C. Hagness, and B. D. Van Veen, "Microwave imaging via space-time beamforming for early detection of breast cancer," in *Proc. IEEE Int. Conf. on Acoust., Speech, and Signal Process. (ICASSP '02)*, May 13–17, 2002, vol. 3, pp. III-2909–III-2912.

A. E. Bulyshev, A. E. Souvorov, S. Y. Semenov, V. G. Posukh, and Y. E. Sizov, "Three-dimensional vector microwave tomography: Theory and computational experiments," *Inv. Problems*, vol. 20, no. 4, pp. 1239–1259, Aug. 2004.

S. Caorsi, G. L. Gragnani, and M. Pastorino, "Reconstruction of dielectric permittivity distributions in arbitrary 2-D inhomogeneous biological bodies by a multiview microwave numerical method," *IEEE Trans. Med. Imag.*, vol. 12, no. 6, pp. 232–239, Jun. 1993.

S. Caorsi, G. L. Gragnani, M. Pastorino, and M. Sartore, "Electromagnetic imaging of infinite dielectric cylinders using a modified born approximation and including *a priori* information on the unknown cross sections," *Proc. Inst. Elect. Eng.—Microw. Antennas Propag.*, vol. 141, no. 6, pp. 445–450, Dec. 1994.

J. T. Case, I. Robbins, S. Kharkovsky, F. Hepburn, and R. Zoughi, "Microwave and millimeter wave imaging of the space shuttle external fuel tank spray on foam insulation (SOFL) using synthetic aperture focusing techniques," (SAFT) *Review of Quantitative Nondestructive Evaluation*, vol. 25, pp. 1546−1553, 2006.

Z. Chen, G. Preda, O. Mihalache, and K. Miya, "Reconstruction of crack shapes from the MFLT signals by using a rapid forward solver and an optimization approach," *IEEE Trans. Magn.*, vol. 38, no. 2, pp. 1025–1028, Mar. 2002.

W. C. Chew and Y. M.Wang, "Reconstruction of two-dimensional permittivity distribution using the distorted born iterative method," *IEEE Trans. Med. Imag.*, vol. 9, no. 2, pp. 218–225, Jun. 1990.

W. C. Chew and J. H. Lin, "A frequency-hopping approach for microwave imaging of large inhomogeneous bodies," *IEEE Microwave Guided Wave Lett.*, vol. 5, no. 12, pp. 439–441, Dec. 1995.

K. Chung, S. Pyun, and J. Choi, "Design of an ultrawide-band TEM horn antenna with a microstrip-type balun," *IEEE Trans. Antennas and Propag.*, vol. 53, no. 10, pp. 3410–3413, Oct. 2005.

D. Colton and P. Monk, "The detection and monitoring of leukemia using electromagnetic waves: mathematical theory," *Inv. Problems*, vol. 10, pp. 1235–1251, 1994.

CST Computer Simulation Technology AG., http://www.cst.com.

S. K. Davis, B. D. Van Veen, S. C. Hagness, and F. Kelcz, "Breast tumor characterization based on ultrawide band microwave backscatter," *IEEE Trans. Biomed. Eng.*, vol. 55, no. 1, pp. 237–246, Jan. 2008.

A. J. Devaney, "Reconstructive tomography with diffracting wave-fields," *Inv. Problems*, vol. 2, no. 2, pp. 161−183, May 1986.

J. Detlefsen, A. Dallinger, and S. Schelkshorn, "Effective reconstruction approaches to millimeter-wave imaging of humans," *XXVIIIth General Assembly of Int. Union of Radio Science (URSI)*, pp 23–29, 2005.

D. L. Donoho, “De-noising by soft-thresholding,” *IEEE Trans Inf. Theory*, vol. 41, no. 3, pp. 613–627, May 1995.

O. Dorn, E. L. Miller, and C. M. Rappaport, “A shape reconstruction method for electromagnetic tomography using adjoint fields and level sets,” *Inv. Problems*, vol. 16, no. 5, pp. 1119–1156, Oct. 2000.

D. Echeverria and P.W. Hemker, “Space mapping and defect correction,” *CMAM The Int. Mathematical J. Computational Methods in Applied Mathematics,* vol. 5, no. 2, pp. 107–136, 2005.

C. Edwards and S. B. Palmer, “The magnetic leakage field of surface-breaking cracks,” *J. Phys. D: Appl. Phys.*, vol. 19, no. 4, pp 657–673, Apr. 1986.

M. Elsdon, M. Leach, S. Skobelev, and D. Smith, “Microwave holographic imaging of breast cancer,” *IEEE Int. Symp. on Microwave, Antenna, Propag., and EMC Tech. For Wireless Commun.*, pp. 966–969, 2007.

Emerson & Cuming Microwave Products, http://www.eccosorb.com.

EM Software & Systems-S.A. (Pty) Ltd., http://www.feko.info.

Q. Fang, P. M. Meaney, S. D. Geimer, A. V. Streltsov, and K. D. Paulsen, “Microwave image reconstruction from 3-D fields coupled to 2-D parameter estimation,” *IEEE Trans. Med. Imag.*, vol. 23, no. 4, pp. 475–484, Apr. 2004.

N. H. Farhat and W. R. Guard, “Holographic imaging at 70 GHz,” *Proc. of the IEEE*, vol. 58, no. 12, pp. 1955−1956, 1970.

N. H. Farhat and W. R. Guard, “Millimeter wave holographic imaging of concealed weapons,” *Proc. of the IEEE*, vol. 59, pp. 1383−1384, 1971.

R. Ferrayé, J.-Y. Dauvignac, and C. Pichot, “An inverse scattering method based on contour deformations by means of a level set method using frequency hopping technique,” *IEEE Trans. Antennas Propag.*, vol. 51, no. 5, pp. 1100–1113, May 2003.

A. Fhager and M. Persson, “Comparison of two image reconstruction algorithms for microwave tomography,” *Radio Sci.*, vol. 40, no. 3, Jun. 2005, Article RS3017.

A. Fhager and M. Persson, “Using *a priori* data to improve the reconstruction of small objects in microwave tomography,” *IEEE Trans. Microwave Theory Tech.*, vol. 55, no. 11, pp. 2454–2462, Nov. 2007.

E. C. Fear and M. A. Stuchly, “Microwave detection of breast cancer,” *IEEE Trans. Microwave Theory Tech.*, vol. 48, no. 11, pp. 1854–1863, Nov. 2000.

E. C. Fear, J. Sill, and M. A. Stuchly, “Experimental feasibility study of confocal microwave imaging for breast tumor detection,” *IEEE Trans. Microw. Theory Tech.*, vol. 51, pp. 887–892, Mar. 2003.

E. C. Fear and M. A. Stuchly, “Microwave system for breast tumor detection,” *IEEE Microwave Wireless Compon. Lett.*, vol. 9, pp. 470–472, Nov. 1999.

O. Féron, B. Duchêne, and A. Mohammad-Djafari, “Microwave imaging of inhomogeneous objects made of a finite number of dielectric and conductive materials from experimental data,” *Inv. Problems*, vol. 21, no. 6, pp. S95–S115, Dec. 2005.

S. C. Hagness, A. Taflove, and J. E. Bridges, “Two-dimensional FDTD analysis of a pulsed microwave confocal system for breast cancer detection: Fixed-focus and antenna-array sensors,” *IEEE Trans. Biomed. Eng.*, vol. 45, pp. 1470–1479, Dec. 1998.

W. Han and P. Que, “Defect reconstruction of submarine oil pipeline from MFL signals using genetic simulated annealing algorithm,” *J. Japan Petr. Inst.*, vol. 49, no. 3, pp. 145–150, 2006.

W. Han and P. Que, “2-D defect reconstruction from MFL signals by a genetic optimization algorithm,” *Russian J. of NDT,* vol. 41, no. 12, pp. 809–814, Dec. 2005.

W. Han and P. Que, “A modified wavelet transform domain adaptive FIR filtering algorithm for removing the SPN in the MFL data,” *Meas.*, vol. 39, no. 7, pp. 621–627, Aug. 2006.

P. T. Huynh, A. M. Jarolimek, and S. Daye, “The false-negative mammogram,” *Radiographics*, vol. 18, pp. 1137–1154, 1998.

T. Isernia, V. Pascazio, and R. Pierri, “On the local minima in a tomographic imaging technique,” *IEEE Trans. Geosci. Remote Sens.*, vol. 39, no. 7, pp. 1596–1607, Jul. 2001.

J. H. Jacobi, L. E. Larsen, and C. T. Hast, "Water-immersed microwave antennas and their application to microwave interrogation of biological targets," *IEEE Trans. Microwave Theory Tech.*, vol. MTT-27, no. 1, pp. 70–78, Jan. 1979.

H. M. Jafari, M. J. Deen, S. Hranilovic, and N. K. Nikolova, "A study of ultrawideband antennas for near-field imaging," *IEEE Trans. Antennas and Propag.*, vol. 55, no. 4, pp. 1184–1188, Apr. 2007.

H. M. Jafari, J. M. Deen, S. Hranilovic, and N. K. Nikolova, "Co-polarised and cross-polarised antenna arrays for breast, cancer detection," *IET Microwave Antennas Propag.*, vol. 1, no. 5, pp. 1055–1058, Oct. 2007.

N. Joachimowicz, C. Pichot, and J. P. Hugonin, "Inverse scattering: An iterative numerical method for electromagnetic imaging," *IEEE Trans. Antennas Propag.*, vol. 39, no. 12, pp. 1742–1753, Dec. 1991.

L. Jofre, M. S. Hawley, A. Broquetas, E. de los Reyes, M. Ferrando, and A. R. Elias-Fusté, "Medical imaging with a microwave tomographic scanner," *IEEE Trans. Biomed. Eng.*, vol. 37, no. 3, pp. 303–312, Mar. 1990.

C. H. Jones, "Methods of breast imaging," *Phys. Med. Biol.*, vol. 27, pp. 463–499, Apr. 1982.

A. Joshi, L. Udpa, S. S. Udpa, and A. Tamburrino, "Adaptive wavelets for characterizing magnetic flux leakage signals from pipeline inspection," *IEEE Trans. Magn.*, vol. 42, no. 10, pp. 3168–3170, Oct. 2006.

H. Kanj and M. Popovic, "A novel ultra-compact broadband antenna for microwave breast tumor detection," *Progress In Electromagnetics Research*, PIER 86, pp. 169–198, 2008.

R. E. Kleinman and P. M. van den Berg, "A modified gradient method for two-dimensional problems in tomography," *J. Comput. Appl. Math.*, vol. 42, no. 1, pp. 17–35, Sep. 1992.

M. Klemm, I. J. Craddock, J. A. Leendertz, A. Preece, and R. Benjamin "Radar-based breast cancer detection using a hemispherical antenna array-experimental results" *IEEE Trans. Antennas and Propag.*, vol. 57, no. 6, pp. 1692–1704, Jun. 2009.

P. Kosmas and C. Rappaport, “A FDTD-based time reversal for microwave breast cancer detection—Localization in three dimensions,” *IEEE Trans. Microwave Theory Tech.*, vol. 54, no. 4, pp. 1921–1927, Apr. 2006.

S. Koziel, J. W. Bandler, and K. Madsen, “A space-mapping framework for engineering optimization: theory and implementation,” *IEEE Trans. Microwave Theory Tech.*, vol. 54, no. 10, pp. 3721–3730, Oct. 2006.

S. Koziel and J. W. Bandler, “Space-mapping optimization with adaptive surrogate model,” *IEEE Trans. Microwave Theory Tech.*, vol. 55, no. 3, pp. 541–547, Mar. 2007.

S. Koziel and J.W. Bandler, “Coarse and surrogate model assessment for engineering design optimization with space mapping”, *IEEE MTT-S Int. Microwave Symp. Dig*, Honolulu, HI, 2007, pp. 107–110.

S. Koziel and J.W. Bandler, “SMF: a user-friendly software engine for space-mapping-based engineering design optimization,” *Int. Symp. Signals, Systems and Electronics, URSI ISSSE 2007*, pp. 157–160, 2007.

D. Kundur and D. Hatzinakos, “Blind image de-convolution,” *IEEE Signal Proc. Mag.*, May 1996.

D. J. Kurrant and E. C. Fear, “An improved technique to predict the time-of-arrival of a tumor response in radar-based breast imaging,” *IEEE Trans. Biomed. Eng.*, vol. 56, no. 4, pp. 1200–1208, Apr. 2009.

D. Lamensdorf and L. Susman, “Baseband-pulse-antenna techniques,” *IEEE Antennas Propag. Mag.*, vol. 36, no. 1, pp. 20–30, Feb. 1994.

L. E. Larsen and J. H. Jacobi, “Microwave scattering parameter imagery of an isolated canine kidney,” *Med. Phys.*, vol. 6, pp. 394–403, 1979.

M. Lazebnik, L. McCartney, D. Popovic, C. B. Watkins, M. J. Lindstrom, J. Harter, S. Sewall, A. Magliocco, J. H. Booske, M. Okoniewski, and S. C. Hagness, “A large-scale study of the ultrawide band microwave dielectric properties of normal breast tissue obtained from reduction surgeries,” *Phys. Med. Biol.* , vol. 52, pp. 2637–2656, May 2007.

M. Lazebnik, M. Okoniewski, J. H. Booske, and S. C. Hagness, “Highly accurate Debye models for normal and malignant breast tissue dielectric properties at microwave frequencies,” *IEEE Microwave and Wirel. Components Lett.*, vol. 17, no. 12, Dec. 2007.

X. Li, S. K. Davis, S. C. Hagness, D. V. der Wedge, and B. D. V. Veen, "Microwave imaging via space–time beamforming: experimental investigation of tumor detection in multi-layer breast phantoms," *IEEE Trans. Microwave Theory Tech.*, vol. 52, no. 8, pp. 1856–1865, Aug. 2004.

X. Li, S. C. Hagness, M. K. Choi, and D. Van Der Weide, "Numerical and experimental investigation of an ultra-wideband ridged pyramidal-horn antenna with curved launching plane for pulse radiation," *IEEE Antennas Wirel. Propag. Lett.*, vol. 2, pp. 259–262, 2003.

Y. Li, J. Wilson, and G. Y. Tian, "Experiment and simulation study of 3D magnetic field sensing for magnetic flux leakage defect characterization," *NDT& Int.*, vol. 40, no. 2, pp. 179–184, Mar. 2007.

A. Litman, "Reconstruction by level sets of n-ary scattering obstacles," *Inv. Problems*, vol. 21, no. 6, pp. S131–S152, Dec. 2005.

Q. H. Liu, Z. Q. Zhang, T. T. Wang, J. A. Bryan, G. A. Yabbara, L. W. Nolte, and W. T. Jones, "Active microwave imaging I—2-D forward and inverse scattering methods," *IEEE Trans. Microwave Theory Tech.*, vol. 50, no. 1, pp. 123–133, Jan. 2002.

W. Lord and J. H. Hwang, "Defect characterization from magnetic flux leakage fields," *British J. NDT*, vol. 19, no. 1, pp. 14–18, Jan. 1977.

W. Lord, J. M. Bridges, W. Yen, and R. Palanisamy, "Residual and active leakage fields around defects in ferromagnetic materials," *Mat. Eval.,* vol. 36, pp. 47–54, Jul. 1978.

W. Lord, *Electromagnetic methods of nondestructive testing*, Gordon and Breach Science Publishers, New York, pp. 71–151, 1985.

C. Mandache and L. Clapham, "A model for magnetic flux leakage signal Predictions," *J. Phys. D: Appl. Phys.*, vol. 36, no. 20, pp. 2427–2431, Oct. 2003.

S. Mandayam, L. Udpa, S. S. Udpa, and W. Lord, "Invariance transformations for magnetic flux leakage signals," *IEEE Trans. Magn.*, vol. 32, no. 3, pp. 1577–1580, May 1996.

Matlab^{TM}, Version 7.1, The MathWorks, Inc., 3 Apple Hill Drive, Natick, MA 01760–2098, 2005.

Maxwell Version 11.1.1, Ansoft Corporatin, http://www.ansoft.com, 2006.

P. M. Meaney, M. W. Fanning, T. Raynolds, C. J. Fox, Q. Fang, C. A. Kogel, S. P. Poplack, and K. D. Paulsen, "Initial clinical experience with microwave breast imaging in women with normal mammography," *Acad Radiol.*, vol. 14, no. 2, pp. 207–218, Feb. 2007.

P. Meaney, K. D. Paulsen, A. Hartov, and R. K. Crane, "An active microwave imaging system for reconstruction of 2-D electrical property distributions," *IEEE Trans. Biomed. Eng.*, vol. 42, no. 10, pp. 1017–1026, Oct. 1995.

Y. Melikhov, S. J. Lee, D. C. Jiles, R. Lopez, and L. Brasche, "Analytical approach for fast computation of magnetic flux leakage due to surface defects," *Digests of the IEEE Int. Magnetics Conference (INTERMAG)*, Apr. 2005.

D. Minkov, J. Lee, and T. Shoji, "Study of crack inversions utilizing dipole model of a crack and Hall element measurements," *J. Magn. Magn. Mater.*, vol. 217, no. 1, pp. 207–215, Jul. 2000.

D. Minkov, Y. Takeda, T. Shoji, and J. Lee, "Estimating the sizes of surface cracks based on Hall element measurements of the leakage magnetic field and a dipole model of a crack," *J. Appl. Phys. A*, vol. 74, no. 2, pp. 169–176, Feb. 2002.

T. P. Montoya and G. S. Smith, "Land mine detection using a ground-penetrating radar based on resistively loaded Vee dipoles," *IEEE Trans. Antennas and propag.,* vol. 47, no. 12, pp. 1795–1806, 1999.

D. C. Munson, J. D. Jr. O'Brien, and W. K. Jenkins, "A tomographic formulation of spotlight-mode synthetic aperture radar," *Proc. of the IEEE*, vol. 71, no. 8, pp. 917–925, 1983.

P. Neittaanmaki, M. Rudnicki, and A. Savini, *Inverse Problems and Optimal Design in Electricity and Magnetism*. Clarendon Press, Oxford, 1996.

N. K. Nikolova, D. Cronin, S. M. Pasha, R. K. Amineh, I. Smith, R. Thompson, and J. R. Hare, "Electrical resistance welded seam inspection using circumferential flux," *7th Int. Pipeline Conference (IPC)*, Canada, 2008.

R. Nilavalan, I. J. Craddock, A. Preece, J. Leendertz, and R. Benjamin, "Wideband microstrip patch antenna design for breast cancer tumour detection," *IET Microwave Antennas Propag.*, vol. 1, no. 2, pp. 277–281, Apr. 2007.

R. Nilavalan, J. Leendertz, I. J. Craddock, R. Benjamin, and A. Preece, "Breast tumor detection using a flat 16 element array," *16th Int. Symp. on Electromagn. Compat. Topical Meeting on Biomed.EMC*, Zurich, Switzerland, Feb. 2005, pp. 81–84.

S. O'Connor, L. Clapham, and P. Wild, "Magnetic flux leakage inspection of tailor-welded blanks," *Meas. Sci. Technol.*, vol. 13, no. 2, pp. 157-162, Feb. 2002.

J. Odendaal, J. Joubert, and M. J. Prinsloo, "Extended edge wave diffraction model for near-filed directivity calculations of horn antennas," *IEEE Trans. Instrument. and Measur.*, vol. 54, no. 6, pp. 2469–2473, Dec. 2005.

G. S. Park and E. S. Park, "Improvement of the sensor system in magnetic flux leakage-type nondestructive testing (NDT)," *IEEE Trans. Magn.*, vol. 38, no. 2, pp. 1277–1280, Mar. 2002.

D. M. Parkin, F. Bray, J. F. And, and P. Pisani, "Global cancer statistics, 2002," *CA: A Cancer J. Clinicians*, vol. 55, pp. 74–108, Mar. 2005.

J. Philip, C. B. Rao, T. Jayakumar, and B. Raj, "A new optical technique for detection of defects in ferromagnetic materials and components," *NDT&E Int.*, vol. 33, no. 5, pp. 289–295, Jul. 2000.

C. Pichot, L. Jofre, G. Peronnet, and J. C. Bolomey, "Active microwave imaging of inhomogeneous bodies," *IEEE Trans. Antennas Propag.*, vol. 33, no. 4, pp. 416–425, Apr. 1985.

D. Pozar, *Microwave Engineering*, John Wiley & Sons, Inc., 2005.

P. Ramuhalli, L. Udpa, and S. S. Udpa, "Electromagnetic NDE signal inversion by function-approximation neural networks," *IEEE Trans. Magn.*, vol. 38, no. 6, pp. 3633–3642, Nov. 2002.

P. Ramuhalli, L. Udpa, and S. S. Udpa, "Neural network-based inversion algorithms in magnetic flux leakage nondestructive evaluation," *J. Appl. Phys.*, vol. 93, no. 10, pp. 8274–8276, May 2003.

M. Ravan, R. K. Amineh, and N. K. Nikolova, "Two-dimensional near-field microwave holography," accepted for publication in *Inverse Problems*.

M. Ravan, R. K. Amineh, and N. K. Nikolova, "Microwave holography for near-field imaging," *AP-S/URSI 2010*, Canada.

M. Ravan, R. K. Amineh, and N. K. Nikolova, "Near-field microwave holographic imaging: target localization and resolution study," *URSI/EMTS 2010*, Germany.

M. Ravan, R. K. Amineh, S. Koziel, N. K. Nikolova, and J. P. Reilly, "Sizing of 3-D arbitrary defects using magnetic flux leakage measurements," *IEEE Trans. Magn.*, vol. 46, no. 4, 2010.

M. Ravan, R. K. Amineh, S. Koziel, N. K. Nikolova, and J. P. Reilly, "Sizing of multiple cracks using magnetic flux leakage measurements," *IET Science, Measurement & Tech.*, vol. 4, no. 1, pp. 1−11, Jan. 2010.

M. Ravan, R. K. Amineh, S. Koziel, N. K. Nikolova, and J. P. Reilly, "Sizing of multiple cracks using magnetic flux leakage measurements," *13th Int. Symp. on Antenna Tech. and Applied Electromagnetics and the Canadian Radio Sciences Meeting (ANTEM/URSI)*, Canada, 2009.

M. Ravan, R. K. Amineh, S. Koziel, N. K. Nikolova, and J. P. Reilly, "Estimation of multiple surface cracks parameters using MFL testing," *Int. Union of Radio Science Commission B and Int. Symp. on Electromagnetic Theory (URSI/EMTS)*, Germany, 2010.

T. Rubæk, P. M. Meaney, P. Meincke, and K. D. Paulsen, "Nonlinear microwave imaging for breast-cancer screening using Gauss–Newton's method and the CGLS inversion algorithm," *IEEE Trans. Antennas and Propag.*, vol. 55, no. 8, pp. 2320–2331, Aug. 2007.

M. Säbel and H. Aichinger, "Recent developments in breast imaging," *Phys. Med. Biol.*, vol. 41, pp. 315–368, Mar. 1996.

M. N. O. Sadiku, *Numerical Techniques in Electromagnetics.* 2nd ed., CRC Press, pp. 380, 2001.

F. Santosa, "A level-set approach for inverse problems involving obstacles," *ESIAM: Control, Optim., Calculus of Variations*, vol. 1, pp. 17–33, 1996.

R. Schifini and A. C. Bruno, "Experimental verification of a finite element model used in a magnetic flux leakage inverse problem," *J. Phys.D: Appl. Phys.*, vol. 38, no. 12, pp. 1875–1880, June 2005.

S. Y. Semenov, A. E. Bulyshev, A. Abubakar, V. G. Posukh, Y. E. Sizov, A. E. Souvorov, P. M. van den Berg, and T. C. Williams, "Microwave-tomographic imaging of high dielectric-contrast objects using different image-reconstruction approaches," *IEEE Trans. Microwave Theory Tech.*, vol. 53, no. 7, pp. 2284–2295, Jul. 2005.

D. M. Sheen, D. L. McMakin, and T. E. Hall, "Three-dimensional millimeter-wave imaging for concealed weapon detection," *IEEE Trans. Microwave Theory and Tech.*, vol. 49, no. 9, pp. 1581–1592, 2001.

D. M. Sheen, D. L. McMakin, and T. E. Hall, "Near field imaging at microwave and millimeter wave frequencies," *IEEE/MTT-S Int. Microwave Symp.*, pp. 1693−1696, 2007.

J. M. Sill and E. C. Fear, "Tissue sensing adaptive radar for breast cancer detection—experimental investigation of simple tumor models," *IEEE Trans. Microwave Theory Tech.*, vol. 53, pp. 3312–3319, Nov. 2005.

J. M. Sill and E. C. Fear, "Tissue sensing adaptive radar for breast cancer detection: study of immersion liquids," *Electron. Lett.*, vol. 41, no. 3, pp. 113–115, 2005.

M. Slaney, A. C. Kak, and L. E. Larsen, "Limitations of imaging with first order diffraction tomography," *IEEE Trans. Microwave Theory Tech.*, vol. 32, no. 8, pp. 860–873, Aug. 1984.

D. Slater, *Near-Field Antenna Measurements*, Artech House, Boston, 1991.

Y. Song and N. K. Nikolova, "Memory efficient method for wideband self-adjoint sensitivity analysis," *IEEE Trans. Microwave Theory Tech.*, vol. 56, no. 8, pp. 1917–1927, Aug. 2008.

SMF, Bandler Corporation, P.O. Box 8083, Dundas, ON, Canada L9H 5E7, 2007.

J. Tao, Q. Peiwen, C. Liang, and L. Liang, "Research on a recognition algorithm for offshore-pipeline defects during magnetic-flux inspection," *Defektoskopiya,* vol. 41, no. 4, pp. 34–43, Apr. 2005.

A. N. Tikonov and V. Arsenine, *Solutions of Ill-Posed Problems*. New York: Winston, 1977.

A. Trehan, R. K. Amineh, M. S. Georgiev, and N. K. Nikolova, "Photogrammetry-based surface reconstruction for improving microwave breast tumor detection," *24th Int. Review of Progress in Applied Computational Electromagnetics (ACES)*, Canada, 2008.

A. Trehan, R. K. Amineh, M. S. Georgiev, and N. K. Nikolova, "Accuracy assessment of photogrammetry surface reconstruction for improving microwave imaging," *IEEE Int. Symp. on Antennas and Propag. and USNC/URSI National Radio Science Meeting (AP-S/URSI)*, USA, 2008.

L. W. Tsay, Y. C. Chen, and S. L. I. Chan, "Sulfide stress corrosion cracking and fatigue crack growth of welded TMCP API 5L X65 pipe-line steel," *Int. J. Fatigue*, vol. 23, no. 2, pp. 103–113, Jan. 2001.

D. A. Woten and M. El-Shenawee, "Broadband dual linear polarized antenna for statistical detection of breast cancer," *IEEE Trans. Antennas and Propag.*, vol. 56, no. 11, pp. 3576-3580, Nov. 2008.

T. Wuren, T. Takai, M. Fuiji, and I. Sakagami, "Effective 2-Debye-pole FDTD model of electromagnetic interaction between whole human body and UWB radiation," *IEEE Microwave Wirel. Components Lett.,* vol. 17, no. 7, pp. 483–485, Jul. 2007.

J. J. Xia, T. M. Habashy, and J. A. Kong, "Profile inversion in a cylindrically stratified lossy medium," *Radio Sci.*, vol. 29, pp. 1131–1141, 1994.

Y. Xie, B. Guo, L. Xu, J. Li, and P. Stoica, "Multi-static adaptive microwave imaging for early breast cancer detection," in *Proc. 39th Asilomar Conf. on Signals, Syst. and Comput.*, Nov. 1, pp. 285–289, 2005.

Y. Xie, B. Guo, L. Xu, J. Li, and P. Stoica, "Multistatic adaptive microwave imaging for early breast cancer detection," *IEEE Trans. Biomed. Eng.*, vol. 53, pp. 1647–1657, Aug. 2006.

L. Xu, S. K. Davis, S. C. Hagness, D. W. van der Weide, and B. D. Van Veen, "Microwave imaging via space-time beamforming: Experimental investigation of tumor detection in multilayer breast phantoms," *IEEE Trans. Microwave Theory Tech.*, vol. 52, pt. Part 2, pp. 1856–1865, Aug. 2004.

M. Yan, S. Udpa, S. Mandayam, Y. Sun, P. Sacks, and W. Lord, "Solution of inverse problems in electromagnetic NDE using finite element methods," *IEEE Trans. Magn.*, vol. 34, no. 5,pp. 2924–2927, Sept. 1998.

C. Yu, M. Yuan, J. Stang, E. Bresslour, R. T. George, G. A. Ybarra, W. T. Joines, and Q. H. Liu, "Active microwave imaging II: 3-D system prototype and image reconstruction from experimental data," *IEEE Trans. Microwave Theory Tech.*, vol. 56, no. 4, pp. 991–1000, Apr. 2008.

J. Zhang, E. C. Fear, and R. Johnston, "Cross-Vivaldi antenna for breast tumor detection," *Microwave and Opt. Lett.*, vol. 51, no. 2, pp. 275–280, Feb. 2009.

Z. Q. Zhang and Q. H. Liu, "Three-dimensional nonlinear image reconstruction for microwave biomedical imaging," *IEEE Trans. Biomed. Eng.*, vol. 51, no. 3, pp. 544–548, Mar. 2004.